ABSTRACT

Nanocluster Defects and Their Properties on TiO_2(110) and (001) Surfaces

Nan-Hsin Yu

Mentor: Kenneth T. Park

TiO_2(110) and (001) have been investigated by low energy electron diffraction (LEED) and scanning tunneling microscopy (STM). A nearly bulk-like (1 × 1) TiO_2(110) was produced after cycles of Ar^+ sputtering and surface annealing at moderate conditions. However, with an increasing number of preparation cycles, the partially reduced surface was then obtained. The surface was heterogeneous with the formation of dispersed nanometer-sized bright strands terminated with bright nanoclusters on the (1 × 1) terraces. They were identified as substoichiometric (TiO_x, $x < 2$) and stoichiometric defects, respectively. Upon the adsorption of gold, the stoichiometric nanoclusters were observed to be the most active sites for the initial nucleation of Au and the subsequent formation of nanoparticles. The first principles calculations indicated

that both geometric and electronic effects of the under-coordinated O atoms of the nanocluster with surface O atoms were responsible for exceptionally strong binding sites for Au nanoparticles. This atomistic model suggests a potentially active site for low temperature CO oxidation by Au nanoparticles.

TiO_2(001) under similar preparation conditions revealed the so-called latticework reconstruction: row-like linear structures running along [110] and $[1\bar{1}0]$ directions. Each row further consisted of bright spots separated by 6.5 Å. In some areas, the rows were separated by 13 Å consistent with the lattice domains of $(2\sqrt{2}\times\sqrt{2})R45^\circ$ observed by LEED. In other areas, the rows were distributed in a more random fashion. Thus various nearest neighbor distances and relative heights of the rows formed different microfacets. From the LEED and STM data, a stoichiometric nanocluster is proposed as the basic building blocks for the latticework reconstruction. It is modeled using six TiO_2 units located at bulk-extended positions on TiO_2(001) similar to those on TiO_2(110). The single-step height clusters can further grow into a linear structure either along [110] or $[1\bar{1}0]$, exhibiting many structural traits experimentally observed.

Nanocluster Defects and Their Properties on TiO_2(110) and (001) Surfaces

by

Nan-Hsin Yu, B.S., M.S.

A Dissertation

Approved by the Department of Physics

_____

Gregory A. Benesh, Ph.D., Chairperson

Submitted to the Graduate Faculty of
Baylor University in Partial Fulfillment of the
Requirements for the Degree
of
Doctor of Philosophy

Approved by the Dissertation Committee

_____

Kenneth T. Park, Ph.D., Chairperson

_____

Wickramasinghe M. Ariyasinghe, Ph.D.

_____

Carlos E. Manzanares, Ph.D.

_____

Linda J. Olafsen, Ph.D.

_____

Bennie F. L. Ward, Ph.D.

Accepted by the Graduate School
August 2012

_____

J. Larry Lyon, Ph.D., Dean

Page bearing signatures is kept on file in the Graduate School.

TABLE OF CONTENTS

LIST OF FIGURES

LIST OF TABLES

ACKNOWLEDGMENTS

I am indebted to my mentor Dr. Kenneth T. Park, for his guidance on my work. It has been my pleasure to have an adviser who has fully trusted me with operating his lab. Through the years, great support, time, and prayers from him and Mrs. Maria Park have made this dissertation possible. Also I would like to express my appreciation to Dr. Gregory A. Benesh, Dr. Wickramasinghe M. Ariyasinghe, Dr. Carlos E. Manzanares, Dr. Linda J. Olafsen, and Dr. Bennie F. L. Ward for their kind assistance and concerns in completing this work.

In addition, I would like to give thanks to Dr. Gregory A. Benesh, Dr. Gerlad B. Cleaver, Dr. Lorin S. Matthews, Dr. Dwight P. Russell, Dr. Kenneth T. Park, Dr. Anzhong Wang and Dr. B.F.L. Ward for teaching and preparing me for the physics profession. I have enjoyed learning with them and thank them for setting great examples of instructors. I would like to thank Dr. Minghu Pan for initiating my experimental skills and Dr. Zhenrong Zhang for her discussions and suggestions for this work. I also would like to thank Dr. Linda Kinslow and Mr. Randy Hall for the years of help, advice, and counseling with lab teaching. I owe warm thanks to Mrs. Baker Chava, Mrs. Marian

Nunn-Graves and Dr. Yumei Wu for their help and assistance with my study and life at Baylor University.

I am grateful to our group members, especially Mr. David Katz who was my coworker through a tough period in the lab. I am also grateful to the members of Dr. E. W. Plummer's group for the generous assistance and warm friendships during my stay at University of Tennessee, Knoxville in 2007 and Louisiana State University in 2010. I deeply appreciate Mr. Jerry M. Milner , Mr. Joe W. McCulloch, and the late Mr. Milton Luedke for the professional support on laboratorial techniques. It would have been challenging to keep the lab running without them and their excellent skills. I would like to thank Dr. Jorge Carmona Reyes for helping me modify the LabView codes and the tutors in the Writing Center for critically reading this manuscript.

My sincere thanks go to my brothers and sisters in Waco Chinese Church, who love me in deed and in truth. I clearly know that I am blessed with you and so many good and kind professors and friends around who have always lent a helping hand whenever I am in need. Although I am unable to list all of their names here, I have memorized their faces and smiles in my heart.

To my dearest family, I wish to express my love and great acknowledgement. Special thanks go to my parents, Ben and Marian Yu, and my husband Daniel; thank you

for loving and supporting me unconditionally, and always encouraging me and remembering me in your thoughts and daily prayers, particularly during my time studying abroad. To my beloved daughter Anna, thank you for being my great joy, comfort, and sweet company.

And finally, the ultimate credit for my work and my life goes to the Author of humanity.

In Memory of My Grandparents

CHAPTER ONE

Introduction

1.1 Titanium Dioxide

Titanium dioxide (TiO_2) is of considerable interest among transition metal oxides. Reflecting the ever-growing interest from the scientific community, the number of publications on single crystalline TiO_2 alone shows the exponential growth over the past three decades [1, 2]. The popularity of the oxide is in part due to the fact that high purity, high quality, single crystal specimens have been made available through synthesis. With a basic understanding of the structure and properties of bulk TiO_2, it has become a prototype model system for understanding other transition metal oxide surfaces. In addition, its technological importance in various industrial applications has made it one of the most extensively studied oxide surfaces. For example, TiO_2 is an essential component used in paints as white pigment. Also, taking advantage of its optical properties, it is used in thin-film optical-interference coatings to control the transmission and reflection ratio of light applied for various mirrors and optical components [3]. The photochemical or photocatalytic properties of TiO_2 are, on the other hand, perhaps the most active areas in materials research. The use of TiO_2 as a catalytic electrode by

Fujishima and Hinda [4] to decompose water into H_2 and O_2 in a photoelectrolysis cell has stimulated intense research for finding ways to produce clean energy since the 1970's. The electron-hole pairs created upon irradiation with sunlight have been further investigated by reacting with adsorbed water and oxygen to produce radical species that decompose the organic molecules. Photo-assisted degradation of organic molecules applied in wastewater purification and self-cleaning coatings on windows are examples of active on-going research to exploit photochemical or photocatalytic properties of TiO_2.

In spite of these promising applications of titanium dioxide (also called titania), the fundamental understanding of their surface structures and the principles behind the observed photochemistry and catalysis is still lacking in many aspects. The improvement of the materials' photochemistry and performance first requires understanding the atomistic structure and the local electronic properties of TiO_2 salient to photochemistry and being able to tailor them for desired outcomes. For example, the band gap of rutile TiO_2 is about 3.0 eV, which corresponds to absorption of photons in the near-ultraviolet region. Consequently, TiO_2 is a poor absorber of photons in the solar spectrum. Countless efforts have been made in extending its photo-activity to the natural sun light region. Recently, Ariga *et al*. [5] reported an unexpected photo-oxidation reaction of formic acid on pure TiO_2 (001) single crystalline surface via

visible light. This study suggested the band gap narrowing to 2.3 eV (visible light 2.1~2.8 eV) due to the surface state of pure reconstructed TiO_2 (001) surface [5].

Understanding the surface states and the active sites on the reconstructed TiO_2(001), as well as other crystallographic faces, could be a key step toward developing practical applications based on TiO_2. In this dissertation, my cumulative work on the surfaces of rutile TiO_2 single crystals is presented. Especially, it aims at understanding the structural-functionality relationship for nanometer-sized defects on TiO_2(110) and TiO_2(001). Before proceeding to the technical results and discussions, brief descriptions of crystalline TiO_2 and surface defects are presented below as a tutorial to the rest of the dissertation.

Rutile is one of the three major crystal polymorphs found in titanium dioxide (TiO_2). The other two less common forms are anatase and brookite. The basic building block in these structures is TiO_6 octahedron with more or less distorted configurations. The octahedra are stacked in a way that they share both corners and edges in rutile and brookite, but share only edges in anatase [6].

The octahedral building block containing a titanium atom at the center and six oxygen atoms at the apices is shown in Fig. 1.1(a). In rutile, the four bond lengths between the coplanar oxygen and the titanium atoms are equal to 1.946 Å, which is

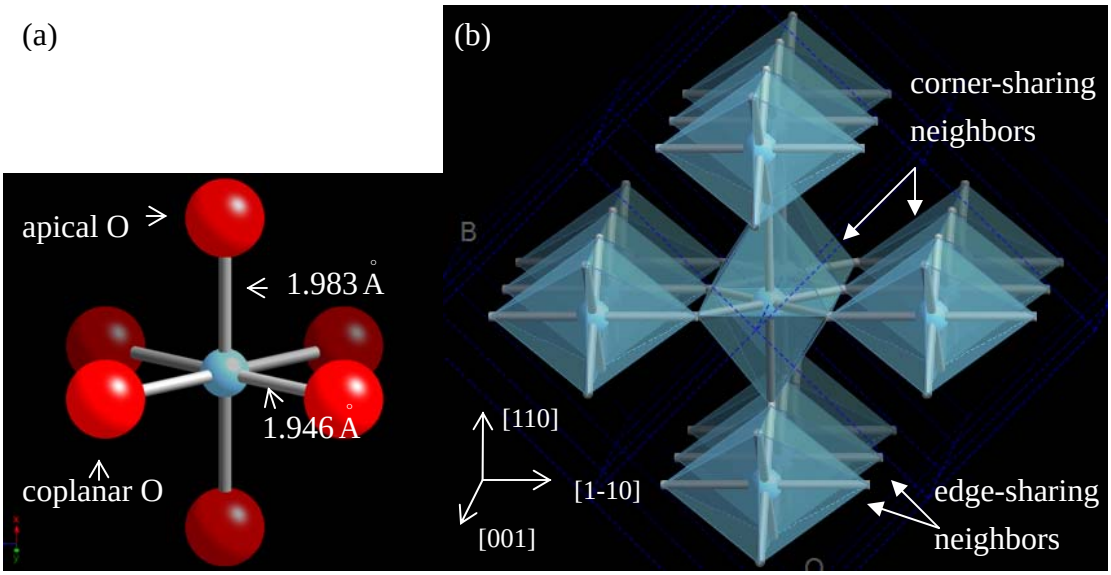

FIG. 1.1. Bulk structure of rutile TiO_2. (a) A unit of octahedron. Oxygen and titanium atoms are red and blue sphere, respectively. (b) The structure in polyhedral model.

shorter than 1.983 Å, the two bond lengths between the apical oxygen atoms and the titanium atom. The octahedra are connected by their edges along the [001] direction but are stacked by their corners and angled at 90° oriented with respect to their neighbors along the $[1\bar{1}0]$ and the [110] directions (Fig. 1.1(b)). Consequently, rutile TiO_2 has tetragonal structure, whose lattice constants are a=4.59 Å and c=2.953 Å [7-8].

Among the low index surfaces of rutile TiO_2, surface energy of (110) is found to be the lowest while (001) surface is the highest. The surface structures of (110) and (001) with bulk-like termination are shown in Fig. 1.2. The (110) surface outline is corrugated with the top layer of 2-fold oxygen atoms, called bridging oxygen, sticking out of the surface. The second layer consists of 3-fold oxygen and both 5-fold and 6-fold titanium

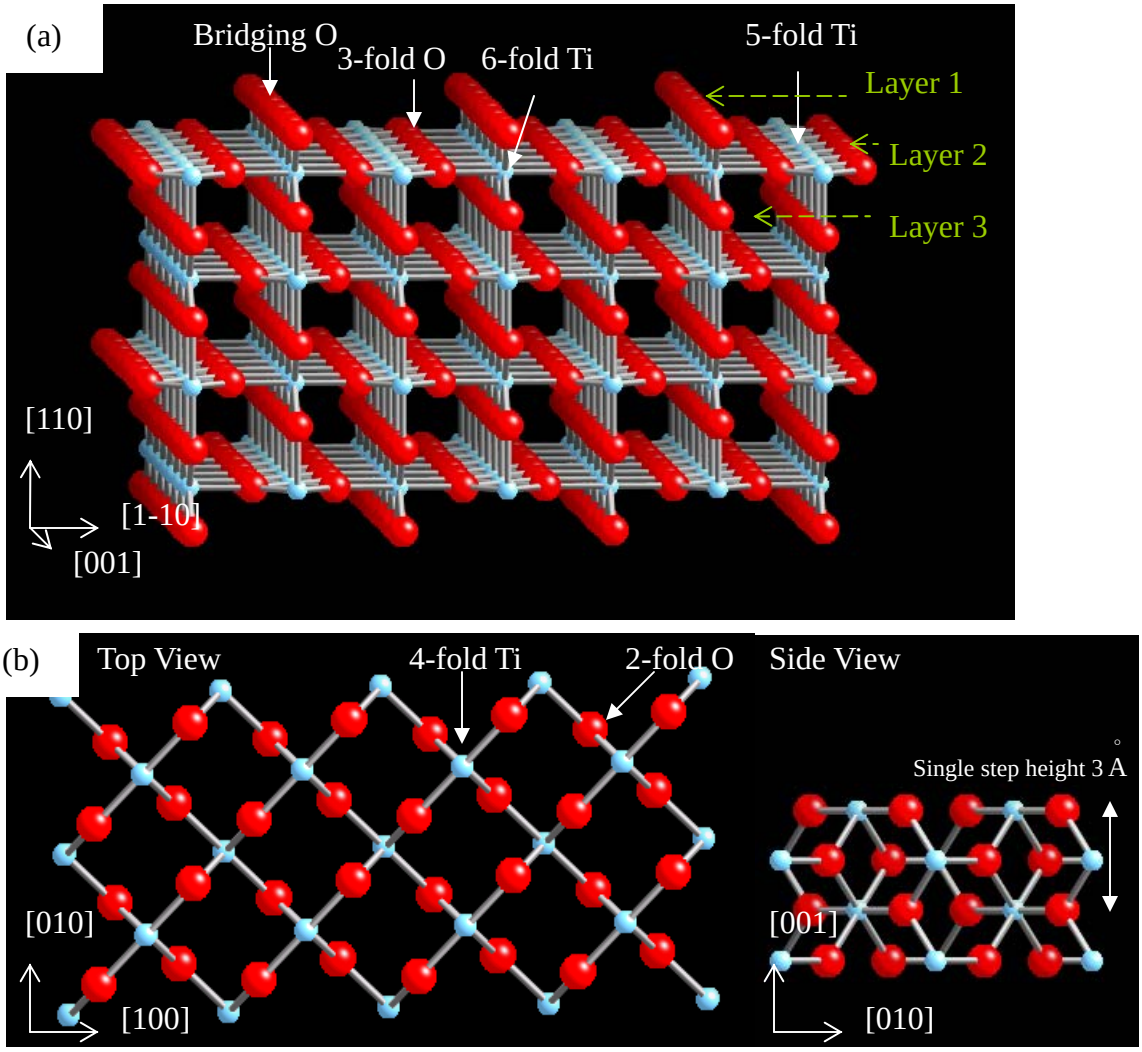

FIG. 1.2. Surfaces of rutile TiO_2(110) (a) and (001) (b).

atoms. The third layer has only 3-fold oxygen atoms. For the subsequent layers, this 3-layer unit is repeated after shifting half the lattice constant along the $[1\bar{1}0]$ direction. On (110) surface, each of the bridging oxygen atoms and the 5-fold coordinated titanium atoms have one dangling bond. Since the same number of oxygen-to-titanium bonds are broken as titanium-to-oxygen, the surface is autocompensated and stable [9, 10].

(Autocompensation refers to the fact that excess charges from cation-derived dangling bonds compensate anion-derived dangling bonds, and the net charge involved remains zero. Alternatively, it can be thought of as completely filling the valence band orbitals while completely emptying the conduction band orbitals [11].) On the other hand, the (001) surface has a higher number of broken bonds. All the oxygen atoms are 2-fold, compared to 3-fold in bulk, and all the titanium atoms are 4-fold in contrast to six in bulk. Consequently, the surface has a high surface energy even though the surface is non-polar and autocompensated. To lower the energy, an extensive reconstruction of the (001) surface takes place. A particular type of the (001) reconstruction, known as the latticework, is discussed in Chap. 5.

Even for a high quality single crystal specimen, defects are inevitably present due to both thermodynamic and practical reasons. Far too often, surface defects are introduced by the very methods of preparing for a clean and ordered surface. Surface defects of TiO_2 can be generated by ion bombardment or by high temperature annealing. Because different types of defects on TiO_2 surfaces have different chemistry [12], it is important to understand the nature and characteristics. Only a couple of known and investigated defects are mentioned in this chapter. Oxygen vacancy is one of the most frequently studied point defects from the single crystal surface. When an O^{2-} ion is removed from

the surface due to high temperature heating and/or preferential sputtering during ion bombardment, oxygen vacancy is created and two electrons are left. One or two of the electrons can occupy the adjacent metal sites causing Ti to form the lower oxidation states Ti^{3+} or Ti^{2+}, respectively. For a pristine TiO_2, the band gap of about 3 eV opens up between the mainly O2p-derived valence band and the Ti3d-derived conduction band. After the formation of the O vacancies, localized surface states are introduced within the band gap. This is because the previously occupied O2p states are unavailable as the oxygen is removed. Therefore, the residual electrons move to the localized states below the conduction band [13, 14]. Such states have played an important role in photochemistry as they represent localized states and effectively reduce the band gap [15].

Line defects and small cluster defects also have been observed on clean and oxygen-deficient TiO_2 surfaces [16]. Line defects can grow on the surfaces, often extending out of step edges onto the lower terrace. They are believed to form as a result of mass transport of Ti interstitials and O vacancies between bulk and surface in significantly reduced TiO_2 samples [17]. They represent oxygen-deficient or sub-stoichiometric (TiO_x, $x < 2$) extended defects at the nanometer scale. The line defects are also often observed to terminate with clusters at the ends. Unlike the line

defects, the clusters are a fully stoichiometric (TiO_2) species [18]. Their structure and properties are one of the major topics discussed in this dissertation and will be comprehensively reviewed in later chapters.

CHAPTER TWO

Experiments

2.1 Vacuum System Technology

2.1.1 Ultra-High Vacuum (UHV)

Ultra-high vacuum (UHV) is widely used in experiments that involve investigating the surface properties of materials. The vacuum range below 10^{-8} Torr is generally defined as UHV. Under UHV, the collision rate of residual gas molecules and atoms with a surface is low enough that the surface contamination remains minimal from a few minutes to a few hours depending on the pressure and the surface reactivity. In addition, the low collision rate means a long mean free path (greater than 10 cm) for particles such as electrons and ions [19]. Because they do not suffer significant scattering from residual gas in UHV, they can be used to probe the sample surface and be analyzed for their energy and momentum transfer during the interaction.

In order to achieve a UHV condition, different types of vacuum pumps are generally employed. Vacuum pumps can be categorized by their operating pressure as listed in Table 2.1 [20]. Among the various kinds of pumps, mechanical pumps, turbo molecular

Table 2.1. Vacuum pumps and their operating ranges [20]. (1 mbar = 0.75 Torr)

	Rough Vacuum	Medium Vacuum	High Vacuum	Ultra-high Vacuum
Pressure (mbar)	1000—1	$1—10^{-3}$	$10^{-3}—10^{-7}$	$10^{-7}—$
Piston pump				
Diaphragm pump				
Liquid ring pump				
Sliding vane pump				
Rotary plunger pump				
Roots pump				
Roots/claw pump				
Screw pump				
Ejector pump				
Diffusion pump				
Diffusion ejector pump				
Turbo molecular pump				
Getter ion pump				
Cryopump				
Adsorption pump				
Titanium sublimation pump				

pumps, ion pumps and titanium sublimation pumps (TSP) are used to achieve UHV pressure in the two systems described in this dissertation. They are housed separately in the Laboratory for Surface Analysis and Modification (LSAM) at Baylor University for low energy electron diffraction (LEED) study and in the Materials Research Laboratory (MRL) at the Louisiana State University (LSU) for LEED and scanning tunneling microscopy (STM) study. A mechanical pump, also called a roughing pump, is able to generate a vacuum of 10^{-3} Torr. It is typically employed as the foreline pump for a turbo-molecular pump. A turbo-molecular pump, or a turbo pump in short, can further bring down the pressure from 10^{-3} Torr to 10^{-8} Torr (or even

10^{-9} Torr) without any treatment of the UHV chamber. In order to lower pressure or achieve high vacuum, both pumps physically remove the molecules inside a chamber towards the exhaust. A roughing pump compresses the gas molecules that had entered its inlet and then forces them to the exhaust by the two spring-loaded vanes. Unlike the roughing pump, a turbo pump does not have vanes but instead consists of rotors and stators both with circular blades. The combination of the fast spinning rotor and the stator causes the gas molecules to move in a preferred direction due to the collisions [21]. The momentum transfer provided by the turbo pump helps remove the molecules from the system.

In order to further achieve the pressure in the range of 10^{-9} Torr or lower in a reasonable period of time, e.g. in days as opposed to in weeks, a chamber needs bakeout. The purpose of bakeout is to remove the adsorbed impurities, especially water, from the inner walls of an ultrahigh vacuum chamber [22]. The chamber as well as the ion pump, which will be described shortly, are heated between 100 and 200 °C using the combination of heating tapes and panels while pumping the system using a turbo pump. The temperature of the chamber is monitored with thermocouple wires over several different places including the far ends of the chamber to assure uniform heating at a desired temperature of the minimum 100 °C. The bakeout usually takes 48 hours.

After the bakeout, degassing or outgassing is performed on all the UHV parts that contain filaments. In this procedure, controlled amounts of electrical current are sent through the filaments to heat them and their immediate surroundings for a short period of time, typically no more than 30 minutes. The intense heat from the filaments results in a short burst of the desorption of the impurities. After degassing is repeated a few times, the combination of an ion pump and a TSP is then used to bring the pressure of the chamber finally into the 10^{-10} Torr range and maintain it. Contrary to the mechanical pumps described previously, an ion pump does not physically remove gas molecules from the system. Instead it ionizes them, accelerates the gas ions toward the titanium cathode, and then embeds them into the cathode. It is highly reliable as it does not involve any mechanical parts. It is also very effective for reactive gases since they form stable, non-volatile compounds on the titanium cathode surface. TSP is used to supplement the ion pump by reacting with the molecules to form a stable product with titanium vapor. It is operated by passing a high current generally 40 to 50 A to heat a titanium filament. The sublimed titanium atoms from the hot filament can cause the chamber pressure to increase by an order of magnitude temporarily. However, once the titanium atoms react with gas molecules and form stable compound films the pressure decreases, and a lower base pressure is obtained.

2.1.2 Thermal Control: Heating and Cooling of Sample

In addition to the UHV condition, the ability to control the sample temperature is also a requirement for surface preparation as well as surface studies. To increase the sample temperature, both methods of radiation heating and electron bombardment heating are available in the LSAM vacuum chamber. These methods are termed indirect heating as the sample is indirectly heated via the contact with the sample holder, which is heated by a heat source. Radiation heating and electron bombardment heating share the same configuration of heating elements as depicted in Fig. 2.1.

A tungsten filament, obtained from a commercially available halogen lamp (12 V, 50 W), is mounted onto two stainless steel connectors. It is positioned about 1.5 mm below

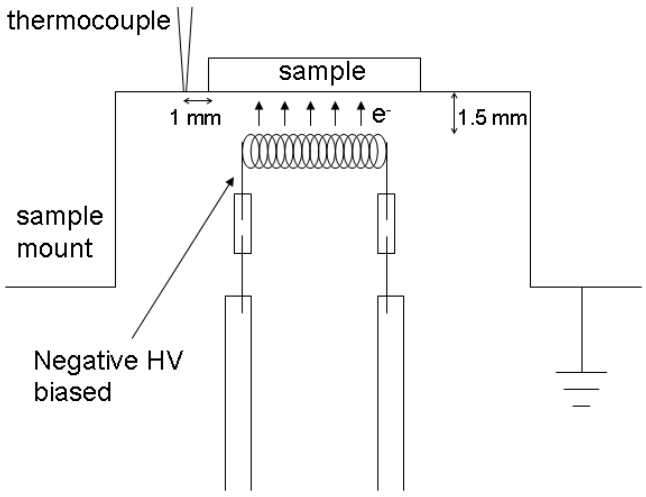

FIG. 2.1. The sample heating device which is capable of radiation heating and electron bombardments heating in LSAM. For electron bombardment, the filament is biased with negative high voltage to induce the electron emission onto the back of the sample.

the sample stage [22]. The leads of the filament are brought into contact with the annealed molybdenum wires (70 mm, 1 mm dia, 99.95%, Alfa Aesar) through the stainless steel connectors. The Mo wires are fitted through an Al_2O_3 tube (Scientific Instrument Services, Inc.) to copper wires. The Cu wires are connected to the power supply outside the chamber via an electrical feedthrough. During heating, the sample temperature is measured and monitored using a K-type thermocouple wire attached to the sample holder.

For radiation heating, typically 3 A of current is sent through the W filament. The sample holder is heated by radiation generated by the hot filament. Radiation heating by itself can bring the sample temperature up to a few hundred degree Celsius. However, a metal oxide like TiO_2 requires an even higher temperature to anneal its surface from damages incurred during ion sputtering.

So for this reason, the heating device is also capable of electron bombardment or electron-beam heating. The electron bombardment method takes advantage of the same filament assembly used in radiation heating. However, in this method, the filament is biased with voltages from -600 V to -1 kV to accelerate electrons toward the sample stage, which is grounded. Because of the high voltage applied to the filament, the wires are doubly shielded: first with glass fiber sleeves, then fitted into ceramic beads to ensure

electrical isolation between the wires as well as between the wires and the ground. It is note-worthy that the bombarding electrical current to the sample is sensitive to the gap distance between the filament and the sample stage. If the gap is too large, the high voltage current is negligible, and the heating is mainly due to radiation. On the other hand, if the gap is too narrow, there is a risk that the filament will touch the sample holder and get electrically shorted. With the gap of 1.5 mm, 50 mA of the sample current is usually measured with the bias of -700 V. With this emission current, a typical temperature of 650 °C is achieved within minutes of applying the electron bombardment method.

In MRL, a sample is also heated indirectly. A sample is mounted on a slotted holder where a layer of electrically non-conductive material is coated between them. The slotted holder is resistively heated so that the sample reaches the desired temperature. The temperature is measured by a calibrated optical pyrometer.

Just as the ability of heating a sample is critical in surface preparation, the ability to lower the surface temperature is highly desirable for surface studies. For low temperature LEED study, the UHV chamber in LSAM is equipped with an indirect cryogenic cooling unit (Thermionic Northwest, Inc., Fig. 2.2). The indirect cooling method lowers the sample temperature by thermal conduction through flexible copper

braids attached to a remote liquid nitrogen reservoir. Although the cooling efficiency with the use of Cu braids is poor compared to that with the direct contact of the reservoir to the sample, this configuration allows for flexibility in the sample movement, as well as an ample space to accommodate the sample heater described previously. Liquid nitrogen is supplied with inlet pressure of 22 psi to the reservoir through one of the

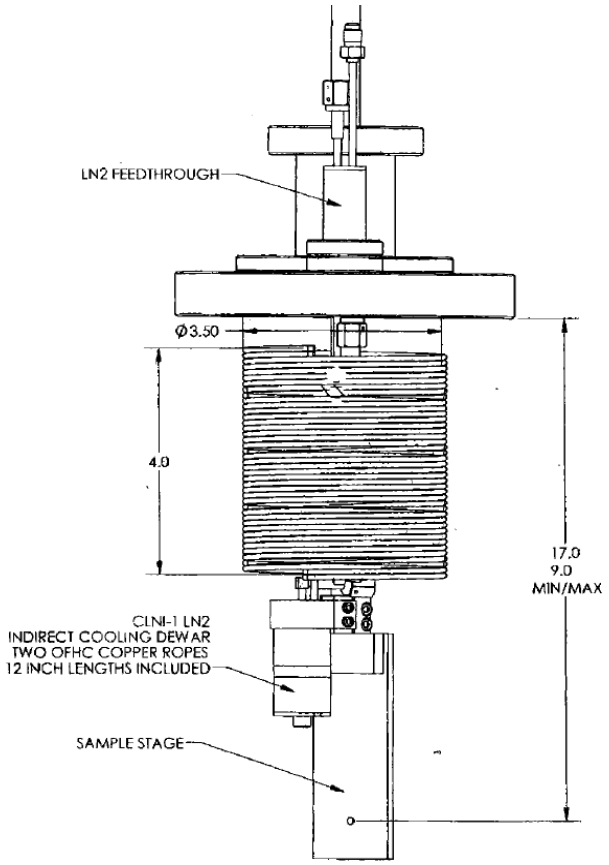

FIG. 2.2. Indirect cryogenic cooling system in LSAM. It consists of 1/8" inlet and outlet tubes. Inside the UHV system, the coils of the 1/8" tube can be extended or compressed as the sample moves. The reservoir is suspended from the 1/8" tubes and is connected to the sample stage via four Cu braids (not drawn in the figure).

1/8-in. diameter stainless steel coil tubes. After the heat exchange, the excess liquid and vapor exit out of the reservoir through the outlet tube. A typical cooling behavior of the sample stage is shown in Fig. 2.3. The sample temperature of 190 K can be reached within an hour.

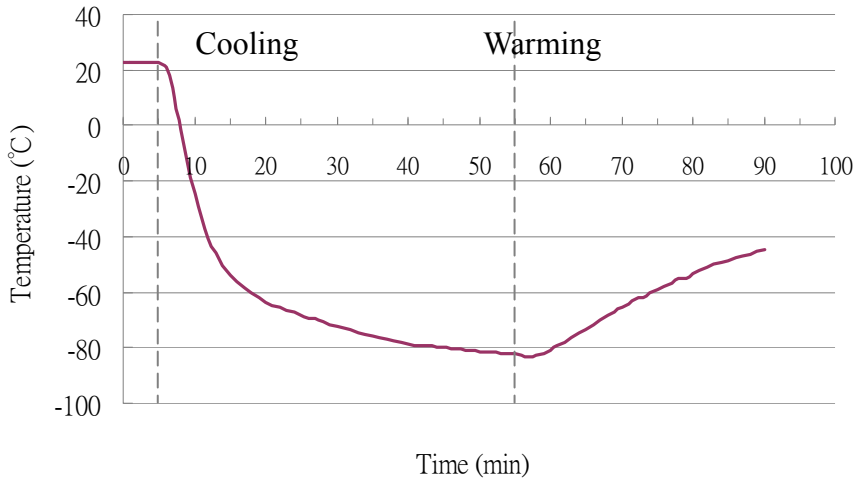

FIG. 2.3. A cooling behavior of the cryogenic cooling system in LSAM. The supply of liquid nitrogen is turned off after 55 minutes.

The ultimate cooling temperature and the time it takes to reach it can be improved by future design modification. An additional flow regulator at the inlet can reduce the amount of liquid nitrogen flow from the supplier tank to the inlet. This can optimize the flowing rate of liquid nitrogen into the reservoir, then it can further improve the cooling efficiency. Also the size of the sample holder can be reduced. The total surface areas of the sample holder and the four Cu braids are about 13 cm^2 and 54 cm^2, respectively.

The ratio of the surface areas is about one to four. Although the size of the Cu braids is comparable to that suggested by the standard design [22], the sample holder is larger than necessary. Hence by reducing unnecessary size, the cooling efficiency can be improved. Besides, a radiation shield between the sample holder and the manipulator is suggested for reducing the heat flowing to the sample holder.

2.2 Experimental Methods: Sample Preparation

2.2.1 Bare TiO_2(110)

It is well known that the surface with bulk-like termination, the so-called (1 × 1) surface, can be produced on TiO_2(110) after cycles of ion sputtering followed by annealing. In LSAM, sputtering was accomplished with a differentially pumped ion gun. Ar gas was introduced into the chamber using a precision-leak valve to backfill the ion gun and the chamber to the pressure of about 5×10^{-7} Torr. A 1 kV Ar^+ beam was produced by the ion gun and directed at the sample to sputter the sample surface. The amount of Ar^+ ions impinging on the surface was estimated using the corresponding ion current at the sample. A typical ionic current of 1 μA was measured during sputtering. After about 15 minutes of sputtering, the chamber was pumped down to UHV, and the sample was annealed to 640 °C for 15 minutes. The sample was then allowed to cool

down to ambient temperature. The above procedure was repeated many times until a highly ordered (1 × 1) surface was obtained.

In addition to the bulk-like surface, TiO_2(110) is also known to exhibit a reconstructed surface after a preparation treatment under a reducing (oxygen deficient) condition. The periodicity along the $[1\bar{1}0]$ direction typically doubles to form the so-called (1 × 2) TiO_2(110) surface. In order to prepare the (1 × 2) reconstructed surface, sputtering was performed with a higher Ar^+ ion current, about twice the current used for the (1 × 1) surface for 15 minutes or sometimes longer. On TiO_2, Ar^+ ions inherently tended to knock out O atoms more easily than Ti atoms. With larger Ar^+ ion currents bombarding the surface, the preferential sputtering of oxygen quickly created the imbalance in the surface stoichiometry and sped up the surface reducing process. The ion-bombarded, Ti-rich surface was then subjected to annealing at temperature of 750 °C for 15 minutes. This annealing temperature was intentionally higher than that used in producing (1 × 1) TiO_2(110) because the higher the temperature, the more easily surface oxygen atoms desorbed. So, annealing at a higher temperature aimed not only to heal the ion-damaged surface but also to keep the surface oxygen-deficient. The cycles of intense sputtering and annealing were repeated until a (1 × 2) surface was obtained.

2.2.2 TiO_2(001)

TiO_2(001) is believed to be the most reactive surface among the low index surfaces of rutile TiO_2. Perhaps closely related to its intrinsic reactivity, the surface state is thought to mediate various photo-chemical reactions on the surface. In order to study its atomically-ordered surface structures, two samples of polished TiO_2(001) were employed in this work. For both samples, preparation conditions were kept as mild as possible so that the surfaces were minimally disturbed and remained as pristine (that is, stoichiometric) as possible.

In LSAM, the single crystal of $10 \times 10 \times 1$ mm^3 was directly mounted on a stainless steel sample holder. The cycles of argon sputtering (1 kV for 15 minutes) and annealing above 700 °C for 15 minutes were performed. The heating/cooling rates were 1 °C /s at temperature above 500 °C and 2 °C /s at temperature below 500 °C.

In MRL, a sample was cut from the back side into two halves of $10 \times 5 \times 1$mm^3, and one of the two was used for STM and LEED studies. Because the sample was cut in house, it was ultrasonically rinsed in acetone and then in MilliQ water for five minutes each and dried with N_2 gas. This rinsing process was repeated twice before the sample was transferred into the UHV chamber whose base pressure was 2×10^{-10} Torr. A Ta foil was placed between the sample and the sample stage to ensure uniform heat

distribution. In addition, the foil was used to block the radiation emission from the resistive heater for an accurate pyrometer reading. After introducing the sample into the UHV chamber, it was pre-annealed overnight to a few hundred degrees Celsius (filament current 2 A, 4 V). The sample was then cleaned by several cycles of sputtering and annealing. Ar^+ sputtering was performed with 0.3 μA at 1 kV for 15 minutes followed by annealing at a temperature up to 600 °C for 15 minutes. The heating/cooling rates were 1 °C /s at temperatures above 300 °C. Temperature was measured by an optical pyrometer with the emissivity ε set as 0.5.

2.2.3 Deposition of Au

One of the major scientific applications using TiO_2 is to provide a structural support for catalysts in the form of metal nanoparticles. Gold nanoparticles supported on TiO_2 are one such example. The unexpected oxidation of carbon monoxide by Au/TiO_2 catalysts even below room temperature has been subject to intense research in the past decade [23]. Thus, the ability to deposit and grow metal nanoparticles on a model single crystal surfaces is essential toward atomic-level investigation of such catalytic activity at the interfaces between the metal and the oxide.

Gold was deposited onto a clean TiO_2(110) surface *in situ* for studying the formation of the nanoparticles using STM in MRL. The deposition was achieved using an

electron-beam evaporator, which was aimed at the sample stage. A crucible containing a Au wire (99.98%) was mounted on a high-voltage feedthrough. Before Au was actually evaporated, it was repeatedly degassed by applying the filament current up to 14.5 mA at 700 V. For the actual deposition, the source was bombarded by electrons with 15.0 mA at 700 V. During the evaporation, the pressure remained below 2×10^{-10} Torr. The amount of evaporated Au was estimated in terms of the ionic current measured at the opening of the evaporator. The typical ionic current was about 42 nA during the actual deposition. The amount of Au deposited on the sample surface was determined though STM image analysis. More detailed procedures on the quantification of Au deposited is presented in Results and Discussion I.

2. 3 Low Energy Electron Diffraction (LEED)

2.3.1 LEED Optics

LEED is one of the two analytical tools used in this dissertation. It is one of the most widely used and well-established methods in surface analysis. The LEED apparatus in LSAM is based on a 6" reverse-view optics (ErLEED 100) with the power supply ErLEED 1000A. LEED optics consists of an electron gun and a display system (Fig. 2.4(a)).

The 15 mm-diameter electron gun is fitted with a thoria-coated iridium cathode, the Wehnelt cylinder, a double anode, an electrostatic single lens (L1, L2 and L3), and the drift tube (L4) (Fig 2.4(b)). The electron gun may be operated at a pressure up to the upper 10^{-5} mbar (7.5×10^{-6} Torr) range. However, for a longer life-time of the filament, it is operated at a much lower pressure. The hot electrons are emitted from the heated filament by passing a current of 2.3 A. The electrons are accelerated and collimated into a beam along the main axis of the gun by the optics. The energy range of the electron

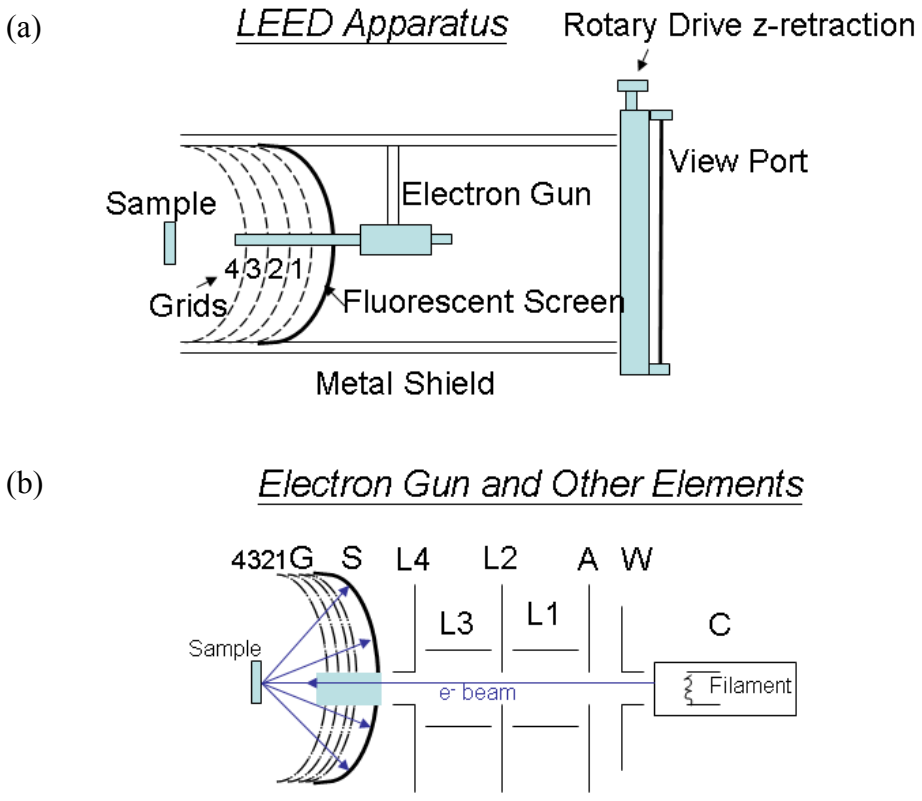

FIG. 2.4. The schematics of the LEED optics. (a) LEED apparatus and (b) electron gun and other elements.

beam is controlled via the potential difference between the anode and the cathode ranging from 0 to 1000 eV. The Wehnelt cylinder (W in Fig. 2.4(b)) acts as an electrostatic aperture between the cathode and the anode. It regulates the penetration of the anode potential onto the direction of the cathode by applying the same or negative potential with respect to the cathode. This may change the size of the electron beam and, therefore, change the sharpness of the diffraction spots. The lens elements are biased separately to shape the electron beam. All Wehnelt and lens voltages vary linearly as a function of energy with adjustable gain and offset. In order to achieve a sharply focused beam over a broad range of electron energy, one has to first optimize all offset voltages at low energies (< 50 eV) and then re-optimize the voltage gains at high energies (> 300 eV), leaving the offsets unchanged. This procedure has to be done iteratively [24].

The display system of the LEED optics is made of four hemispherical concentric grids and a rear view glass screen that is coated with an ITO conducting layer and P43 cadmium free phosphorus (Fig 2.4(a)). They are arranged concentrically around the electron gun, which is pointing toward the sample position. Grid 1 is grounded to provide a field-free region between the sample and the LEED optics. This minimizes an undesirable electrostatic deflection of incident and diffracted electrons. A negative voltage is applied to grid 2 and 3, which are called the suppressor grids to keep away the

inelastically scattered electrons from the screen. Grid 4 is also grounded to reduce field penetration of the suppressor grids to the screen. For the screen, a positive voltage between +4 kV and +6 kV is typically applied to accelerate the electrons and to make their impacts on the fluorescent screen visible.

In MRL, the LEED experiment is conducted using an Omicron's reverse-view LEED optics. It has similar components as described as above, except for a larger viewport based on a 8" CF flange. Since the LEED spots converge toward the center of the screen with increasing incident energy, a larger screen allows one to track the beams over a longer distance before they are blocked from view by the electron gun. Thus, the larger screen optics in MRL permits the collection of I-V (intensity versus voltage) data over a larger dynamic range for the incident beam energy.

2.3.2 LEED Data Acquisition and Extraction System in LSAM

The LEED images are captured with a Watec 902C CCD camera of the specifications 640 by 480 pixels with 16 bits in depth. Then the acquired images are passed to a PC via a Bandit video card and stored in both image (.bmp) and text (.txt) files. Information, such as the incident electron voltage and the current from the LEED control unit, passed through a current amplifier is also stored via a PCI-1200 DAQ card

in a RAMP text file. In LSAM, data acquisition and extraction are automated using the suite of programs written in LabVIEW by a former group member T. Ellis [25].

The whole acquisition processes are controlled by the LEED Acquisition program (LAC). From the stored data, the intensities of the LEED spots or called beams are extracted by the LEED Analysis Master Control program (LAMC). The extracted intensities of spots are then saved with the corresponding incident electron energy and currents. For each diffraction beam, the data then can be plotted into intensity versus voltage or an I-V curve.

In order to differentiate a diffraction spot from the background of inelastically scattered electrons and also to improve the signal to noise ratio of the I-V spectra, the background intensity has to be accurately determined and carefully subtracted. Two methods have been developed and utilized for background subtraction. The first method is the fixed position method (FPM). The background intensity is determined by averaging the background intensity obtained at three fixed positions, shown as yellow boxes in Fig. 2.5. The size of the pre-selected background regions is 20 by 20 pixels. The averaged intensity serves as the background intensity for all the diffraction spots for a given energy of incident electron. The second method is the spot vicinity method (SVM). The background intensity is determined from the vicinity of a given spot (green

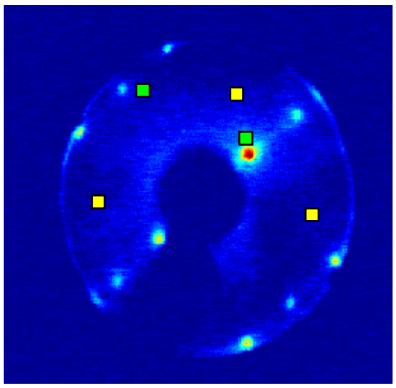

FIG. 2.5. A LEED image on TiO_2(110) surface. Two methods are tested for background subtraction: The averaged intensity of the three yellow (each green) regions is the background intensity used in the fixed point method (FPM) (spot vicinity method (SVM)).

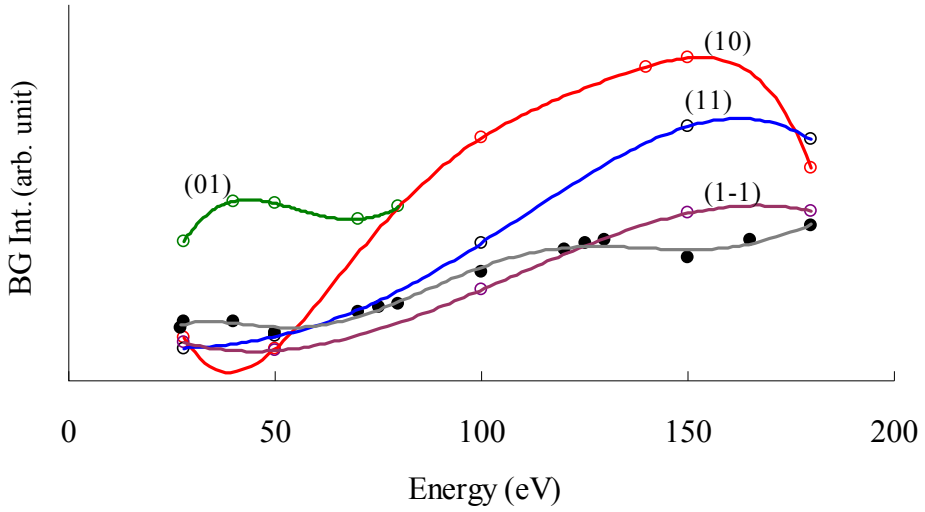

FIG. 2.6. The background intensity of TiO_2(110) LEED data is plotted with the increasing energy for fixed point method (FPM) by the grey line of closed circles and SVM for four beams, (01), (10), (11) and (1-1) by the green, red, blue and purple lines and open circles, respectively. The background intensity varies for the four beams.

squares in Fig. 2.5). Therefore, unlike FPM, each diffracted spot has its own background intensity associated with it.

The plots of background intensity with increasing energy are shown in Fig. 2.6. The background intensity generally increases with increasing electron energy due to larger numbers of inelastically scattered electrons. Thus, the subtraction of accurate background becomes increasingly important for the LEED images obtained at larger incident electron energy. In order to demonstrate the effect of background subtraction, I-V spectra after FPM and SVM background subtractions as well as the I-V spectra

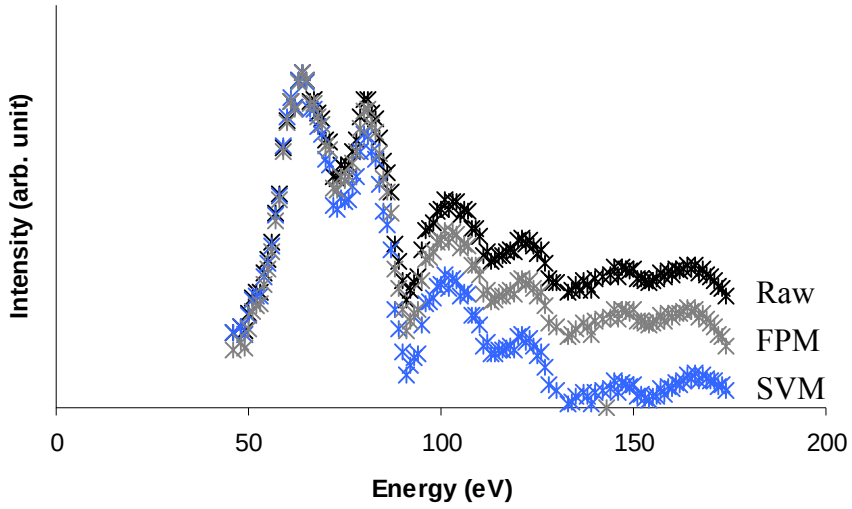

FIG. 2.7. LEED IV spectra of TiO_2(110): (10) beam without (black stars) and with (grey and blue stars) background subtraction. Effect from the background is more pronounced at high energy region. Grey spectrum is from fixed point method (FPM) and blue spectrum is from spot vicinity method (SVM).

before the background subtraction are compared in Fig. 2.7. The effect of background subtraction is more pronounced at higher energies, i.e. above 90 eV; the intensities of the peaks in the region are significantly reduced. The resulting I-V curves are more easily compared to the theoretically calculated I-V curves of elastic scattering. In comparing the two background subtraction methods, it can be seen that FPM underestimates the background intensity at higher energies. Since SVM determines the background specific to each spot, the I-V spectrum after SVM background subtraction is in general more accurately represented. Also one needs to pay careful attention to the background subtraction for the surfaces containing partially disordered, complex, or faceted domains as such surfaces tend to produce spots with lower beam intensity and higher background [26, 27].

Whether one chooses to employ FPM or SVM, the determination and the subtraction of the background intensity must be carried out manually from an image to another image as the original version of the LAMC programs automatically extracted the raw spot intensities only. This manual process of the background subtraction for each beam intensity was labor-intensive and time-consuming. So, an automation of the background treatment has been implemented into the upgraded extraction codes.

Before describing how the background intensity is estimated in the program, a brief outline of LEED Analysis (LAN) operation is presented here. A given LEED image is treated as an array. LAN first uses a LabVIEW's function Array Max and Min VI to find the maximum value of the entire array. It then averages the intensities of pixels in a square around the maximum value. The size of the square is specified as the average spot dimension (2L+1), which is a user specified value on the front panel of LAN (Fig.

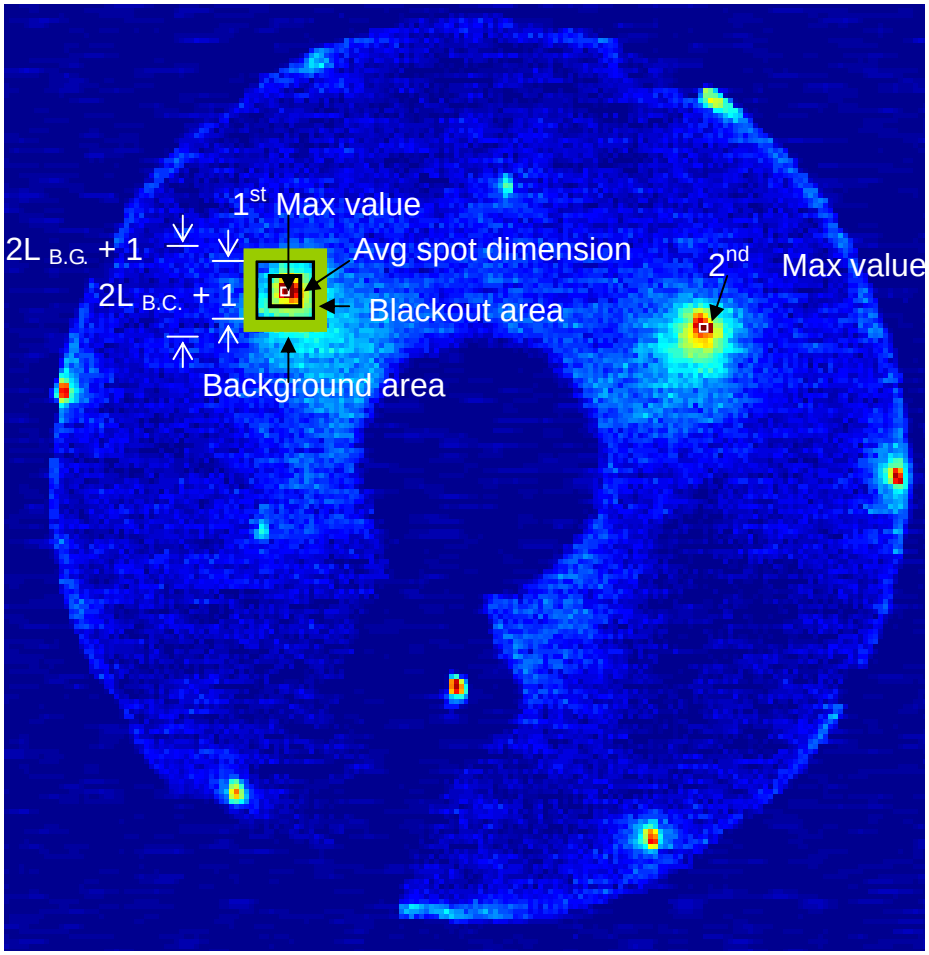

FIG. 2.8. A LEED image is showing the dimensions of the parameters used for LAN.

2.8). After the brightest spot is found and identified as the 1st Max value, LAN is set to begin the search process for the next bright spot as the second diffraction spot. Because the program may falsely identify a pixel in close proximity to the 1st spot as the second diffraction spot, the 1st spot and the surrounding area are removed from the search process through the use of the blackout coefficient (B.C.). The blackout coefficient is specified by the user and is used to determine the size of an area to black out the first spot.

For example, suppose a user enters the value of 0.5 as the B.C. Then the program identifies the area centered at the 1st Max value, in which the average intensity is greater than 50 % of the 1st Max value, as the blackout area of the 1st spot. It is a square with its side dimension being ($2L_{B.C.}$ +1) pixels long. This area is skipped in the search for the next diffraction spot. After the second bright spot is found, the LAN repeats the procedure to find all subsequent diffraction spots in an image.

After all the desired diffraction spots are found, the LAN proceeds to determine the background intensity. Whether the FPM or the SVM is chosen, the background intensity is determined by the same following procedure. The background area is defined as a square with its side dimension of $2L_{B.G.}$ +1, centered on the first diffraction maximum for the FPM or for the SVM, on each diffraction spot (Fig. 2.8). The

parameter $L_{B.G.}$ is related to the parameter $L_{B.C.}$ through $L_{B.G.} = L_{B.C.}$+ background size. The value for the background size can be adjusted from the program's control panel, but the default value is 5. Thus, with $L_{B.G.} = L_{B.C.}$+ 5, the background square is by default larger than the blackout square by five pixels on its side. The background intensity is calculated as the average intensity of this background area. Since the background area and the blackout area are co-centered squares and the values from the blackout area are ignored, only the values from the resulting square strip contribute to the calculation of the background intensity. LAN writes the background intensity to the output file.

2.4 STM

A variable temperature scanning tunneling microscope (VT-STM, Omicron) in MRL was employed to investigate surface morphology at the nanometer scale. The VT-STM is housed in its own UHV chamber bolted onto the main UHV system. An air table supports the whole UHV chamber and reduces environmental vibration. An internal spring suspension system with eddy current damping further ensures the vibrational isolation of STM from other parts of the UHV system. This STM instrument is capable of *in situ* sample or tip exchange. The samples or tips are transferred into and out of the STM stage using a wobble stick. The STM stage holds a sample with its surface facing

down. The tip is then brought to the sample within a few angstroms from below using the coarse positioner and the piezo-driven fine positioner. The tip movement and positioning are monitored using an external CCD camera as well as the STM program, which automatically brings the tip towards the surface within the specified tunneling current limit.

Commercially made or homemade tips can be used for STM studies. The homemade tips are made of tungsten wires. They are electrochemically etched using the dc drop-off method [28, 29]. The tip etching tool is shown in Fig. 2.9. A piece of W wire is held from the top where a positive voltage will be applied to make it an anode.

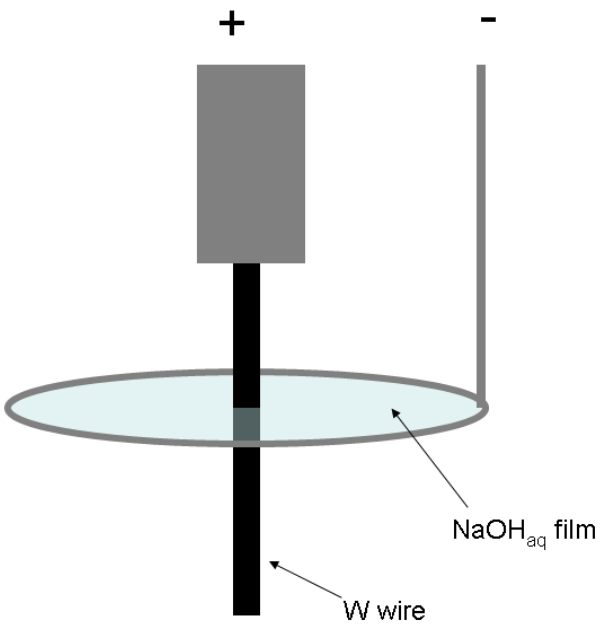

FIG. 2.9. The setup of making electrochemical etching tip.

A film of an electrolyte, usually an aqueous solution of NaOH, is formed on a metal hook, which serves as the cathode. The W wire is then passed through the center of the ring. When the voltage bias is applied, etching occurs at the air-electrolyte interface (the top surface of the film). Bubbles are generated around the hook during the etching. The amount of bubbles and their sizes can be used as an empirical guide to optimize the etching rate. Once the neck of the wire is etched thin enough, the weight of the wire itself fractures the neck. The lower half of the wire drops off on a sponge tip holder. The applied voltage should be turned off immediately to prevent the tip from further etching. The two broken segments of the W wire typically show different shapes of their necks (Fig. 2.10). The neck of the upper half of the wire tends to be shorter and curved, whereas the lower half usually has a longer neck. The tips are rinsed with deionized water to remove the residual electrolyte. Experience shows that a tip with a

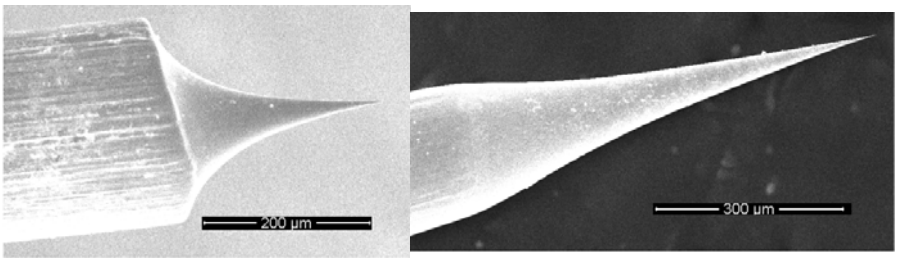

FIG. 2.10. Scanning electron microscope (SEM) images of electrochemical etching tips. Left (right) image is from the upper (lower) half of the W wire. Different radius of tip curvature is observed.

desired shape or curvature can be obtained, to a certain extent, through the combination of the etching time, the shut-off time after the drop of the lower half tip (the power supply is manually controlled here), the concentration of the electrolyte, and the amount of etching current. The electrochemically etched tip is not yet atomically sharp and needs additional *in situ* treatments. One treatment is sharpening the tip by field emission in UHV. A high voltage (potential) is applied to the tip for a short duration. The W atoms near the end of the tip are attracted to the apex by the high field and stripped off to form an atomically sharp end [30]. Another popular method is to just scan a standard sample such as Si, Au or even graphite. During repeated scanning, the tip becomes sharpened under tunneling bias. During this time, the tip can unexpectedly and spontaneously pick up or drop atoms. When the tip sharpens to just one atom at the end, it can provide atomic resolution images of the surface.

In order to generate a tunneling current and subsequently map surface images, a bias voltage is applied between the sample and the tip (Fig. 2.11). If the voltage is kept at a constant value, the tip stays at a constant height during scanning. The tunneling current varies in response to the surface morphology. This is known as the constant voltage or height mode. On the other hand, the tunneling current can be kept at a constant value

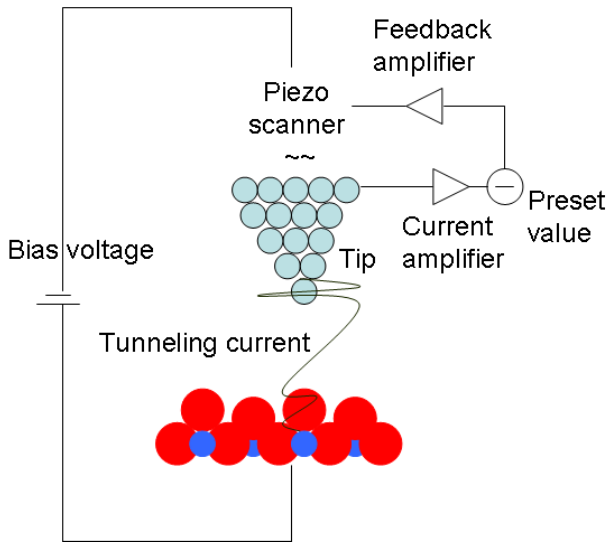

FIG. 2.11. The scheme of scanning tunneling microscope.

specified by a user. When the constant current mode is employed, the tunneling current through a current and a logarithmic amplifier is compared with a reference voltage. The difference or the error signal is then processed by the feedback loop of the electronics to drive the z piezo electric scanner. Therefore, the z position of the tip is regulated during the scan to maintain a constant tunneling current. As a result, a contour map of the equal tunneling-current surface is generated, which indicates the density of states on the surface. In general, an STM image represents the convolution of the electronic density of states and the surface topography. More discussion on the operating principle of STM is presented in Chap. 3.

CHAPTER THREE

Theory

3.1 LEED Kinematics

The kinematic theory of electron scattering, also known as single scattering theory, describes the simplest model for the electron scattering phenomena. In this model, an electron that has been scattered once by an atom will not be scattered again by another atom. The scattering theory together with energy conservation is routinely used to predict the positions of the diffraction spots in a LEED pattern. It further allows the identification of the kinematic peak positions in I-V curves [31]. In an experiment, the vast majority of the incoming electrons suffers inelastic scattering and is not detected. Only 1 to 5 percent of them are elastically scattered and measured as diffraction spots [19]. Even for diffracted electrons a significant portion of them still have small energy losses to phonons, usually on the order of meV at the surface. However, the energy loss is much smaller than a typical instrumental resolution of 0.2 eV. So the treatment of an entire diffraction spot as elastically scattered electrons is justified in general [27].

In the kinematic theory, the incident plane wave of an electron is expressed as

$$\psi_i(\vec{r}) = A_o \exp(i\vec{k}\cdot\vec{r}) \tag{3.1}$$

where A_o is a constant, $\vec{k}$ is the incident wave vector, and $\vec{r}$ is the position vector. The diffracted or elastically scattered wave within the single scattering approximation can be written as

$$\psi_s = A_o\left[\sum_n \alpha f_n(\vec{s})\exp(i\vec{s}\cdot\vec{r}_n)\right]\exp(i\vec{k}'\cdot\vec{r}) \tag{3.2}$$

where $f_n(\vec{s})$ is the atomic scattering factor for the n^{th} atom at position $\vec{r}_n$, $\vec{s} = \vec{k}' - \vec{k}$ is the momentum transfer, and $\vec{k}'$ is the wave vector of the scattered wave. Because the energy is conserved,

$$E = \frac{h^2}{2m}\left|\vec{k}\right|^2 = \frac{h^2}{2m}\left|\vec{k}'\right|^2 \quad \text{or} \quad \left|\vec{k}\right|^2 = \left|\vec{k}'\right|^2 \tag{3.3}$$

The sum $\sum_n f_n(\vec{s})\exp(i\vec{s}\cdot\vec{r}_n)$ in (3.2) is called the structure factor S in the diffraction theory as it contains information on the positions and the types (i.e. $f_n(\vec{s})$) of atoms. Since the LEED has a two-dimensional pattern that arises from the lattice parallel to the surface, the atomic position vector can be written as

$$\vec{r}_n = \vec{R}_p + m_1\vec{a}_1 + m_2\vec{a}_2 \tag{3.4}$$

where $\vec{a}_1$ and $\vec{a}_2$ are the two basis vectors of the surface lattice, m_1 and m_2 are integers, and $\vec{R}_p$ are the locations of the atoms within one unit cell. The structure factor then can be written as

$$S^{(2)} = \sum_n f_n(\vec{s})\exp(i\vec{s}\cdot(\vec{R}_p + m_1\vec{a}_1 + m_2\vec{a}_2)) = \left[\sum_p f_p(\vec{s})\exp(i\vec{s}_{//}\cdot\vec{R}_p)\right]\left\{\sum_{m_1 m_2}\exp\left[i\vec{s}_{//}\cdot(m_1\vec{a}_1 + m_2\vec{a}_2)\right]\right\} \quad (3.5)$$

with $\vec{s}_{//}$ being the component of $\vec{s}$ parallel to the surface. The sum over the lattice vectors in the second curly bracket must satisfy the periodic boundary conditions: $\psi_i(\vec{r} + m_1\vec{a}_1 + m_2\vec{a}_2) = \psi_i(\vec{r})$. The sum becomes proportional to the Dirac delta function $\delta(\vec{s}_{//} - \vec{g}^{(2)})$, where $\vec{g}^{(2)}$ is any of the two-dimensional reciprocal lattice vectors of the surface lattice $(\vec{a}_1, \vec{a}_2)$

$$\vec{g}^{(2)} = h\vec{g}_1 + k\vec{g}_2, \text{ (h, k integers)} \quad (3.6)$$

with

$$\vec{g}_1 = 2\pi\frac{\vec{a}_2\times\vec{n}}{\vec{a}_1\cdot(\vec{a}_2\times\vec{n})}$$
$$\vec{g}_2 = 2\pi\frac{\vec{n}\times\vec{a}_2}{\vec{a}_1\cdot(\vec{a}_2\times\vec{n})} \quad (3.7)$$

and $\vec{n}$ is the normal vector pointing out of the surface. The generalization to the three-dimensional lattice may be easily worked out by adding one more lattice vector in Eq. (3.4) and replacing the normal vector by the third lattice vector in Eq. (3.7). The delta function embodies the scattering condition or the Bragg condition, that is

$$\vec{s}_{//} = \vec{k}'_{//} - \vec{k}_{//} = \vec{g}^{(2)}. \quad (3.8)$$

By squaring the both sides, Eq. 3.8 can be rewritten as $2\vec{k}_{//} \cdot \vec{g}^{(2)} = \left|\vec{g}^{(2)}\right|^2$. With the simple geometry illustrating Eq. 3.8 depicted in Fig. 3.1, the more familiar form of the Bragg condition

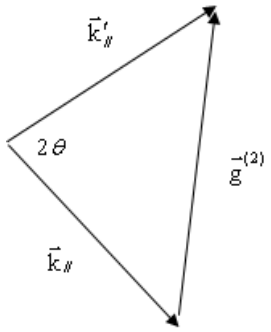

FIG. 3.1. The geometry illustrating Eq. 3.8.

$$\frac{2\sin\theta}{\lambda} = \frac{n}{d}, \tag{3.9}$$

can be recovered where d is the distance between the rows of surface atoms or surface unit cells. In summary, the low energy electron waves scattered from a single crystalline surface can produce the diffraction maxima upon fulfilling the Bragg condition. The Bragg condition essentially states that the diffraction maxima arises as the difference in pathlength between reflections from periodic surface unit cells equals an integer multiple of the wavelength. Therefore the LEED pattern can be readily used to extract information on the periodicity and the symmetry of the surface structure.

3.2 LEED Pattern of Stepped Surfaces

For a LEED pattern generated from a simple surface, the extraction of structural information such as the size and the shape of the unit cell is straightforward. However, LEED patterns from stepped or faceted surfaces can become increasingly complex and difficult to interpret. In such a case, the Ewald construction can be useful in order to visualize and understand the diffraction pattern that arises from a model stepped surface. The method of Ewald construction utilizes a geometric construction in k-space to help

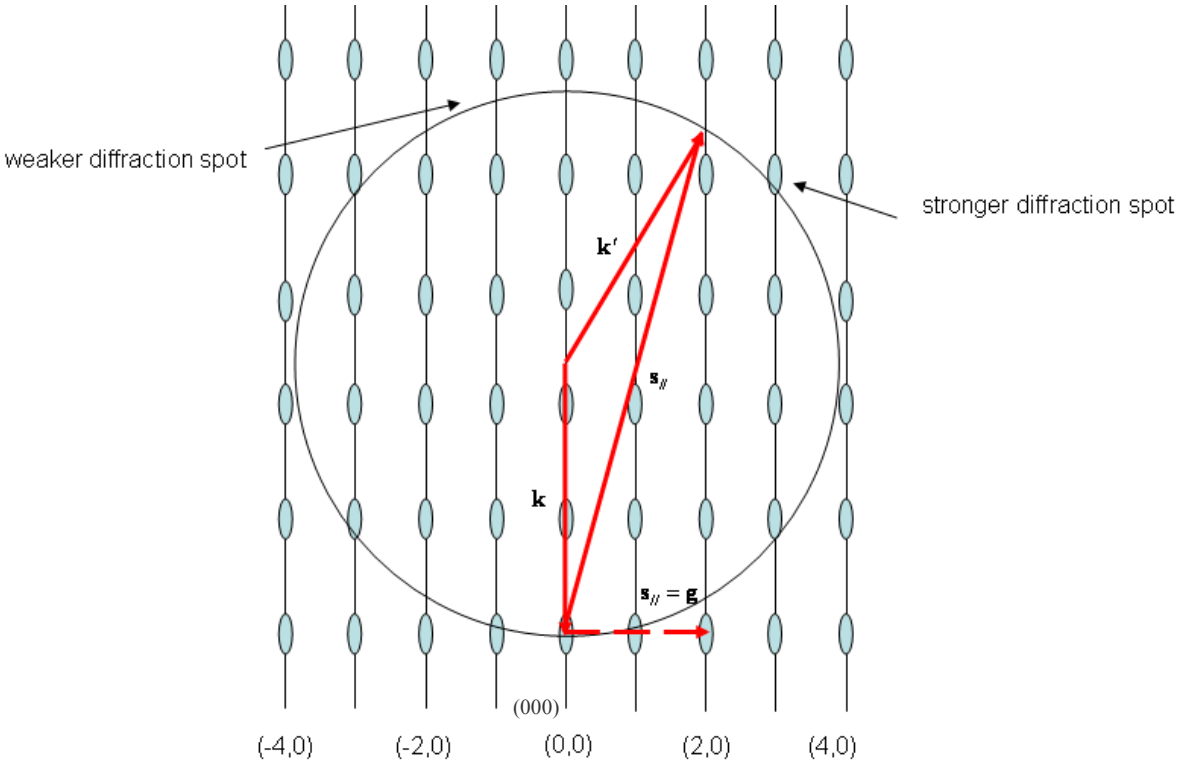

FIG. 3.2. Ewald construction of quasi-2D scattering for a non-stepped surface [31].

picture the Bragg conditions, and the observed LEED peaks, consequently, allow for the deduction of the crystal structure form.

Before applying the Ewald construction to the stepped surface, an Ewald construction of 3D scattering for a simple, flat surface is introduced first to illustrate the essential features of predicting a LEED pattern (Fig. 3.2) [31]. For an idealized two-dimensional surface, the periodicity along the surface normal is broken, and the periodic distance is regarded as infinite. Then, the reciprocal lattice 'points' along the surface normal are infinitely dense as the distance between two adjacent reciprocal points is inversely proportional to the distance between two adjacent lattice points in real space. These infinitely dense reciprocal points form a reciprocal rod that characterizes the surface periodicity and symmetry in diffraction. For a real single crystal surface, sub-surface layers are periodic along the surface normal. The crystal structure perpendicular to the surface can contribute to the scattered intensity as in the X-ray diffraction. In this case, the reciprocal rods shrink to spots.

In an Ewald construction, a sphere of radius k can be drawn given the incident wave vector $\vec{k}$. According to the LEED experimental geometry, the wave vector $\vec{k}$ is pointed toward the surface and positioned with its head at the intersection of (0,0) rod and the sphere. The points on the sphere can represent elastically scattered waves since they

have the same radius or energy. As the energy of the electron beam increases (decreases), the radius of the sphere increases (decreases) as well. The centers of the spheres move along the (0,0) rod so that all the spheres remain in contact with the (0,0,0) reciprocal lattice point, which is superimposed on the surface. When the sphere intersects a reciprocal lattice rod, the Bragg condition in Eq. (3.8) is fulfilled. The intersection point also represents the parallel component of the scattering vector being

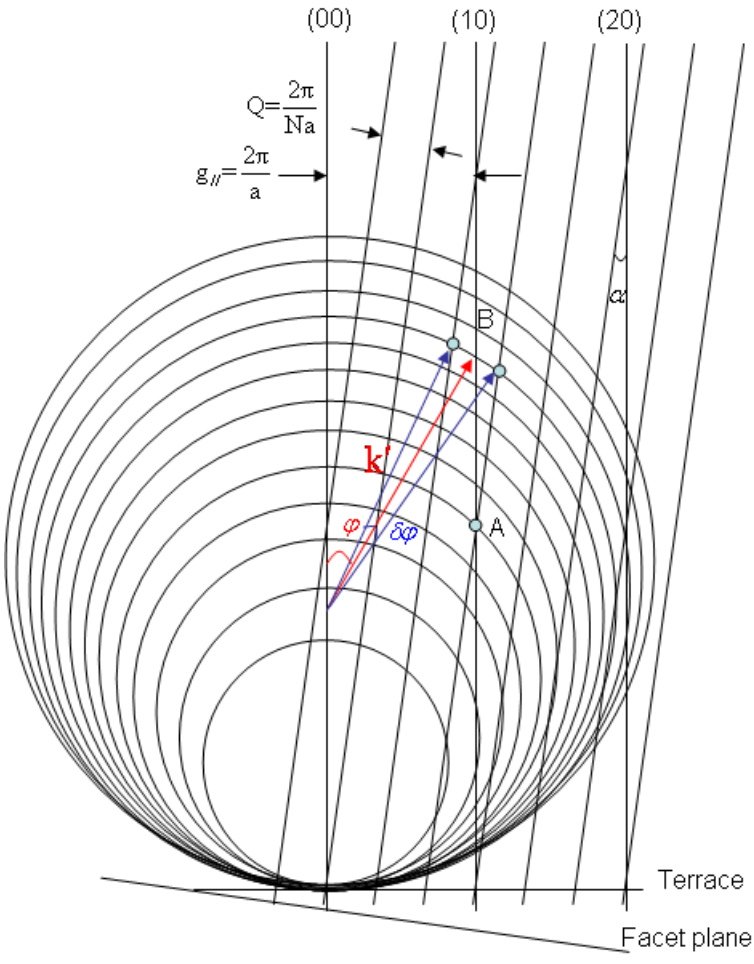

FIG. 3.3. Ewald construction for a stepped surface [27, 31].

equal to a surface reciprocal lattice vector. As the incident energy varies, the Ewald sphere may pass successively through the spots along the rods. As a result, the intensity of the corresponding LEED spot may modulate periodically.

For a stepped surface, two sets of rod arrays in the reciprocal space are necessary to describe the periodic structure shown in Fig. 3.3 [27, 31]. The vertical array represents the reciprocal lattice of the flat terrace. The spacing of the rods is $g_{//} = g_{hk}$. However, the terrace is not infinitely extended as the simple flat surface but has a finite width. This finite width broadens the reciprocal lattice rods, because the structure factor in Eq. 3.2 no longer produces a sharp delta function-like condition. This reciprocal rod array will be referred to simply as the terrace rods. The other tilted array with the rod spacing Q in the reciprocal space results from the periodic steps of the surface. The tilt angle α is equal to the angle of inclination for the step plane with respect to the terrace. The reciprocal lattice rods of the stepped surface are packed in inversely proportional to the terrace width Na, thus the rod spacing Q is equal to $\frac{2\pi}{Na}$, where a is the lattice constant of the terrace surface. Due to the structure of the flat terraces, the step rods are important only in the proximity of the terrace rods [27, 31, 32].

Several Ewald spheres with increasing radii are drawn in Fig 3.3. As an Ewald sphere intersects the reciprocal lattice rods, two cases may be considered. The first case

is when the sphere crosses where a step rod would meet with a terrace rod, for example, the point A in Fig. 3.3. In this case, only a single spot is observed as in the LEED from the simple surface. The second case is when the sphere crosses two nearby step rods at the same time. An example of such a point is labeled as B in Fig 3.3. In this case, a

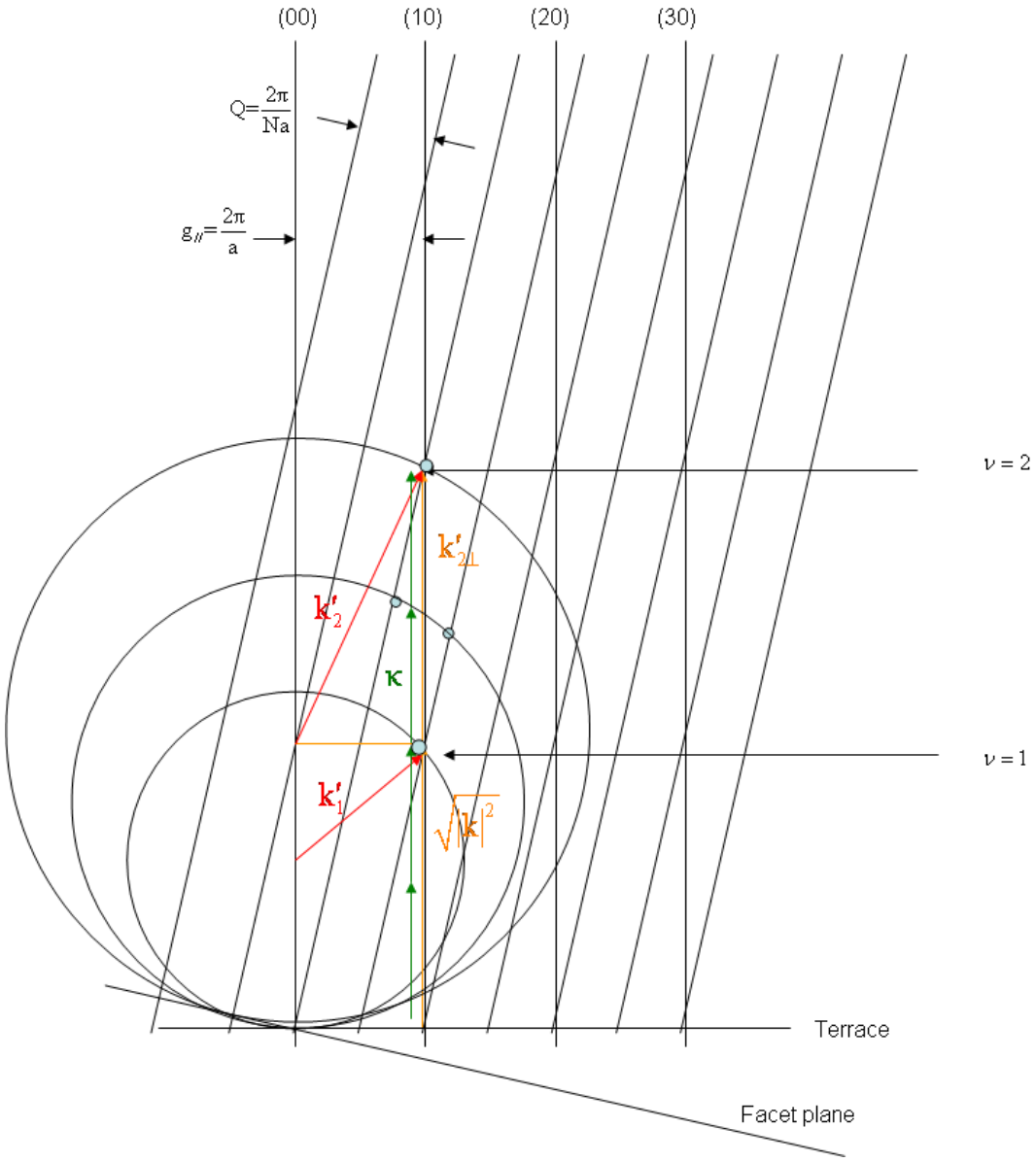

FIG. 3.4. Ewald construction for a stepped surface illustrating Eqs 3.12 and 3.13.

double spot is observed. As the radius of the Ewald sphere increases with increasing electron energy, a diffraction spot may change its appearance alternately between a single and double spot.

From the geometry depicted in Fig. 3.3, one can derive an expression for the angular splitting of a scattering angle φ of a LEED spot, $\delta\varphi$. For a small angle of inclination α

$$k'\delta\varphi \cong \frac{Q}{\cos(\varphi\text{-}\alpha)} \approx \frac{Q}{\cos\varphi} \text{ or } \delta\varphi = \frac{Q}{k'\cos\varphi} \tag{3.10}$$

$$\text{Since } k = k' = \frac{2\pi}{\lambda},\ \delta\varphi = \frac{Q}{k\cos\varphi} = \frac{\lambda}{Na\cos\varphi} \tag{3.11}$$

The electron wavelength λ corresponds to the energy value at which a LEED spot at a scattering angle φ is split into two. As the energy increases from one value to another, a diffraction beam may alternate from a single spot to double spots. The energies values corresponding to single or double spots are called the characteristic energies [32]. At the characteristic energies one can obtain

$$2\nu\kappa = \sqrt{|\mathbf{k}|^2} + k'_{\perp}, \text{ where } \nu = 1, 2, 3.... \tag{3.12}$$

$$2\nu\kappa = \sqrt{\frac{2mE}{h^2}} + \sqrt{\frac{2mE}{h^2} - |g_{//}|^2} \tag{3.13}$$

κ is the perpendicular distance in reciprocal space between the points of a single and a split spot, for example, the distance between point A and B. ν is the order of the

occurrence for the characteristic energies. This relationship is geometrically shown in Fig 3.4. The inclination angle α may be found from the following equation.

$$\frac{Q}{2\kappa} = \frac{2\pi}{2\kappa Na} = \sin\alpha \tag{3.14}$$

The stepped surface height can then be found with the approximation.

$$\sin\alpha \cong \tan\alpha = \frac{d}{Na} \tag{3.15}$$

3.3 Scanning Tunneling Microscope (STM)

In 1982, the first STM result was published by Binning and Rohrer who were awarded the Nobel Prize five years later [33, 34]. The STM revealed the first real-space atomic image to the world. It was a technological breakthrough, which realized for many a dream of visualizing individual atoms and subsequently manipulating them [35].

When the sample and the tip are brought to each other within several angstroms in a UHV chamber, a measurable amount of tunneling current can be established with a bias voltage applied. To understand the tunneling phenomenon semi-quantitatively, one can use elementary quantum mechanics. Fig 3.5 depicts the potential energy diagrams involving a tip and a surface. The vacuum gap between the tip and the sample forms a potential energy barrier. For simplicity, the tip and the sample are assumed to have the same work function ϕ, the minimum energy for taking an electron from the solid to the

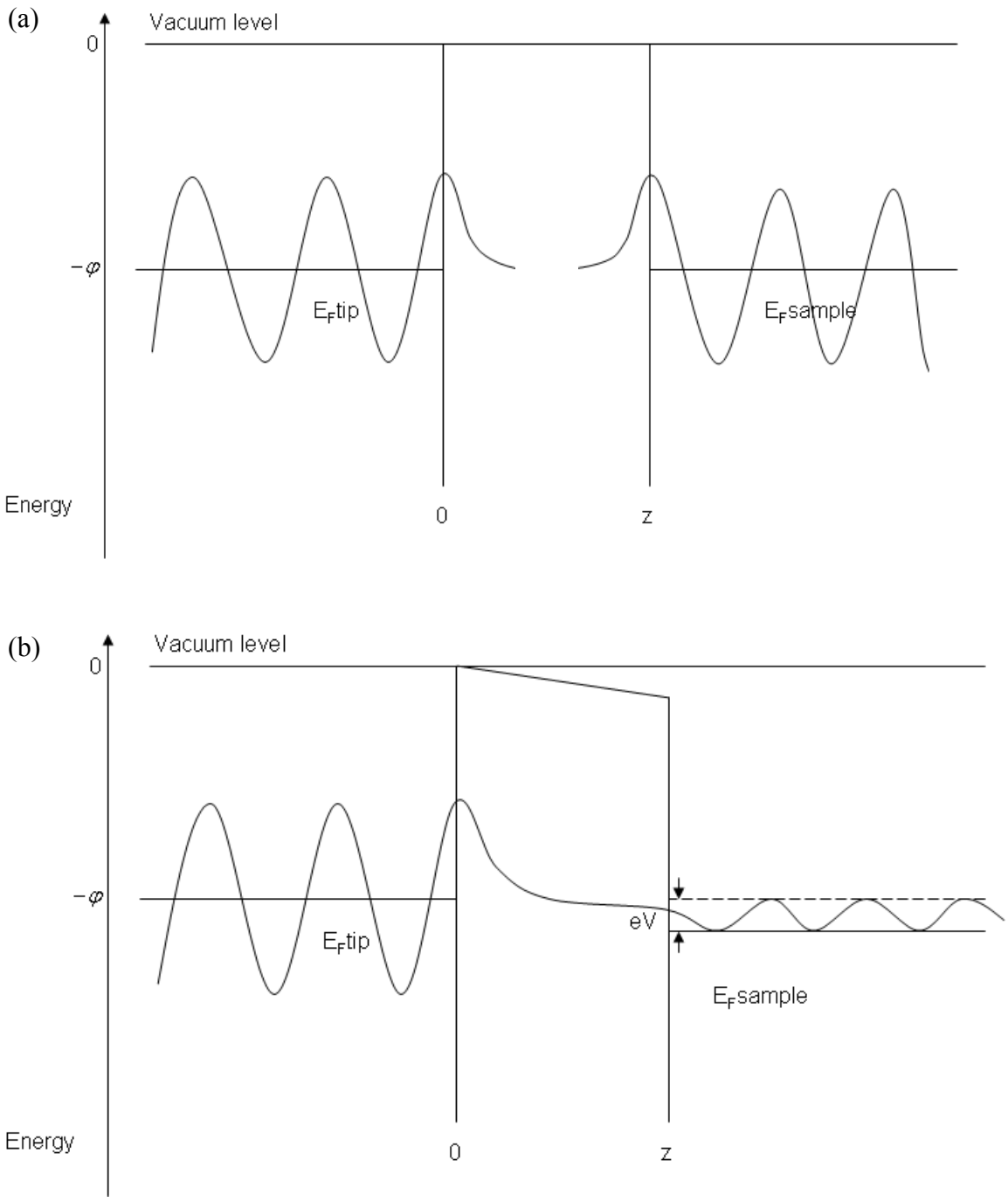

FIG. 3.5. Potential energy diagram of the sample and the tip states. (a) before a positive bias voltage V is applied (b) after a positive bias voltage V is applied, a tunneling current is generated from the filled tip states to the empty sample states [30].

vacuum energy level. In the absence of an external bias, the Fermi levels E_F (the energies of the highest occupied state) for the tip and the sample are aligned to $-\phi$ with respect to the vacuum level.

When a positive bias voltage V is applied to the sample (Fig. 3.5(b)), the Fermi levels in the tip and the sample shift by eV with respect to each other. The electron state $\psi(z)$ in the tip between E_F and E_F – eV satisfies the Schrödinger equation (3.16).

$$-\frac{\hbar^2}{2m}\frac{d^2}{dz^2}\psi(z) + U(z)\psi(z) = E\psi(z) \tag{3.16}$$

The potential barrier $U(z)$ is greater than the electron energy E, and the solution is obtained in Eq. 3.17,

$$\psi(z) = \psi(0)e^{-\kappa z}, \text{ for } U(z) > E \tag{3.17}$$

where the decay constant $\kappa = \frac{\sqrt{2m(U - E)}}{\hbar}$ and m is the electron mass. Eq. (3.17) describes an electron penetrating through the barrier into the classically forbidden region. The tunneling current is proportional to the probability density of observing an electron near z.

$$I \propto e^{-2\kappa z} \tag{3.18}$$

Eq. (3.18) shows that the tunneling current is an exponential function of the distance between the tip and the sample. A quick estimate can be made to gauge the sensitivity. As the tunneling electron states are very close to the Fermi level, U - E is approximately

equal to ϕ. The work functions for the typical materials investigated are about 5 eV [30]. According to Eq. (3.18), the tunneling current decays one order of magnitude per angstrom. Therefore, STM is extremely sensitive to the gap between the tip and the sample and consequently to the corrugations of the surface structure.

For the STM used for this dissertation, the tip was grounded, and the sample was biased with a voltage V. When a positive bias voltage is applied, the tunneling current flows from the occupied states of the tip into the empty states of the sample. If the bias voltage is negative, the electrons flow from the occupied states of the sample to the empty states of the tip. For TiO_2, atomically resolved STM images are obtained generally using a positive sample bias voltage [36]. In this case, the empty states of the TiO_2 surface are imaged. The band structure calculations indicate that the empty states in the conduction band are largely Ti-derived states [37], hence the imaged contrast represents the convolution of the local density of mainly Ti d states and surface topography. There have not been many reported STM images taken at a negative sample bias voltage. With the negative bias voltages (< 3 V) applied, the contrast of the image is greatly reduced [36]. This is in part due to the fact that there are few states for the electrons to tunnel to within the 3 eV band gap with the Fermi level pinned at the bottom of the conduction band.

CHAPTER FOUR

Result and Discussion I

4.1 Bare TiO_2(110)

4.1.1 Pristine TiO_2(110): Mostly Bulk Like Surface

After a TiO_2(110) surface was subject to the cycles of sputtering and annealing as prescribed in Chap. 2, several sets of LEED data were collected. The observations showed that after continuously taking data from the same area for an hour or longer, the contrast of the LEED pattern was reduced. Especially, the diffraction spots at high electron energies became significantly broadened and less well defined. A similar observation has been reported and attributed to the TiO_2 surface being damaged by the electron beam if the same surface area were exposed to an electron beam for a prolonged period of time [38]. Therefore in this work, utmost care was taken to minimize the damage by the incident electron beam and its unintended effect on the I-V data. First, the control parameters of LEED optics were optimized for the spots to be sharply focused before the last cleaning cycle was performed such that the exposure time of the surface to the electron impingement was reduced. Second, before the sample was brought to the

data acquisition position, the LEED optics was warmed up for at least 10 minutes to reach a steady anode current and to avoid the effects of instrument drift. Also, any given area of the surface was limited to about 30 minutes of collecting the I-V data.

Fig. 4.1(a) shows the LEED pattern of the pristine TiO_2(110) surface taken at the electron energy of 110 eV. The smallest repeating rectangular unit cell suggest that the surface possesses the same rotational symmetry of the bulk-terminated TiO_2(110) surface (Fig. 4.1(b)). Since a LEED pattern represents the reciprocal lattice vectors, their lengths are inversely proportional to those of the real space lattice vectors (see Sec. 3.1). Then, the directions of the two surface lattice vectors [001] and $[1\bar{1}0]$ are immediately

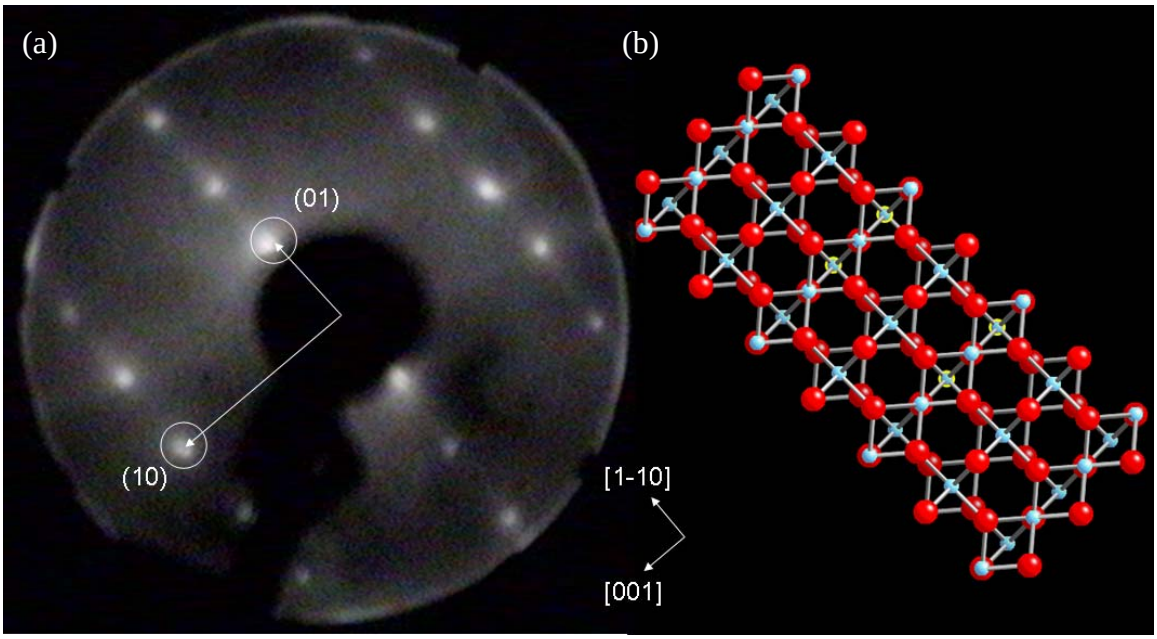

FIG. 4.1. (a) LEED pattern of TiO_2(110) (1 × 1) taken at 110 eV and (b) the corresponding bulk-terminated surface structure.

identified, and the corresponding first order diffraction spots are labeled as (10) and (01), respectively.

To determine the size of the surface unit cell, the scattering conditions in Eq. 3.8 was applied. The equation requires the measurement of the angular position θ of a diffraction maximum at a known energy. One can try to measure the angular positions of (10) and (01) spots from the above energy. In an equally valid and perhaps more convenient way, the incident energy can be adjusted until the spots can be partially blocked by the edge of the LEED optics in the viewport, one spot at a time. Then, the angular position of each spot is the same angle subtended by the optics but measured at a different energy or wavelength. Furthermore, a known reference sample can be used as an internal calibration for the above LEED optics geometry. In this laboratory, Ag(111) was used as a reference surface since its surface relaxations are minimal as the (111) of the face-centered-cubic structure [39]. Its bulk value of 2.89 Å was used to calibrate the optics geometry. A detailed description of calibrating the LEED optics using Ag(111) and calculating the lattice constants is in Appendix A.

The calculated values of the lattice constants are 6.6 Å and 3.1 Å along $[1\bar{1}0]$ and [001], respectively with ± 0.2 Å for experimental uncertainty. A number of experimental sources can contribute to the estimated uncertainty of 0.2 Å, but most

significant sources of errors include the finite beam size, the finite energy resolution, and the uncertainty in determining the sample-to-optics distance. For instance, the LEED spots appeared exactly at the edge of the LEED screen even though the energy was varied by ± 3 eV. Also the z-retraction distance of the LEED optics might have been slightly different between each operation, which could affect the estimated sample-to-screen distance. Within the uncertainty, the measured lattice constants are essentially identical to the bulk values of 6.491 Å along the $[1\bar{1}0]$ and 2.953 Å along the [001] directions. Hence this surface is referred to as the bulk-like terminated surface or the (1 × 1) TiO_2(110).

The (1 × 1) TiO_2(110) may possess the bulk-like symmetry and periodicity, but it is far from the ideal surface. As mentioned in the introduction, there may be many intrinsic defects present on the surface such as O vacancies, Ti interstitials, and step edges. A typically prepared (1 × 1) TiO_2(110) may contain up to several percent of a monolayer (ML) of oxygen vacancies arising from the sample preparation processes. Such an amount is still too small to be detected with a traditional macroscopic tool like X-ray photoelectron spectroscopy (XPS) [40] as its signal is averaged over several layers deep below the surface. Similarly, the O vacancies do not significantly influence the LEED

patterns as they are randomly distributed throughout the surface; although, their presence has been clearly documented using STM [41].

Although the symmetry and the size of the surface unit cell can be extracted by analyzing the spot positions, the positions of Ti and O atoms within the unit cell can not be determined. Instead this information can be obtained by studying the I-V data from diffracted beams. For a complete quantitative analysis, one must employ multiple scattering theory since kinematic theory is inadequate to predict the intensity of a diffraction spot as a function of the electron energy [27, 31]. In practice, the theoretically calculated I-V curves are obtained for each beam for given structural candidates. Then they are compared to the experimental ones, and through an error analysis, for example Pendry's R-factor analysis [42], the model structure that provides the lowest R-factor is proposed to account for the experimental LEED I-V data. Since multiple scattering theory was not used in this work, our data was compared to a similar measurement reported by another group [43].

Fig. 4.2 shows the LEED I-V data from (1 × 1) TiO_2(110) with the sample temperature of about 220 K as well as the data by Lindsay *et al*. [43]. It is easily seen that most of the major peaks from the two sets are in good agreement. Particularly, (01)

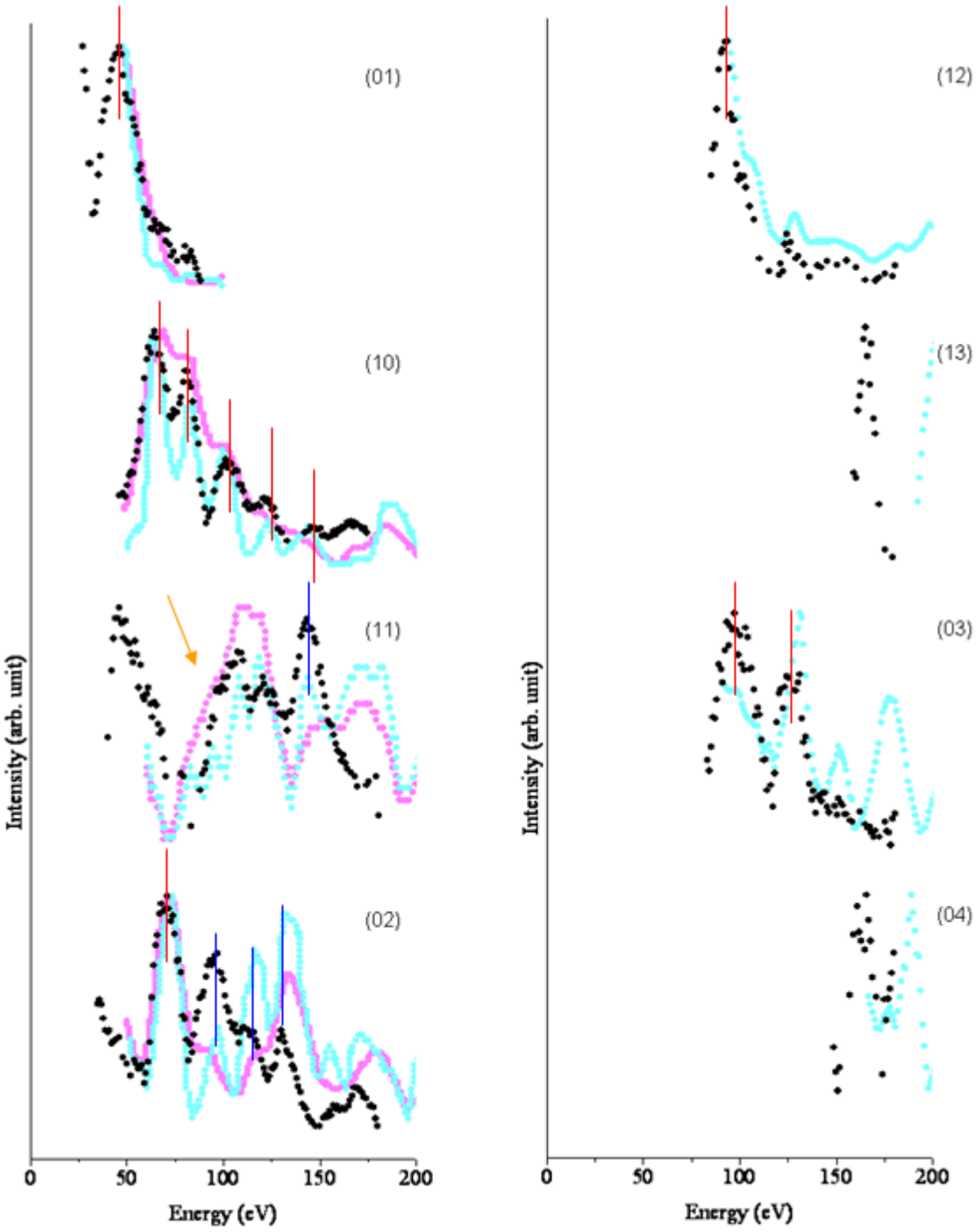

FIG. 4.2. LEED IV of a TiO_2(110) (1 × 1) surface. Black curves are data taken at low temperature (LT) of 220 K at LSAM. The light cyan and pink curves are redrawn from the experimental data and theoretical intensities reported by Lindsay *et al*. [43].

and (10) beams from the two sets show that all the major peaks are at the same positions and that their intensity anisotropy also agree well with each other. Also it is noteworthy that the energy ranges for our I-V curves generally start lower than those of Lindsay's (i.e. (01), (11), (02), (12), (13), (03), and (04) beams) due to the ability to maintain a well-focused electron beam even at very low energy using the VSI optics. On the other hand, Lindsay's data set shows the I-V curves extending to higher energy values probably due to the larger optics used. Thus our data sets complement Lindsay's data sets.

There are a few significant discrepancies between the data sets as well. For example, for the (11) beam, Lindsay 's I-V curve apparently reveals that the peaks in the energy range from 80 to 106 eV are better resolved than the corresponding ones in our data. However, the theoretically calculated curve appears to be a better fit to our data. Also for the (02) beam, the two sets of data do not agree on the relative intensities of the peaks between 90 and 150 eV whereas the position and the number of the peaks are the same. A similar observation was reported on the TiO_2(001) surface, where multiple I-V data sets were taken with increasing and decreasing energy at different area of the surface [38]. The comparison of the data sets showed that the intensities of the peaks varied whereas the number of peaks and their positions remained consistent among the different sets. It was concluded that relative intensities of the peaks were susceptible to

disordered structures on the surface introduced through the damages by the electron beam. On the other hand, the number of peaks and the peak positions were more directly related to the periodic nature of the surface as discussed in Secs. 3.1 and 3.2. Therefore, it is inferred here that the two surfaces might have different disordered local structures.

Using the LEED data, the atomic positions within the first seven layers of TiO_2(110) are determined [43], and their displacements from the bulk positions are summarized in Table 4.1. The positions determined by the LEED are further compared to those

TABLE 4.1. Atomic displacements (Å)of TiO_2(110) surface from their bulk positions as determined by surface x-ray diffraction (SXRD) [44] and LEED [43].

Atom	SXRD [44]	LEED [43]
Ti(1)	0.12 ± 0.05	0.25 ± 0.03
Ti(2)	- 0.16 ± 0.05	- 0.19 ± 0.03
Ti(3)	- 0.09 ± 0.04	- 0.09 ± 0.07
Ti(4)	0.07 ± 0.04	0.14 ± 0.05
O(1)	- 0.27 ± 0.08	0.10 ± 0.05
O(2)[110]	0.05 ± 0.05	0.27 ± 0.08
O(2)[$1\bar{1}0$]	- 0.16 ± 0.08	- 0.17 ± 0.15
O(3)	0.05 ± 0.08	0.06 ± 0.10
O(4)	0.00 ± 0.08	0.00 ± 0.08
O(5)[110]	0.02 ± 0.06	0.06 ± 0.12
O(5)[110]	- 0.07 ± 0.06	- 0.07 ± 0.18
O(6)	- 0.09 ± 0.08	0.00 ± 0.17
O(7)	- 0.12 ± 0.07	0.01 ± 0.13

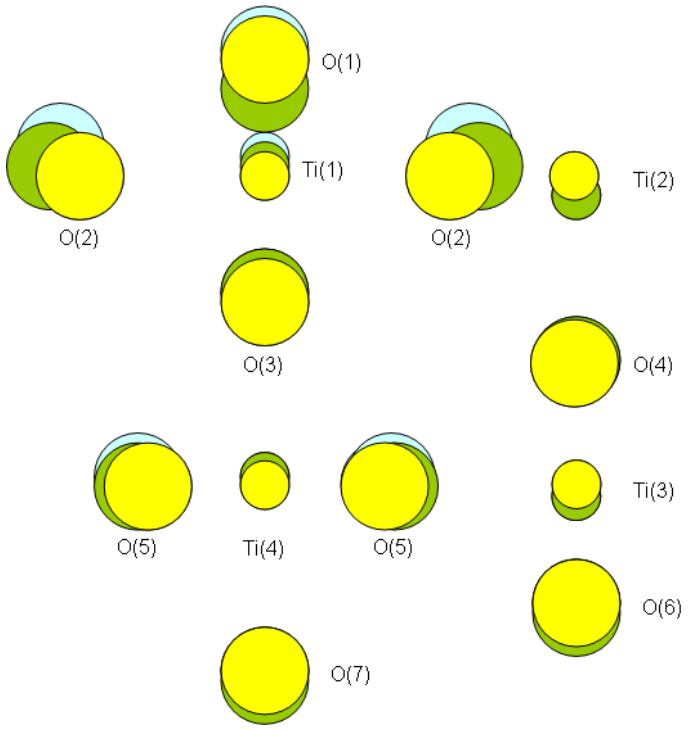

FIG. 4.3. Comparison of the atomic displacements in a unit cell of TiO_2(110) surface determined by surface x-ray diffraction (SXRD) [44] and LEED [43] colored with green and light cyan, respectively. The atoms at the bulk positions are colored with yellow. The larger circles are oxygen atoms, and the small circles are titanium atoms. The displacements show the relative positions not to scale.

determined by the surface x-ray diffraction (SXRD) [44]. For easy visualization, the key traits of the atomic displacements proposed by the two different methods are schematically presented along with the bulk-terminated structure in Fig. 4.3. In general, both methods indicate that vacuum termination of TiO_2(110) surface influences mostly the first two atomic layers. They agree that the 6-fold coordinated Ti atom (Ti(1)) is relaxed outward to the vacuum whereas the 5-fold coordinated Ti atom (Ti(2)) is relaxed

inward toward bulk (Table 4.1 and Fig. 4.3). Also, in-plane oxygen atoms (O(2)) are predicted to move laterally toward the 5-fold coordinated Ti atom (Ti(2)) by both methods.

However, the major discrepancy between the LEED and the SXRD structures is found for the 2-fold coordinated, so-called bridging oxygen atom (O(1)). The LEED data suggests that the oxygen atom is either near the bulk position or slightly moved outward whereas the SXRD predicts that the oxygen moves significantly inward toward the bulk. The atomic displacement of O(1) predicted by SXRD is more consistent with chemical intuition using a simple ionic model; the absence of a Ti cation on the vacuum side of O(1) would result in the oxygen atom being pulled toward Ti(1). Therefore, one of the current LEED projects in LSAM aims at achieving a best-fit structure, which would be more consistent with the SXRD result. One approach is to utilize optimized muffin tin potential in collaboration with Rundgren [45]. In this approach, the calculations of the phase shifts for electron scattering are made with adjustable muffin tin radii. Unlike the conventional methods, the muffin-tin radii of titanium and oxygen are allowed to vary as a function of the electron energy so that the electron wavefunctions do not suffer any possible kinks at the potential boundary. Such extra smooth joining of the

electron wavefunctions across the muffin-tin boundary could allow a much lower R-factor and hence possibly an alternative structure [45, 46].

A (1 × 1) TiO_2(110) was also imaged using STM. Fig. 4.4 shows an atomically

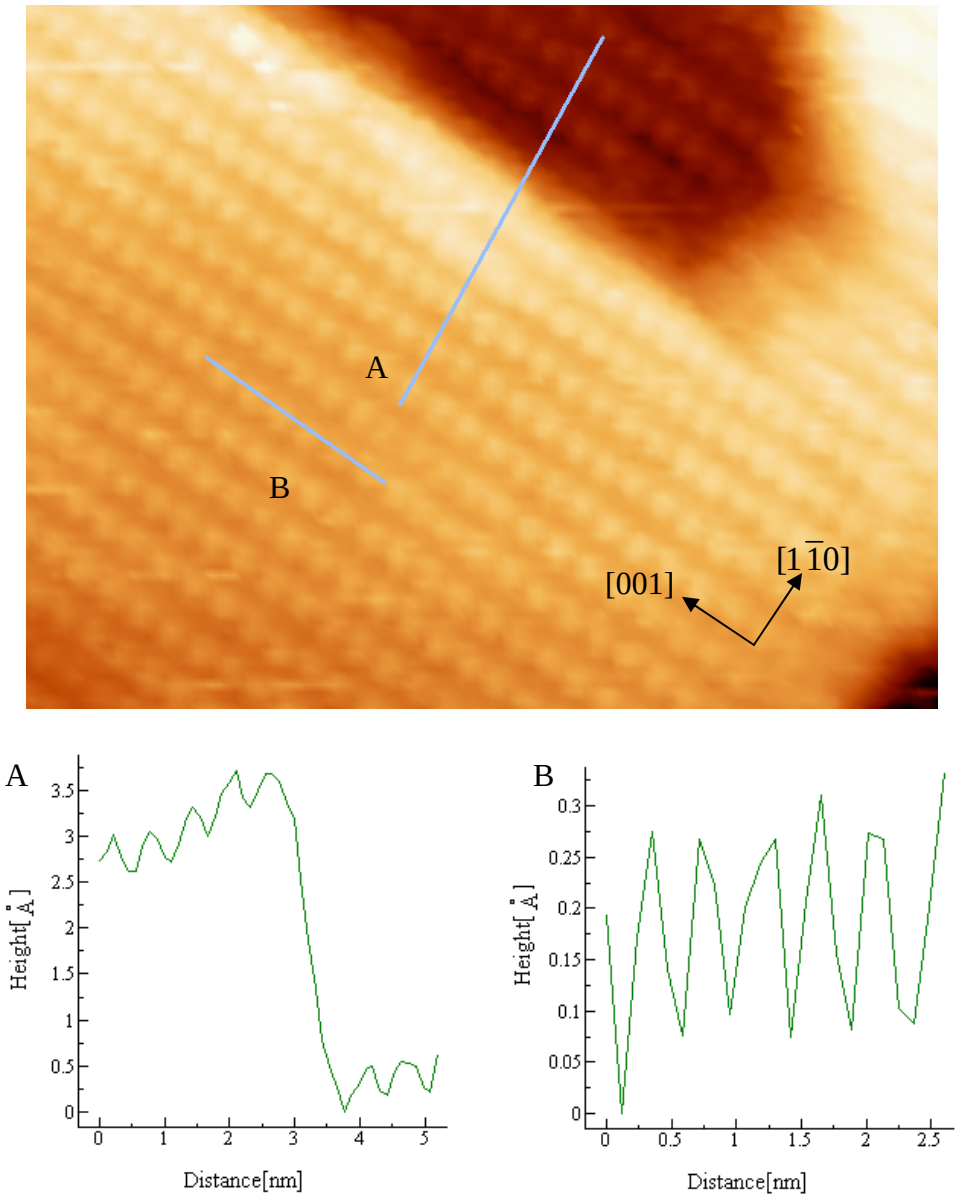

FIG. 4.4. Atomically-resolved STM image of the TiO_2(110) surface and the line profiles.

resolved image of the terraces [47]. The line profile reveals that the height difference between the dark region and the top terrace is about 3.2 Å corresponding to the single-step height of the bulk-terminated TiO_2(110) surface. The surface also exhibits bright and dark rows running along the [001] direction on the terraces. The distance between two adjacent bright rows is about 6.5 Å, which is very close to the bulk value of 6.491 Å along $[1\bar{1}0]$. Each bright row consists of the bright spots lined up with the periodicity of 4 Å along [001]. The measured value is significantly off from the expected value of 2.953 Å. The discrepancy likely results from the tip and thermal drifts of STM [30]. Aside from the instrument effect of the directional distortion, STM shows a nearly perfect, defect-free (1 × 1) TiO_2(110) surface. The assignment of bright and dark rows to either the Ti or O rows has not been easy. However, there now appears to be a consensus that the apparent corrugation between the bright and the dark rows is reversed due to the electronic effects [48]. On the (1 × 1) surface, the bright rows in Fig. 4.4 result from large density of states localized on the 5-fold coordinated Ti^{4+} atoms. The darker rows are assigned to be the bridging oxygen rows, which do not contribute much to the empty states despite the fact that they are physically about 1.5 Å above the plane of the fivefold coordinated Ti^{4+} atoms.

4.1.2 Partially Reduced TiO_2(110): (1×1) Surface with Line Defects

As the pristine surface was subject to an increasing number of preparation cycles, the LEED image continued to display a (1 × 1) pattern without easily discernable changes. However, the gradual change of the sample color from white to blue and eventually to darker blue suggested that overall stoichiometry was reduced significantly enough to alter the optical and electrical properties of the sample [49-51]. Because the (1 × 1) LEED pattern indicated that the long-range order remained the same as the pristine surface, it was believed that these changes were brought by sub-stoichiometric species, which were distributed throughout the sample without any long-range order. The presence of these randomly distributed sub-stoichiometric species can be also gleaned from the LEED I-V data.

Fig. 4.5 compares the LEED I-V data from a partially reduced (1 × 1) TiO_2(110) (black filled circles) to those from the pristine (1 × 1) TiO_2(110) (gray filled circles). For each diffraction beam, major peaks are reasonably well matched between the two sets. Many peaks from the partially reduced surface show their peak positions are shifted to higher energy (ca. 3%), compared to those from the pristine surface: for example, the peak at 50 eV of the (01) beam as well as the peaks of the (10) (11) and (02) beams. The peak shifts might have resulted from different temperatures used for the two surfaces

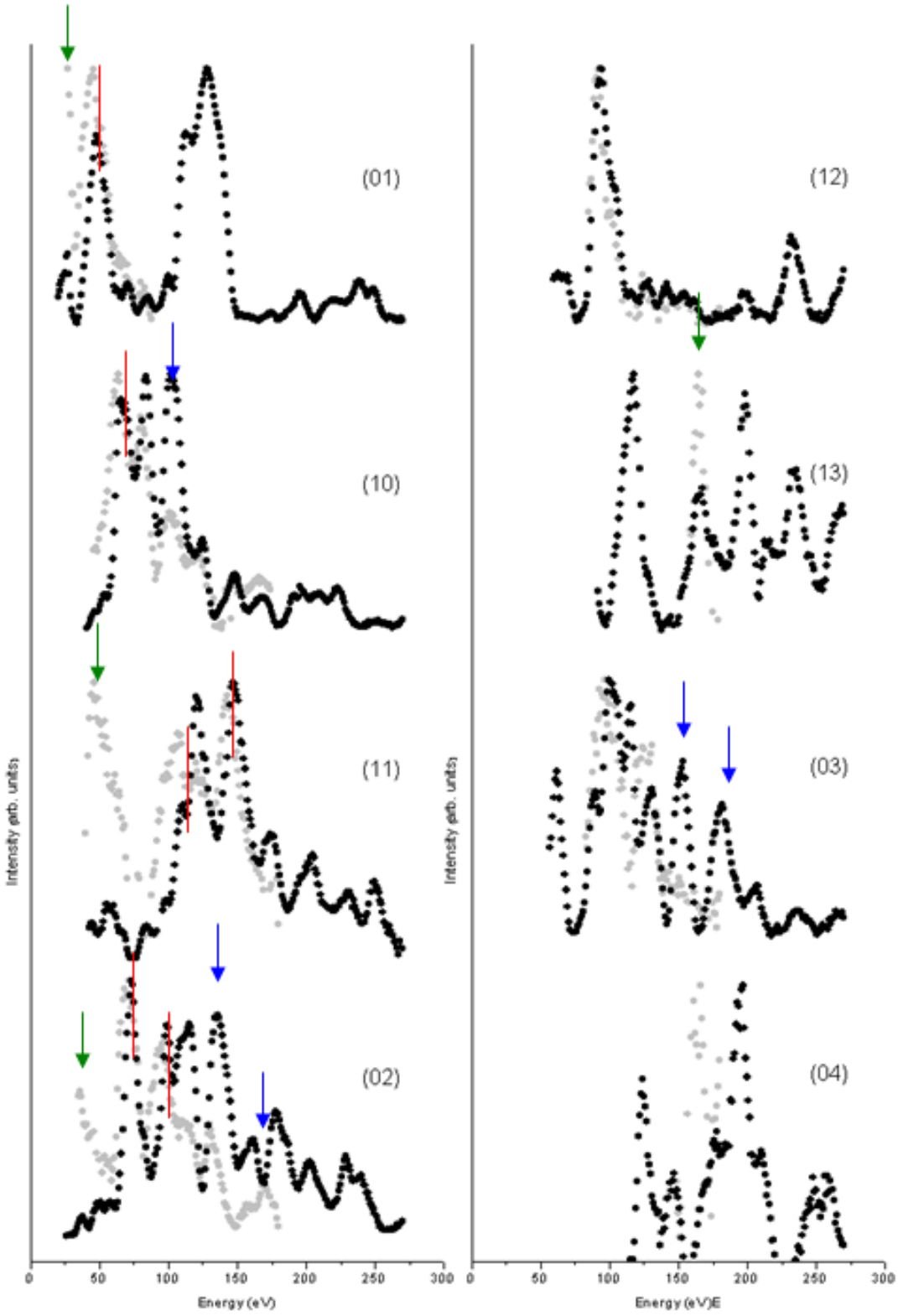

FIG. 4.5. LEED IV of a TiO_2(110) (1×1) surface taken at and room temperature (RT). The light grey cures are redrawn from Fig. 4.2 for comparison.

but also from intrinsic changes in the composition and the conductivity, which might influence the inner potential for electron scattering. More substantially, some peaks from the partially reduced surface show strikingly different intensity profiles, compared to those from the pristine surface. For example, the peaks at 94 eV for the (10) beam, the peaks at 110eV and 135 eV for the (02) beam, the peaks at 160 eV and 180 eV for the (03) beam exhibit significantly enhanced intensities, compared to the corresponding peaks from the pristine surface (Fig. 4.5). On the other hand, the low energy peaks around 30 eV for the (01), (11), and (02) beams from the reduced surface all show greatly suppressed intensities. These contrasts clearly point to a considerable change in the surface morphology and composition taking place on the partially reduced TiO_2(110). A more direct view on the changes taking place on the partially reduced surface can be obtained using STM. A large-area STM scan in Fig. 4.6(a) shows terraces of size at least 200 nm × 30 nm with sharp edges running predominantly parallel to [001] and $[1\bar{1}1]$ directions. At this large scale, the surface appears to be similar to the pristine TiO_2(110). However, a close-up view of the surface reveals that numerous bright strands of several tens of angstroms long are dispersed on the (1 × 1) terraces (Fig. 4.6(b)). Each strand is aligned along [001], but there is no long-range order among the strands.

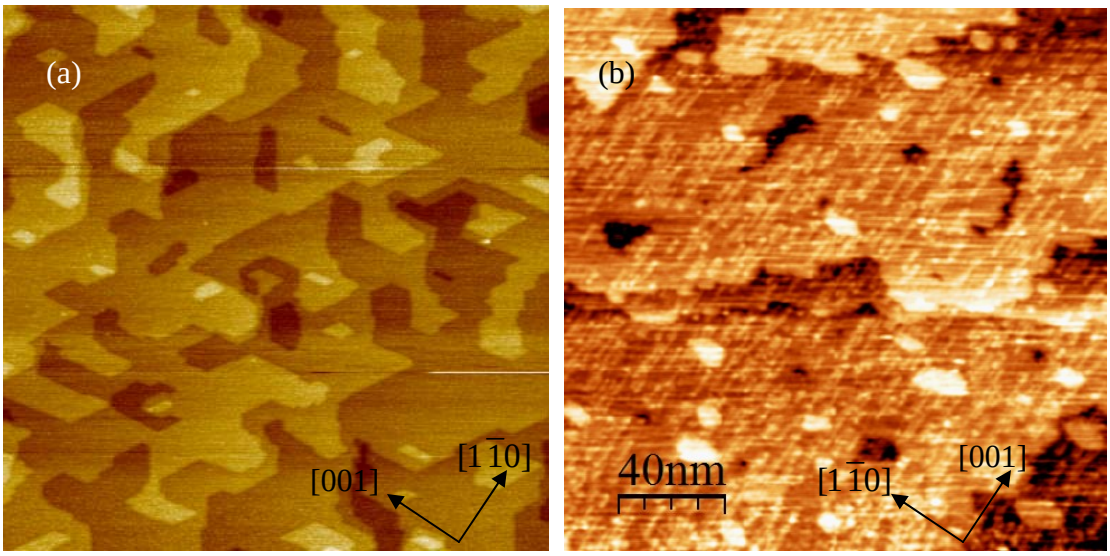

FIG. 4.6. (a) 400 × 400 nm^2 and (b) 200 × 200 nm^2 STM images of a reduced TiO_2(110) (1 × 1) surface taken at RT (bias, 4.0 V; tunneling current 50 pA). The surface is further annealed at 900 °C for five hours.

A higher resolution image further reveals that the bright strands (Fig. 4.7) are typically about 1.6 Å tall, measured from the surface Ti^{4+} rows, and are located right next to the Ti^{4+} rows. The full width at half maximum (FWHM) of the strands ranges from 7 to 9 Å. As the appearance of the strands is correlated with the gradual reduction of the surface [17], they are believed to be defects resulting from oxygen deficiency or of sub-stoichiometric nature. However, both the exact nature and the atomic structure of a strand have been subjects of debate over the past several years. The most recent structural model of the strand proposed by Park *et al*. [52] suggests that Ti interstitials diffused from bulk to surface are coordinated into partially complete oxygen octahedra

that share faces with the substrate octahedral framework. Under an oxygen deficient environment, this face-sharing sub-oxide unit serves as a building block for the strand defects with highly reduced local stoichiometry of Ti_2O.

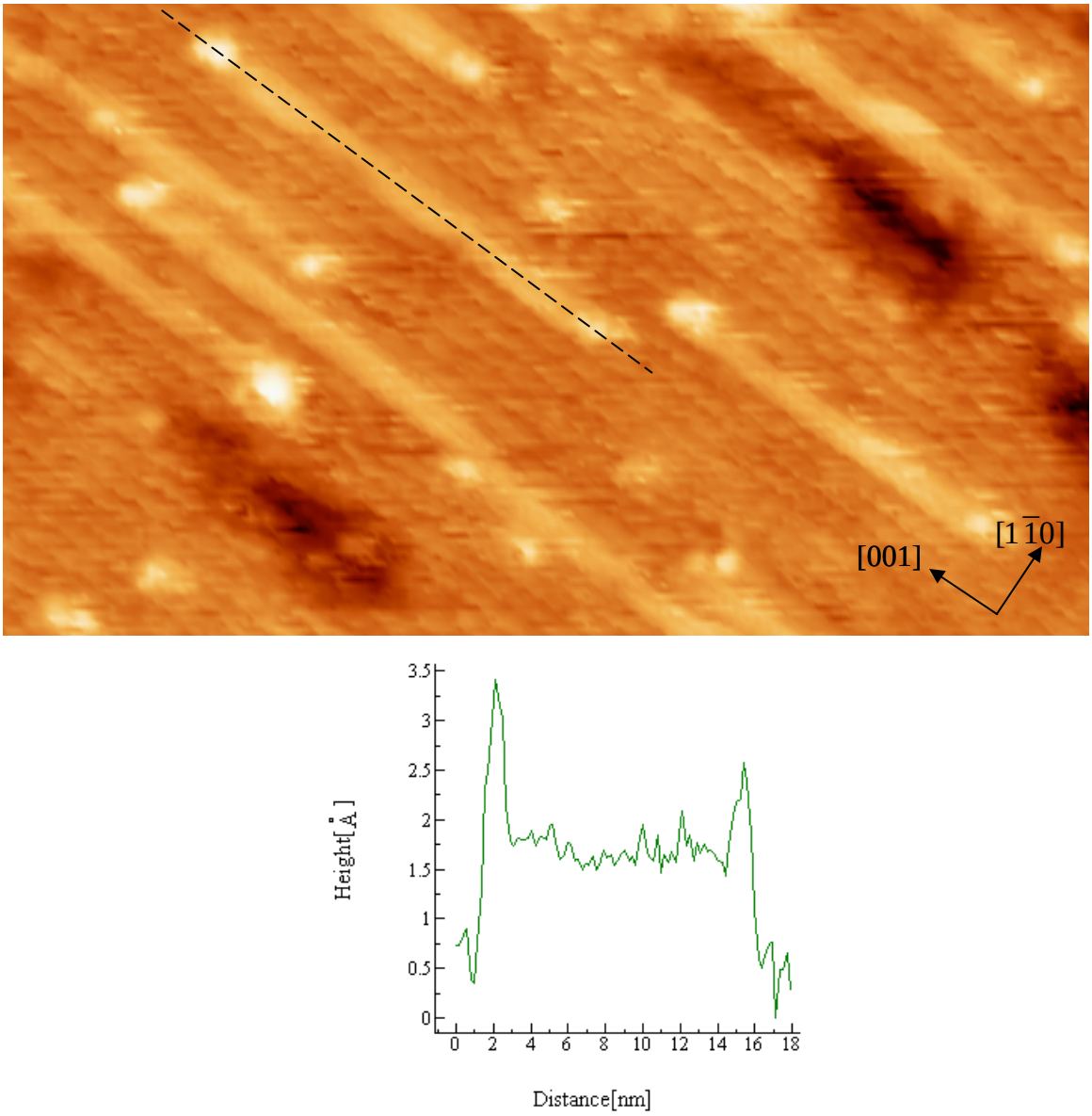

FIG. 4.7. STM image of the line defects.

Also the strands frequently accompany the bright spots at their ends. Unlike the strands, the bright spots span across both Ti^{4+} (bright) and O (dark) rows of the terrace along $[1\bar{1}0]$. Since the width along $[1\bar{1}0]$ is comparable to that along [001], the resulting shape is circular or elliptical. The FWHM of the end spots varies from 4 to 12 Å. However, regardless of the FWHM the heights of bright spots are about 3 Å, which matches to the full-step height of the bulk-terminated surface. These topographical features of the bright spots along with their active role in surface re-oxidation [53, 54] indicate that they might be made of stoichiometric units.

In collaboration with Dr. Meuniers at Oak Ridge National Laboratory (now at Rensselaer Polytechnic Institute), a structural model has been calculated and proposed

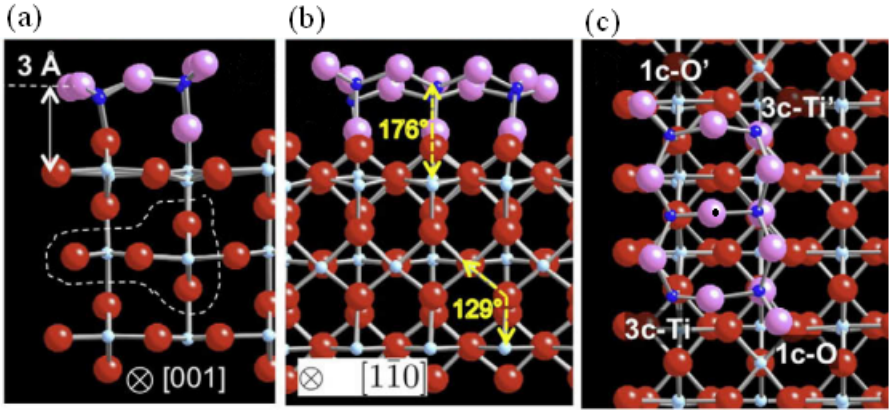

FIG. 4.8. DFT-relaxed structure of a $(TiO_2)_6$ for the dot defect, compared to stoichiometric units in bulk (a dashed loop) viewed along (a) [001], (b) $[1\bar{1}0]$ and (c) (110). (defect and surface Ti: dark and light blue, respectively; defect and surface O: pink and red, respectively) [18].

(Fig. 4.8) [18]. According to the geometry relaxation of the six TiO_2 units using density functional theory (DFT), the most stable positions for each TiO_2 unit are on top of the 2-fold coordinated, bridging O (2c-O) row and about 3 Å above the 5-fold coordinated Ti (5c-Ti) row (Fig. 4.8(a)). As anticipated for a small cluster placed alone on the surface, severe under-coordination forces it to adopt molecular geometry and orientation different from those in bulk rutile. The TiO_2 unit above the 2c-O row turns one of its Ti-O bond axes toward the adjacent TiO_2 unit above the 5c-Ti row. For the TiO_2 above the 5c-Ti row, Ti is lifted up and away from surface while pinned with one of its oxygen atoms onto the surface 5c-Ti. This tilting increases the bond angle (∠ Ti-O-Ti) from 129° in bulk to 176° (Fig. 4.8(b)). As a result of these distortions, Ti is coordinated tetrahedrally with bond lengths of 1.65 Å and 1.87 Å to the 1c- and 2c-O atoms, respectively and 2.00 Å and 2.03 Å to the surface 2c-O atoms. Overall, the distortion and the finite size of the cluster reduce the coordination numbers to 4 or 3 for Ti and 2 or 1 for O, and these atoms of low coordination represent cationic and anionic coordination defects, respectively.

4.2 Surface Modifacation with Au Nanoparticles

4.2.1 Au/TiO_2(110)

As seen in the preceding section, a partially reduced TiO_2(110) surface can become highly inhomogeneous on the microscopic scale with strand and dot defects. However, the distinct shape and height of the nanometer-sized defects allow one to identify them with simple STM topography and *in situ* study of their role in surface chemistry. Fig. 4.9(a) shows a STM image of a clean TiO_2(110) surface prior to Au deposition. Fig. 4.9(b) shows the exact same area after Au deposition for 1 minute at room temperature. The comparison of the STM images shows that the Au clusters are imaged as bright

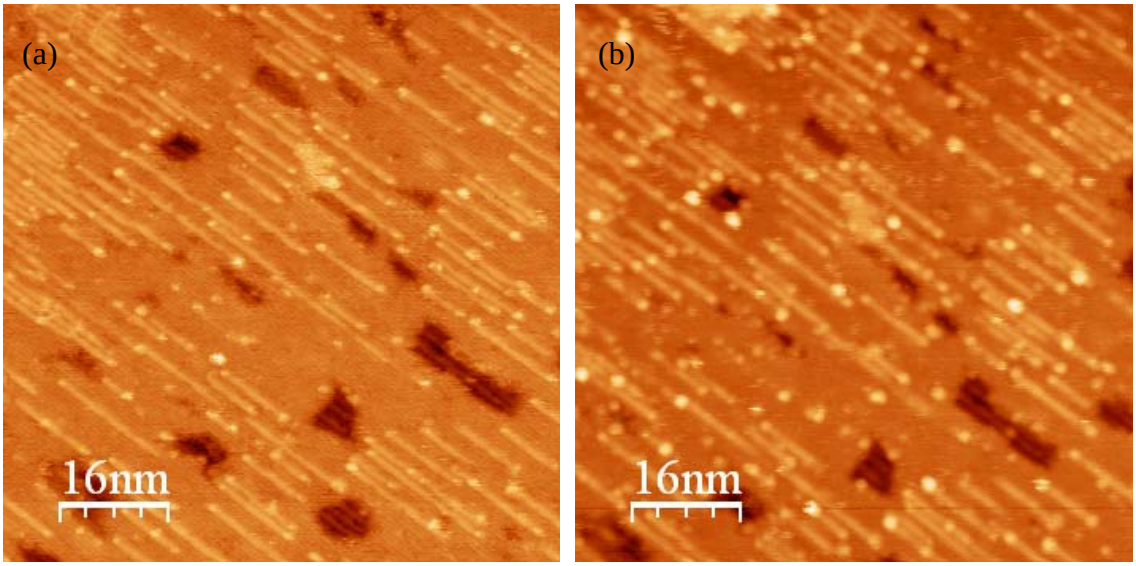

FIG. 4.9. STM images of the reduced TiO_2(110) surface before (a) and after (b) 0.4% ML Au deposition. (80nm × 80nm).

protrusions and that most of them are found preferentially at the bright spots and step edges as well as along strands.

The amount of Au actually deposited on TiO_2(110) can be also estimated by the comparison and quantified in units of monolayer (ML) assuming that the particle density of a gold nano-cluster is the same as that of the packing density of Au(111). As the unit cell of Au(111) ($\sqrt{3}/2 \times (4.08\ Å)^2 \times 2.88\ Å$) contains two Au atoms, the volume per Au atom or the area per Au atom in the close-packed surface can be easily obtained. The surface packing density is calculated as 1.39×10^{15} Au atoms per cm^2 and is defined as 1 ML. Since the total volume of the bright protrusions increases by 8222.95 $Å^3$ due to Au deposition, the amount of Au is obtained by dividing the volume by the monolayer volume. The corresponding ML is 0.00446 or 0.4% ML.

For the 0.4% ML of Au-covered TiO_2(110), the locations of Au adsorption and the size of Au clusters can now be analyzed in detail. 69% of the new clusters are observed

TABLE 4.2. The changes of the shape and height of the clusters after 0.4% ML Au deposition. W± and H± represent increase (decrease) in width and height, respectively.

Change in H\W	W+	W-
H+	40%	0%
H-	20%	5%

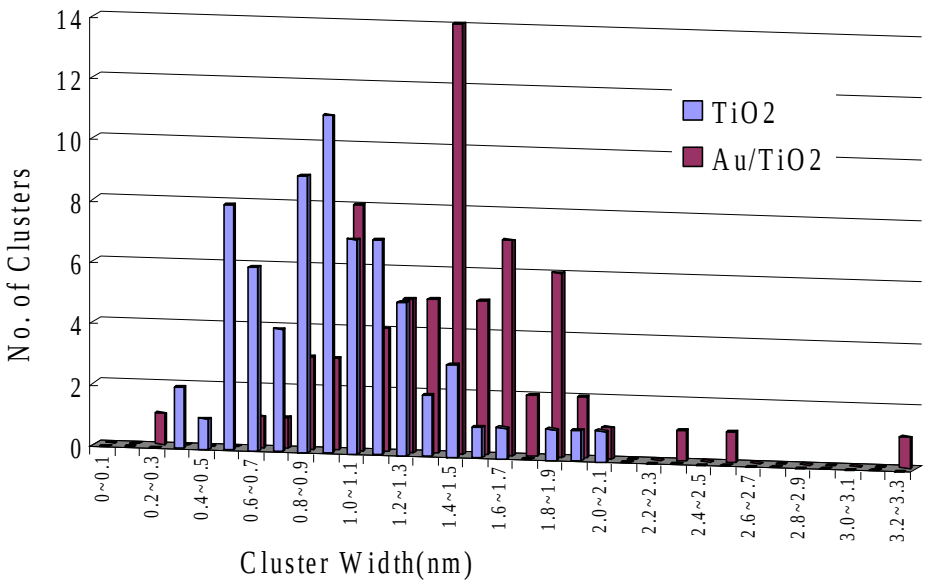

FIG. 4.10. The size distribution of the clusters before and after 0.4% ML Au deposition.

at the end structures of line defects while 14% are at the side of line defects and 17% are seen on the terraces. It indicates that the initial nucleation of Au takes place preferentially at the TiO_2 nanocluster defects. Also among the 80 clusters examined, 40% of the clusters increase in width (along both [001] and $[1\bar{1}0]$ direction) and in height ([110]) while 20% increase merely in width (Table 4.2). The size distribution of the clusters before and after Au deposition is plotted in Fig. 4.10. Fig. 4.11 shows a close-up view of three representative TiO_2 cluster defect sites before and after Au deposition: (a) at the end structure of a line defect, (b) on the line defect, and (c) on the (1×1) terrace. The number of adsorbed Au atoms on all 80 TiO_2 cluster defect sites has

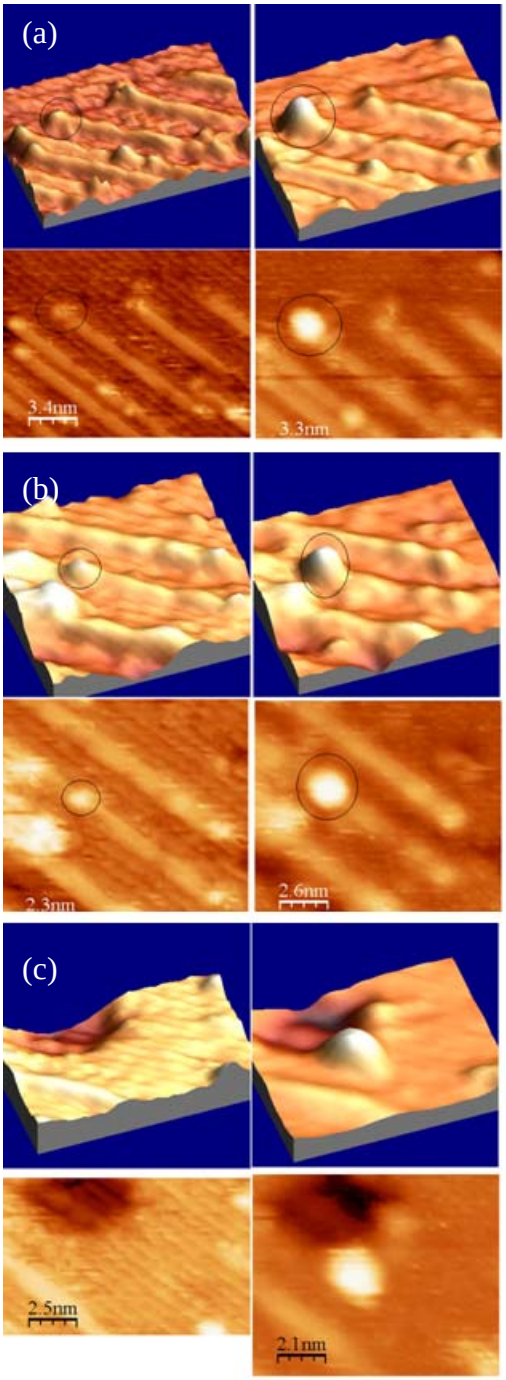

FIG. 4.11. STM images of three distinct TiO_2 clusters before and after Au deposition. (a), (b) and (c) show clusters locate at the end structure of a line defect, on the line defect and on the (1×1) terrace, respectively.

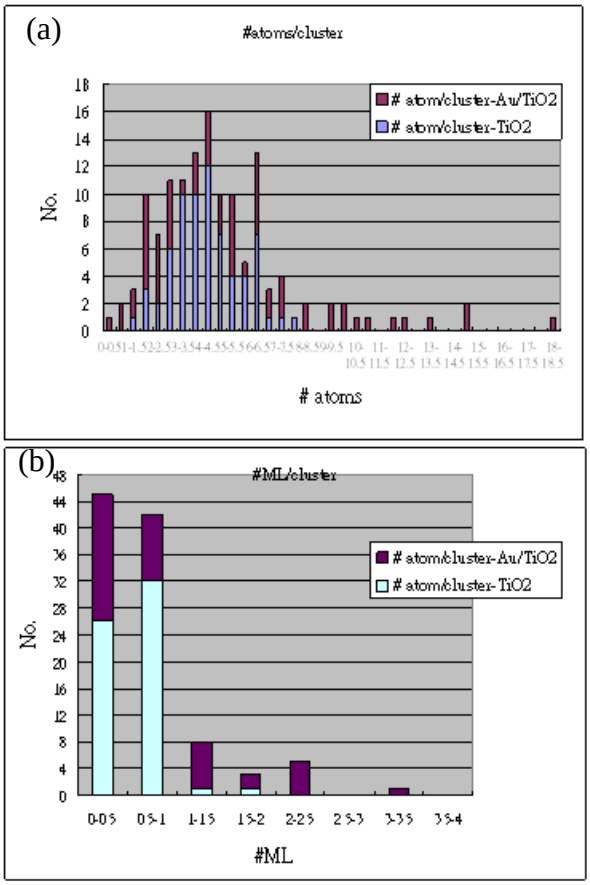

FIG. 4.12. Number of Au atoms that adsorbed on the TiO_2 cluster (a) and the change of cluster height reported in ML (b).

been calculated using the image analysis. Most of the defects have 2 to 8 Au atoms adsorbed, and most of the sites are thus covered with ≤ 1 ML of Au atoms (Fig. 4.12(b)).

The initial adsorption of Au and the subsequent nucleation at the TiO_2 cluster defect are investigated by comparing the energetics for various adsorption sites using DFT [55]. The adsorption energy for Au is calculated as the difference in the total energy before and after Au attachment: $E_A = E(Au_n/TiO_2) - [E(TiO_2) + n \times E(Au_1)]$ for the n^{th} Au atom (n = 1 through 4) attached to the TiO_2 defects on the surface. The theoretical calculations indicate that the most energetically stable adsorption site for Au atom is found between 1-fold O atom of the defect and the bridging O atom at the surface (Fig. 4.13(a)). The adsorption energy for Au atom at the cluster defect is calculated as -2.74 eV. This value

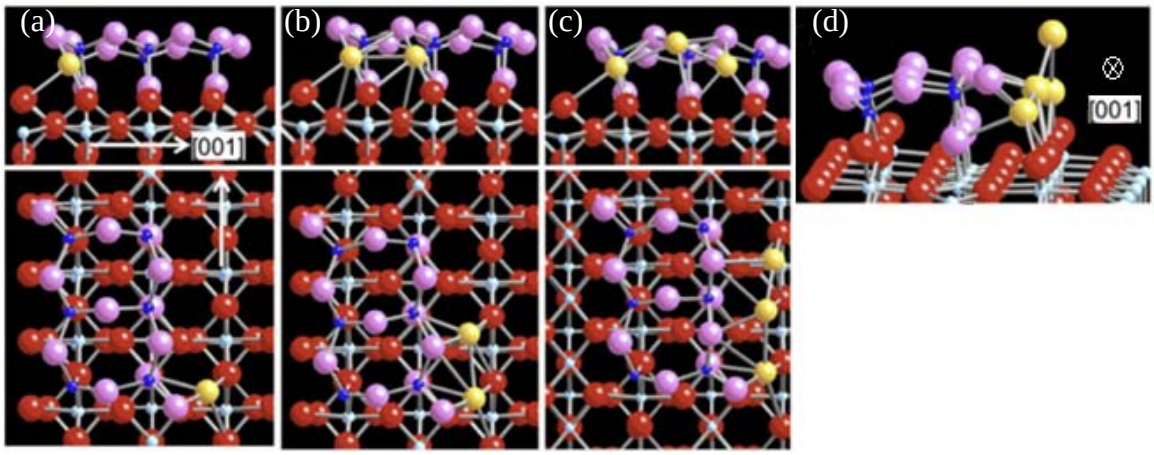

FIG. 4.13 (a), (b), (c) and (d) DFT-relaxed structures of Au_n adsorbed on the $(TiO_2)_6$ on TiO_2(110) for n = 1, 2, 3, 4, respectively. (Au: yellow) [18].

is substantially larger than the reported corresponding energy of -2.38 eV for Au bonded to an O-rich surface [56]. It is also much larger than the energies of -1.36 eV and -1.31 eV for Au adsorption on TiO_2(110) containing sub-surface defects of Ti interstitial and O vacancy, respectively [57]. In order to gain an insight into the exceptional stability of Au on the cluster defect, the local electronic structure is studied. Fig. 4.14 presents the density of states (DOS) of the 1c- and 2c-O atoms of the defect and the surface 2c-O for the TiO_2 system without Au. As can be seen from this figure, the two types of defective

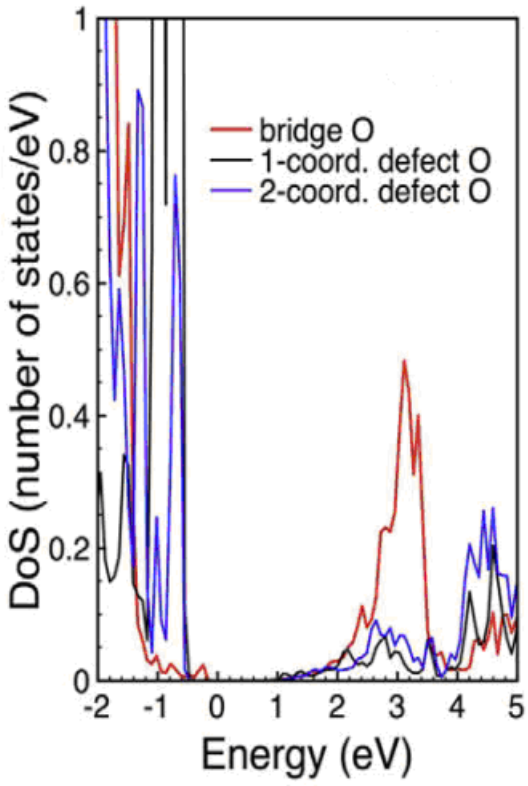

FIG. 4.14 The projected DOS plotted for the 1-c (black line), the 2-c (blue) O of the defect, and surface bridging O (red) of TiO_2(110) [18].

O DOS above the Fermi level overlap the surface bridging oxygen indicating that all O sites have available states for adsorbing Au. Both sites have a limited number of states near the Fermi level with the surface 2c-O having a slightly larger number in the 2.5 – 3.5 eV range and the defect O having a slightly larger number in the 4 – 5 eV range. The bond geometry for single Au adsorption has two nearest neighbor O atoms as in Au bonded to O-rich TiO_2(110): the defect 1c- and surface 2c-O atoms. Thus, the stability of the Au comes from the lowering of the energy due to the hybridization between the two types of O atoms as well as the reduction of the Coulomb repulsion by having the Au adsorption site between the defect and surface O atoms.

The adsorption site for the second Au atom is found behind the first Au along [001] (Fig. 4.13(b)). It can be also understood by its local bond geometry and the electronic structure. The second Au has two nearest O neighbors, the 2c-O of the defect and the surface 2c-O at 2.08 and 2.15 Å, respectively. The DOS for the 2c-O of the defect (Fig. 4.14) has analogous features as the 1c-O of the defect. Both O atoms of the defect and of the surface provide the unoccupied states for the second Au with a similar mechanism of lowering energy as in the initial adsorption. However, the distance between two Au atoms is 2.94 Å, compared to the bulk value of 2.88 Å, suggesting the increase in Coulomb repulsion associated with the first Au.

The addition of the third Au atom at the cluster introduces significant modifications in the atomic positions and bond lengths among Au and O (Fig. 4.13(c)). Most notably, the second Au atom is pushed up so that the Au_3 chain along [001] buckles up. The two nearest neighbors are the surface 2c-O at 2.25 Å and the 2c-O of the defect at 2.66 Å. On the other hand, the bond distance between the second and the third Au atoms is only 2.58 Å, almost 11.6% contraction from the bulk value. The cluster continues to grow with the fourth Au atom found between the second and the third Au atoms with the bond distances of 2.64 and 2.60 Å, respectively (Fig. 4.13 (d)). However, the distance from the last Au atom to the nearest O atom is 3.58 Å, indicating that the stabilization mostly comes from the Au–Au bond.

Low temperature catalytic oxidation of carbon monoxide by gold nanoparticles supported on a TiO_2 single crystal has been reported [23, 58]. The extraordinarily high activity of the nanosize gold catalyst supported on TiO_2 was unusual, as gold has long been known as being catalytically far less active than other transition metals. This catalytic behavior was later found to be dependent particularly on the size of Au clusters. The maximum activity occurred with Au clusters size of 3.5 nm [58, 59]. Also it is suggested that the anchoring sites [60] and the interface structure [61] affect the distinctive catalytic properties. The Au atoms attached to the TiO_2 defect examined in

this study display the key features expected from catalytically active Au nanoparticles. First, the Au cluster remains strongly bonded to the TiO_2 defect throughout the growth. The strong bonding is made possible by the unique geometry: being wedged between the dangling O atoms at the side of the TiO_2 cluster and the surface bridging O rows. The adsorption sites provided by the O atoms also result in the ‘‘wetting” of the Au cluster along [001]. Second, the DFT calculation (Fig. 4.15) reveals the electron deficiency around Au atoms. Specifically, the first Au atom bonded to the 1c-O loses about 0.2 e^-, and the charge is redistributed to nearby oxygen atoms. The electron reduction at Au and the surplus at O are localized along the bond axis as in Au bonded to O adatom on TiO_2(110) [56]. Recent studies have also indicated that the cationic Au species are the

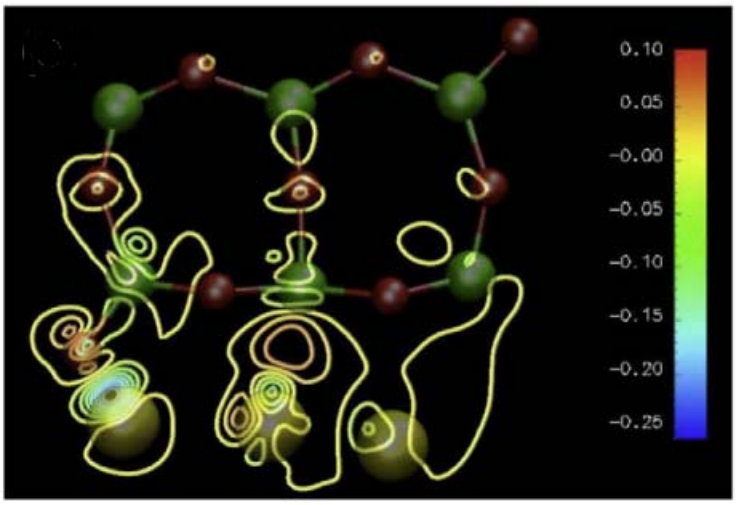

FIG. 4.15 The charge density difference plots for the Au 3 cluster, revealing electron depletion (blue) and surplus (red) with the increment shown in the color bar ($e^-/Å^3$) [18].

catalytically active form [62-65]. Third, in low temperature CO oxidation, CO has been envisioned to adsorb on Au particles at the metal-support interface [66]. The DFT calculation shows that CO indeed adsorbs on the top of the Au cluster wetted on the TiO_2 cluster defect with the adsorption energy of -1.11 eV . This value is considerably larger than the energy of -0.72 eV reported for CO adsorbed on Au_{34} cluster on defect-free MgO [67]. The stronger CO adsorption to Au in this study is attributed in part to the cationic nature of the Au cluster [68].

Finally our model suggests a succinct explanation for two seemingly contradictory requirements for active Au catalysts: slightly reduced oxide support, yet the presence of cationic Au species. In reduced TiO_2, interstitial Ti atoms are drawn to the surface upon exposure to oxygen and react to form various oxide species including fully stoichiometric TiO_2 [52-54]. It is the stoichiometric TiO_2 defect that gives rise to the formation of $Au^{\delta+}$ species through Au-O bonds. In this perspective, the advantage of reducible oxides over non-reducible ones lies in the ability to produce the surface defects of reduced coordination but increased surface area.

CHAPTER FIVE

Result and Discussion II

5.1 TiO_2(001)

5.1.1 Review of the Existing Models for Reconstructed TiO_2(001)

As noted in Chap. 1, TiO_2(001) has the highest surface energy among the low index surface planes, and it is known to exhibit a number of different facet formations depending upon treatment methods and perhaps history as well. Major studies reported on temperature-dependent faceting and the proposed structural models are reviewed in this section so that comparative discussions between the existing models and our results can be presented in the subsequent sections.

The earliest investigations of TiO_2(001) utilized LEED as the main structural probe. Using the LEED patterns from the annealed TiO_2(001), Chung *et al.* in the late 1970s reported that the surface was faceted [69]. A couple of years later, Tait and Kasowski. [70] found two types of faceted surfaces on TiO_2(001). The type I structure was formed after annealing the ion-bombarded surface at 475 °C whereas the type II structure was formed after annealing the sample above 950 °C. Firment later identified the type I and II reconstructed surfaces as {011} and {114} faceted surfaces, respectively [71]. He assigned the specific planes after comparing the observed beam positions with the calculated ones using the LEED kinematic approach [72]. Because a surface could be more damaged through sputtering than being fixed, Mason *et al.* attempted to obtain a

pristine surface without sputtering and annealing, cleaving a natural single crystal to expose the (001) surface [38]. Although two possible structures based on the minimum values of the R-factor to the I-V spectra were proposed, they did not receive much attention from the surface community due to low intensity contrasts and limited energy ranges of the LEED data gathered in the study.

After the LEED studies, STM has been widely used to investigate TiO_2(001) in the past 15 years. Nörenberg *et al.* [73] employed STM, atomic force microscopy (AFM), and optical microscopy to study the surface after annealing at high temperatures between 1200 and 1600 °C. They reported a two-domain ($7\sqrt{2} \times \sqrt{2}$)R45° surface reconstruction with ridges. It was further suggested that the ridges or the lines caused by slip processes were formed to relieve stress after excessive annealing.

In 2001 Fukui *et al.* [74] reported atomically resolved images of TiO_2(001) with STM. A hill-like structure was observed on the surface after annealing at 900 K without a well-ordered LEED pattern. At annealing temperatures above 1160 K, the surface was covered with disordered protrusions. After annealing the surface at 1050 K, a bleacher-like structure was observed (Fig. 5.1). In the bleacher-like structure, the

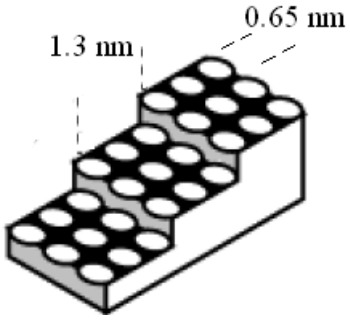

FIG. 5.1. The schematic drawing of a latticework structure on TiO_2(001) and the relative position of the bright spots [75].

row-like narrow terraces formed, running along the $[1\bar{1}0]$ and the $[\bar{1}10]$ directions. On each narrow terrace, three bright spots, lined perpendicular to the row axis, were imaged with a separation of 0.3 nm. Along the row, a regular interval of 0.65 nm was observed.

The distance between the parallel rows was 1.30 nm, hence the bleacher-like structure had the unit cell of 1.30×0.65 nm^2. The height of each step was 0.3 nm while the height between the crossed rows was 0.15 nm. Consequently, the slope of the bleacher-like row corresponded to the (114) plane. The authors tentatively proposed the {114}-microfaceted model, which consisted of a bulk-terminated (001) narrow terrace separated with steps of (111) orientation. In this model, three 4-fold coordinated Ti atoms on the terrace and two 5-fold coordinated Ti atoms on the zigzag steps were exposed. However, this model was not consistent with the experimentally observed periodicity of 0.65 nm along the step.

A couple of years later, Tero *et al.* [75] of the same group analyzed the new molecular adsorption experiment, and assigned the center spot and side spot lined perpendicular to the row axis as 4-fold and 5-fold coordinated Ti atoms, respectively. In addition, they proposed the added-row model built on the {114}-microfaceted model of the lattice-work structure (was called bleacher-like structure in the previous article). This model aimed to resolve the inconsistency in the {114}-microfaceted model with the experimental data and to reduce as many unsaturated coordination sites of Ti atoms as possible in the previous model. So, in the new model, a suboxide row was added on each narrow terrace of the {114}-microfaceted structure, adopting the concept of a Ti_2O_3 'added row on TiO_2(110) [16]. More specifically, a row with stoichiometry Ti_7O_{12} was

added to the terrace of the top and a Ti_7O_{11} row was added to the terrace of the lower step. The added row had four interstitial Ti^{3+} atoms and three exposed Ti^{4+} atoms within a unit cell. Also, the atoms in the added-row model were at the preferable bulk-extended positions except for the interstitial Ti atoms. As a result, the new unit cell of the lattice-work structure had one 4-fold coordinated Ti atom and three 5-fold coordinated Ti atoms.

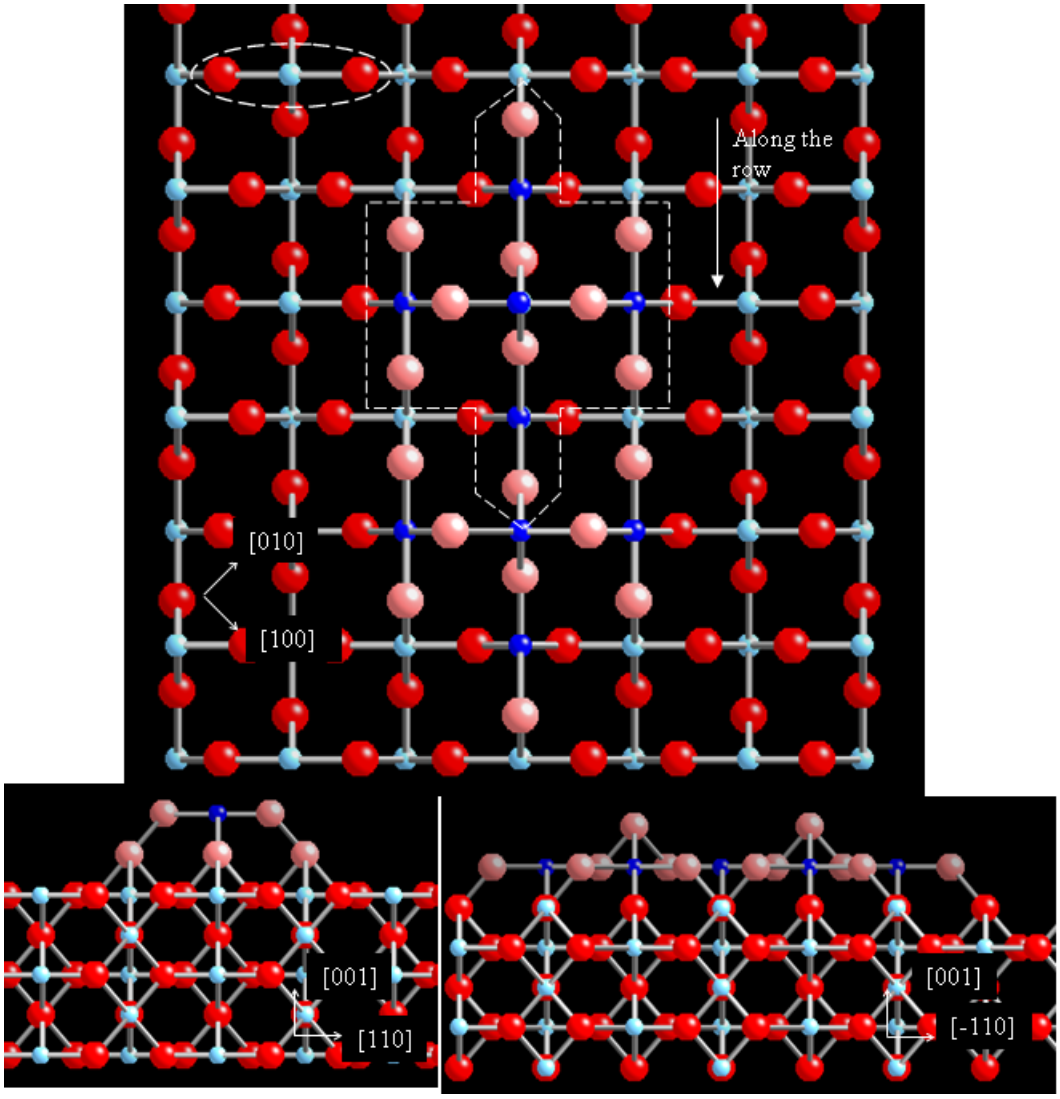

FIG. 5.2. {111} microfaceted model for TiO_2(001) reconstructed surface (reproduced from [76]). The TiO_2 unit highlighted in an ellipse (top) is the chosen form and the polymerly circled unit is a pentamer on an isolated row structure.

The added-row model was later tested by Kubo *et al.* [76]. The density functional theory (DFT) calculations suggested that the model was unstable due to a huge stress caused by the interstitial Ti atoms and outermost oxygen atoms being pushed into vacuum. The authors further systematically studied the (001) surfaces prepared by various experimental conditions. Combining both experimental and computational results, they proposed the {111}-microfacted model (Fig. 5.2). In the {111}-microfacted model, TiO_2 units were viewed as building blocks extracted from the unreconstructed surface. With five units of TiO_2, a dot-like structure (a pentamer) was constructed. Repeating the dot-like structure along the [110] or the $[1\bar{1}0]$ directions, a single row structure was generated. However, in order to form the {114} faceted row structure, an extra TiO unit between the rows needed to be removed and hence exposed the sub-plane of {111}.

Using the same line of thought for the stoichiometric surface, Ariga *et al.* [77] also proposed a revised model of the added-row model (the third version of the {114}-microfaceted model). They provided XPS and near-edge X-ray absorption fine structure (NEXAFS) spectra indicating that the Ar^+ sputtered surface after annealing remained stoichiometric with the absence of the Ti^{3+} species. In this model, four interstitial Ti atoms and two oxygen atoms were removed comparing with the previous model by Tero *et al.* [75]. In other words, a row with stoichiometry Ti_3O_{10} was added to the top terrace and a Ti_3O_9 row was added to the terrace of the lower step. Although the revised model was claimed as "stoichiometric," the added rows were actually oxygen-rich.

Most recently, Busiakiewicz *et al.* [78] reported a well-ordered surface consisting of the lattice-work structure after sputtering and annealing at 1073 K. After further heating at an elevated temperature 1173 K for an hour, the separation distance between the rows of the same height increased to 2.6 - 2.8 nm, yet the interval along the top row remained unchanged. The surface was reported to form new domains of size 30 nm^2 after the elevated temperature annealing, but no model was suggested in the article.

In summary, the {114} structure was suggested as a typical reconstructed surface on TiO_2(001) after annealing the surface at or above 900 °C. However, the STM images with atomic scale resolution revealed that the surface was far more complicated. There were no macroscopically ordered {114} planes, at least not seen on surface. Instead, the reconstructed surface had bleacher-like structures, exhibiting numerous tiny {114} facets or microfacets of several tens of angstroms. It was also reported that the bleacher-like structures or rows could increase in length and separation after annealing at an elevated temperature [73, 78] although annealing at an elevated temperature was earlier thought to disorder the surface [74, 75].

Despite significant variations in modeling the reconstructed TiO_2(001), there appears to be a common denominator: row structure. Regarding its atomic structure, one important question one has to ask is whether its composition is sub-stoichiometric (i.e. strand defects on TiO_2(110)) or full stoichiometric in nature (i.e. nanocluster defects on TiO_2(110)). Experimentally to a certain extent, one could control and limit oxygen deficiency and, thus, excess Ti atoms on the surface, employing low doses of Ar^+ ion sputtering followed by annealing at a moderate temperature. Such a minimally sputtered and annealed surface would be more likely to remain stoichiometric overall and

provide valuable insight into the nature and atomic structure of the surface reconstruction. However, unlike the high temperature annealed surface, the faceted surface produced after the low temperature annealing was rarely studied due to its rugged surface morphology. In this chapter, LEED and STM studies of a reconstructed TiO_2(001) prepared with a moderate sputtering followed by annealing temperatures (up to 600 and 700 °C) are presented and discussed.

5.1.2 LEED

The LEED pattern of TiO_2(001) taken at room temperature shows four sharp beams in the square symmetry (Fig. 5.3). As the symmetry is the same as that of a bulk terminated TiO_2(001) surface (the inset of Fig. 5.3), they are tentatively labeled as (10) and (01) spots. Using Ag(111) and TiO_2(110) as the references for the calibration, the lattice constant for the square unit cell is calculated as 4.5 ± 0.1 Å. The calculated value is in excellent agreement with the bulk-terminated lattice constant of 4.594 ± 0.003 Å [7, 8] along the [100] and the [010] directions. The corresponding LEED spots are thus identified as the first order diffraction spots from a bulk-like surface. The LEED pattern also reveals fractional-order spots, which are indexed by numbers, such as 1/2 1/2 and -1/4 1/4. The fractional-order spots look more diffused and faint compared with the integral-order spots. They represent a new unit cell with the size of 13.0 ± 0.3 Å× 6.5 ± 0.3 Å measured along the [110] and the $[1\,\bar{1}0]$ directions. This larger and rotated unit cell represents the intrinsic reconstruction of the clean surface: $(2\sqrt{2}\times\sqrt{2})$R45° superlattice (or overlayer). Two domains are observed to orient perpendicular to one another. One contains (1/2 1/2) and (-1/4 1/4), and the other is formed by (1/2 -1/2) and

(1/4 1/4). This two-domain structure indicates that the new reconstructed surface has a long range of two kinds of distinct patches whose structures are identical. In addition, streaks between the spots are observed along the [110] and the $[1\,\bar{1}0]$ directions. They are formed by the irregular fashion of reconstruction [27].

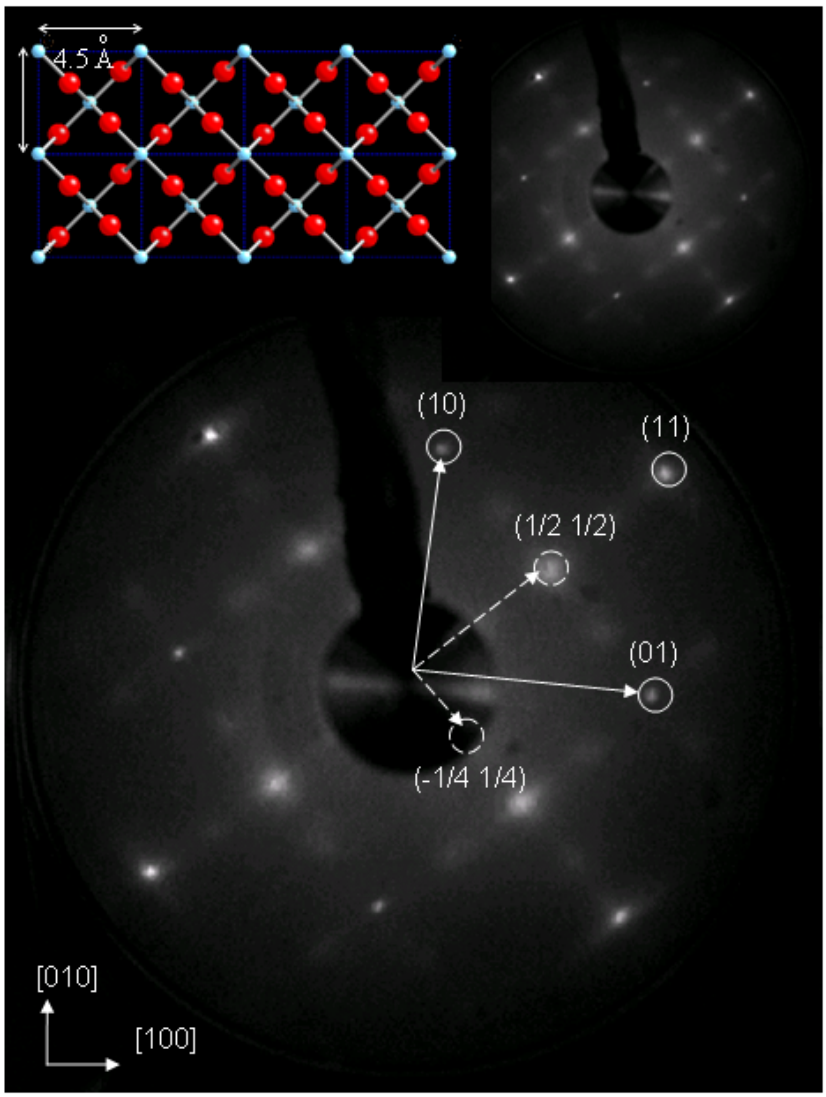

FIG. 5.3. LEED pattern of TiO_2(001) taken at 41 eV.

Splitting of the integral-order and the fractional-order spots accompanying streaks are also observed. For example, a single spot of the (11) beam is initially observed at

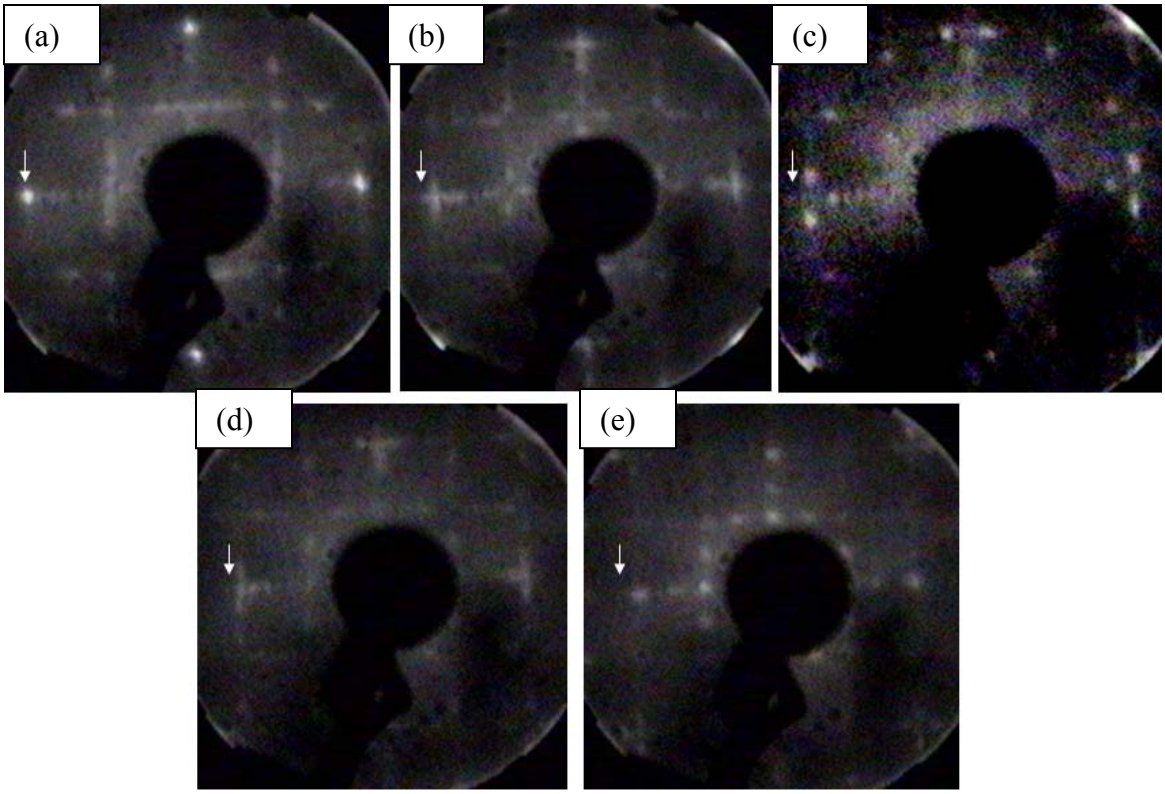

FIG. 5.4. LEED images of TiO_2(001) taken at 48 eV (a), 53 eV (b), 60 eV (c), 65 eV (d) and 70 eV (e). The arrows are pointing at the (11) beam.

the incident energy 48 eV (Fig. 5.4 (a)). As the incident energy increases to 53 eV (Fig. 5.4 (b)), the single spot is replaced by a short streak. When the energy increases to 60 eV (Fig. 5.4(c)), double spots elongated along the [110] direction appear, which are called streaky double spots. The streaky double spots return back to a streak at 65 eV (Fig. 5.4(d)) and then to a single spot at 70 eV (Fig. 5.4(e)). As the electron energy increases,each (11) reflex continuously repeats transitions between a single spot, a streak and a streaky double spot.

Splitting of integral-order and fractional-order spots is a well-known indicator that the surface is stepped [27, 32, 79-86]. The stepped terrace width can be derived from the splitting angle of the double spots as described in Chap. 3. On top of this, the

presence of mixtures of patterns, i.e. streaky double spots mixing a streak with double spots, suggests the existence of other terraces of irregular width with parallel step edge orientation [32]. The step edge orientation is perpendicular to the splitting directions along [110] and $[1\bar{1}0]$ while the stepped terraces formed in two domains are parallel to the splitting directions. The spot splitting is observed on both TiO_2(001) surfaces with different annealing temperatures of up to 600 °C and at least 700 °C used. For both surfaces, the energy ranges of the spot splitting overlap one another showing that they have the similar step height of the reconstruction (Sec. 3.2).

Unlike the integral-order single spots, which simply converge toward the specular beam (or 00 beam blocked from view by the electron gun) with increasing energy, the split spots move in a more complicated way as previously reported [71]. When the spot splitting occurs, the center spot (the integral-order spot) is replaced by closely spaced spots, i.e. split spots. These split spots first separate outward from the replaced center spot and then collapse back to the center spot as the electron energy increases. During this period, the split spots also converge toward the specular beam of the stepped surface. This diverging and then converging behavior indicates that the surface has both ascending and descending steps [81], which can be understood distinctly with the Ewald construction depicted in Fig. 5.5.

Fig. 5.5, shows one set of terrace rod arrays drawn in black and two sets of ascending and descending rod arrays of the stepped surface drawn in green and light green. The specular beams are marked as (00). The shown energy starts from 10 eV and increases stepwise by 5 eV. As the number of stepped rods increases, the energy range of visible splitting beams (shown as the dots in Fig. 5.5) increases as well. The

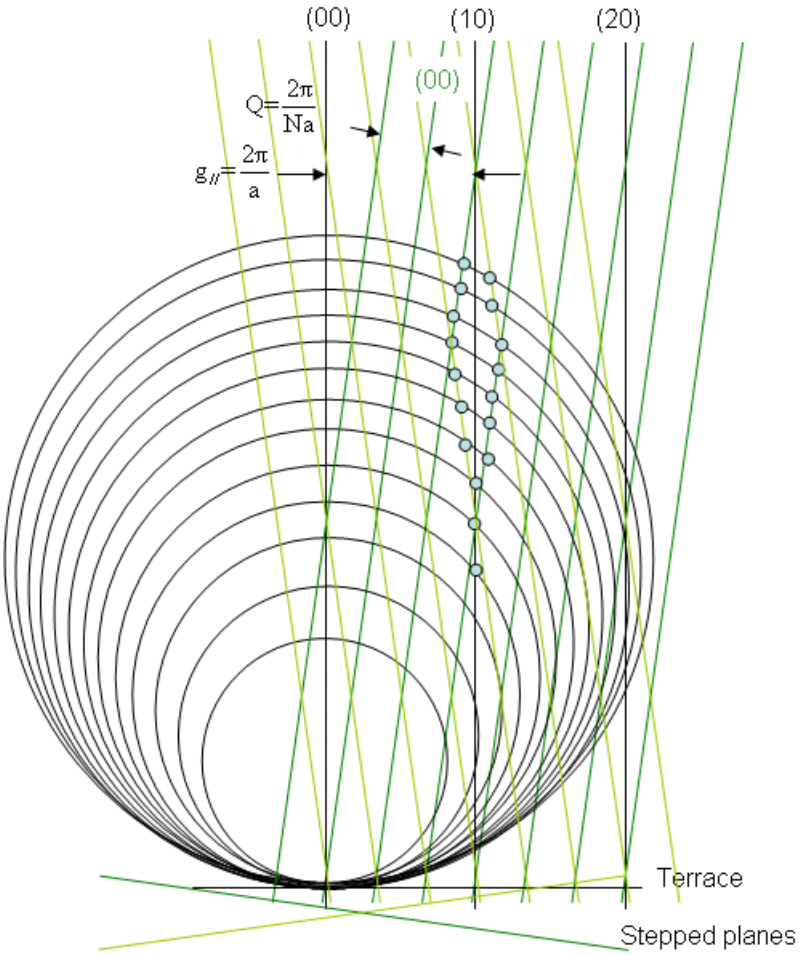

FIG. 5.5. Ewald construction depicting both ascending and descending steps and the consequent behavior of spot splitting. The corresponding energies of the Ewald spheres drawn in the figure have an interval of 5 eV starting from 10 eV.

consequent diverging and then converging behavior is then observed. At the same time, the splitting spots converge toward the stepped specular beam.

For a quantitative analysis, the motions of splitting spots are traced as energy increases in Fig. 5.6. Fig. 5.6(a) shows the trajectories of the (11) beams with increasing electron energies starting from 53 eV. When the splitting occurs at 57 eV, each (11) beam is replaced by two pairs of split spots (red spots in Fig. 5.6(a)). The appearance of the two pairs of split spots is due to the two-domain configuration. After

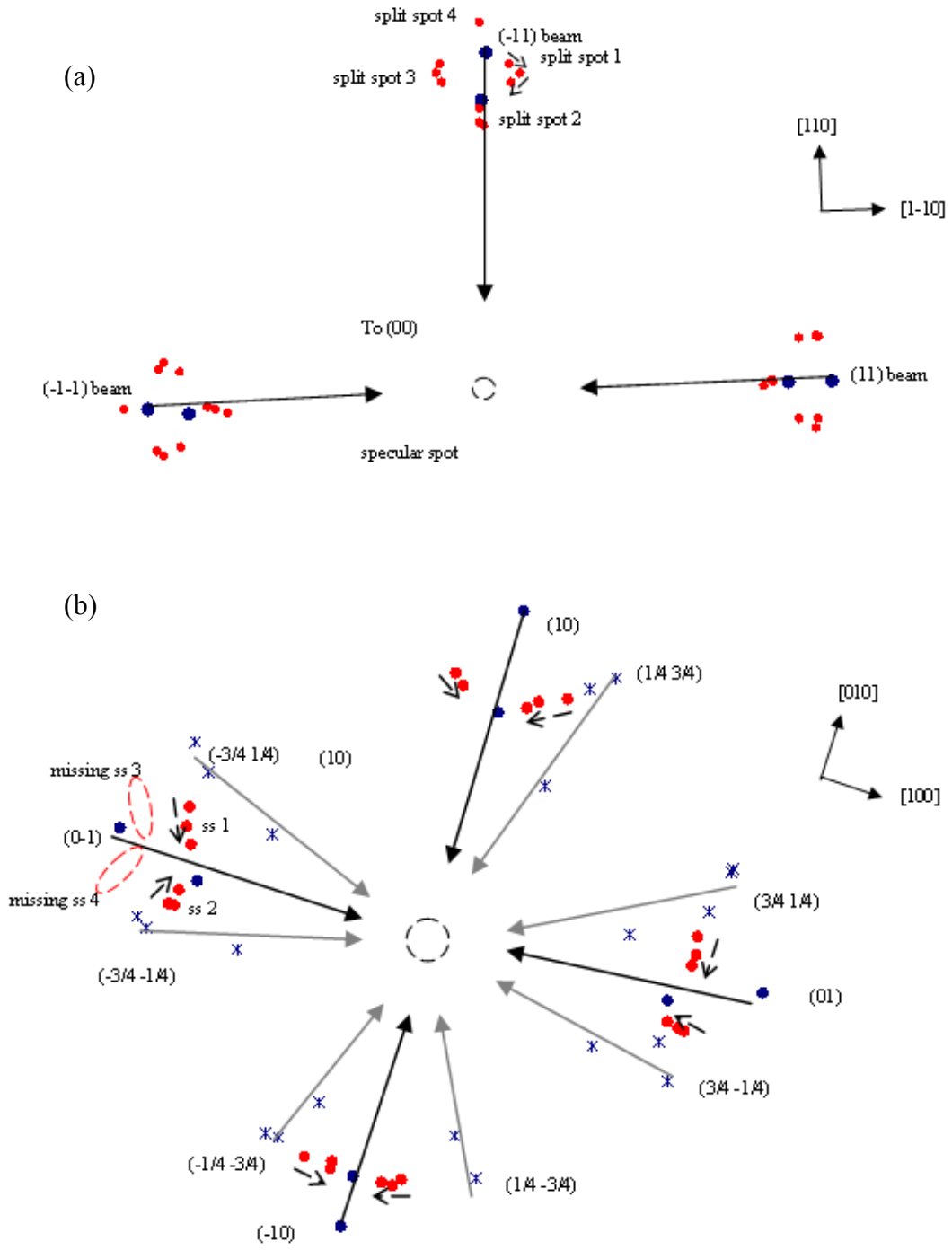

FIG. 5.6. Beam trajectories of TiO_2(001) with increasing energy. (a) The blue and red circles are the (11) beams and their splitting spots, respectively. The solid lines and the dashed line are pointing to the moving directions of (11) beams and their splitting spots, respectively. (b) The blue circles, red circles and blue stars are the (10) beams, their splitting spots (ss) and the (1/4 3/4) beams, respectively. The black solid lines, dashed lines and the grey solid lines are pointing to the moving directions of (10) beams, their splitting spots (ss), and the (1/4 3/4) beams respectively.

the initial split, the split spots start to move away perpendicularly from the line of trajectories (along the [110] and the $[1\,\bar{1}0]$ directions) until 60 eV, at which energy the pair are separated the farthest from each other. Then, they move back towards the central trajectory lines into a single spot after 64 eV. Once the split spots collapse into a single spot, the replaced (11) beams reappear and continue the motion along the central trajectory lines. During the splitting, only three of the four split spots are usually seen in most of the LEED images, possibly due to the weaker intensity of the fourth split spot.

A similar behavior of the splitting spot is also found in the (10) beams. With increasing electron energies, the motions of the (10) beams and their nearby fractional-order beams (1/4 3/4) are shown in Fig. 5.6(b) by the black and grey solid lines, respectively. The trajectories of the (10) and the (1/4 3/4) beams start from 35 eV and 19 eV, respectively. The split spots of the (10) beams appear from 28 to 35 eV. Each split spot moves toward the center (10) beam along the [110] and the $[1\,\bar{1}0]$ directions while the (10) beams (moving along the [010] or the [100] directions), and the (1/4 3/4) beams move toward the specular spot. The initial part of the motions for the split spots (moving outward from the center beams) are barely observed on the screen because of their weak intensities at very low incident energy as similarly seen in the (11) spot.

During the energies from 28 to 35 eV, only two split spots of the (10) beam are observed moving along the $[\bar{1}\,\bar{1}0]$ and the $[\bar{1}10]$ directions. The other two moving along the [110] and the $[\bar{1}10]$ directions are missing (Fig. 5.8(b), left). Meanwhile, only the streaks extending toward the same moving directions of the split spots are observed. This behavior is also observed at the next splitting of the spots at the energies above 54 eV. Similar inequivalent intensities of the split spots were also observed in

other publications [85, 86]. It is suggested that the inequivalent intensities of the split spots are caused by off-normal incidence due to the slightly tilted sample orientation.

The spot splitting is observed at two separated intervals of characteristic energy. One occurs from the energy range of 25 to 35 eV and the other occurs between 53 and 65 eV. According to the Ewald construction (Fig. 3.2) or Eq. 3.8, the first splitting was

TABLE 5.1. Calculated facet plans and the parameters used for the higher temperature (700 °C) annealing surface (top) and the lower temperature (600 °C) annealing surface (bottom).

Annealing Temperature (°C)	At least 700		Up to 600	
$E_\nu(h,k)$	$E_2(1,0)$	$E_3(1,1)$	$E_2(1,0)$	$E_3(1,1)$
Energy (eV)	35	59	35	58
φ (degree)	29.8	22.7	25.8	25.2
$\delta\varphi$ (degree)	7.4	5.3	5.9	5.6
Terrace width Na (Å)	18.5	18.8	22.4	18.4
$g_{//}$ ($Å^{-1}$)	1.40	1.97	1.40	1.97
Step height d (Å)	2.2	2.6	2.2	2.6
Facet angle α (degree)	6.8	7.8	5.6	8.0

predicted to occur at around E_1 = 16 eV. However, this splitting was not observed because its position occurs outside the LEED screen. The splitting started at 25 eV and 53 eV are referred to the second ν = 2 and the third ν = 3 order splitting. Applying the equations in 3.1.1, information on step arrangements is shown in Table 5.1, including the parameters [87] used for calculating the facet angles. In this table, only the largest splitting angles $\delta\varphi$ are used. The terrace width Na calculated from the splitting angles is approximately 2 nm. The step height d from the characteristic energies is around 2.5 Å. Consequently, the calculated angle of the stepped surfaces with respect to the (001) surface is up to 9 degrees, which facets to the (116) plane. However, recall that the observation of the short streaks before the spot splitting, as well as the streaky double spots, suggests a range of angles between the stepped surfaces and the (001) surface due to various terrace widths. It is thus expected that the surface consists of more than one phase that may result from temperature gradients across the sample [71].

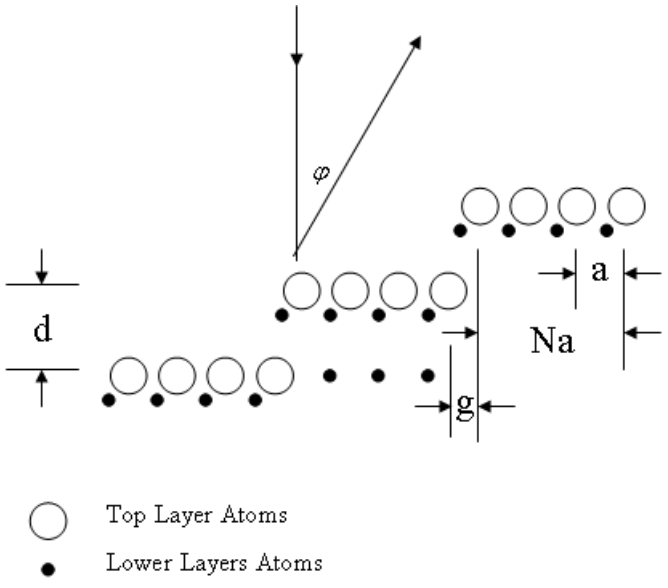

FIG. 5.7. Geometry of the kinematical approximation [89].

Based on the above kinematic experimental results and a simulation of the kinematic approximation [88, 89], more detailed information on the properties of the reconstructed surface can be obtained. According to the geometry in Fig. 5.7, the scattered intensity I at an angle is

$$I(\varphi) = const. \frac{\sin^2[\frac{1}{2}ka(N+1)\sin\varphi]}{\sin^2[\frac{1}{2}ka\sin\varphi]} \sum_{i=-\infty}^{+\infty} \delta[\frac{1}{2}ka(Na+g)\sin\varphi + \frac{1}{2}kd(1+\cos\varphi) - i\pi] \tag{5.1}$$

where k is the wave number of the electron beam, N + 1 is the number of atom rows on one terrace, a is the lattice spacing, d is the step height, and g is the parallel shift of the adjacent steps. Given N = 2, a = 6.4 Å, d = 3 Å, g = a, the split spots observed on the

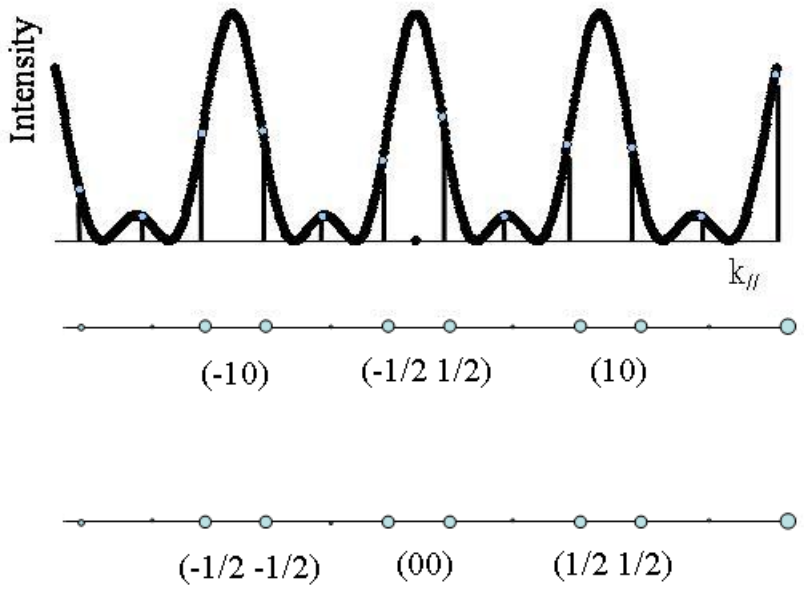

FIG. 5.8. Intensity profile from TiO_2(001) (top) and the resulting diffraction pattern (bottom).

reconstructed (001) surface are reproduced (Fig. 5.8). It is shown that at 53 eV, splitting occurs at the integral-order spot (00) and (10) as well as the fractional-order spot (1/2 1/2). The characteristic energy 53 eV is observed as the onset energy for the third order splitting. This voltage of coincidence of delta functions within the (1/2 1/2) reflection can be derived from the second term (the delta function term) in Eq. 5.1 when

$$\frac{1}{2}ka(Na+g)\sin\varphi+\frac{1}{2}kd(1+\cos\varphi)-i\pi=0 \tag{5.2}$$

With $\sin\varphi=\frac{2\pi}{ka}$ and $\lambda=\sqrt{\frac{150}{V}}$, Eq. 5.2 yields

$$V_{1/2\ 1/2}=\frac{150(i-\frac{g}{a})^2}{4d^2}\left[1+\frac{d^2}{a^2(i-\frac{g}{a})^2}\right]^2$$

which can be simplified as

$$V_{1/2\ 1/2}=\frac{150(i-\frac{g}{a})^2}{4d^2}\left[1+\frac{2d^2}{(ai-g)^2}\right]. \tag{5.3}$$

i is integral for a single spot case and half-integral for split spots. By using i = 2.5, the characteristic voltage is predicted to be 53 eV, which is in excellent agreement with the experimental observation. This single model approximation successfully illustrates the splitting on LEED beams with dependence on the voltage, step spacing and step height for a stepped surface.

Additional information (compared with the model in Sec. 3.2 and Table 5.1) of the horizontal shift of the adjacent terraces g is obtained. Fig. 5.9 displays step-terrace models of three different combinations of the terrace width and the horizontal shift between the adjacent terraces. Model A has the step structure with N = 3 and g = 0 that

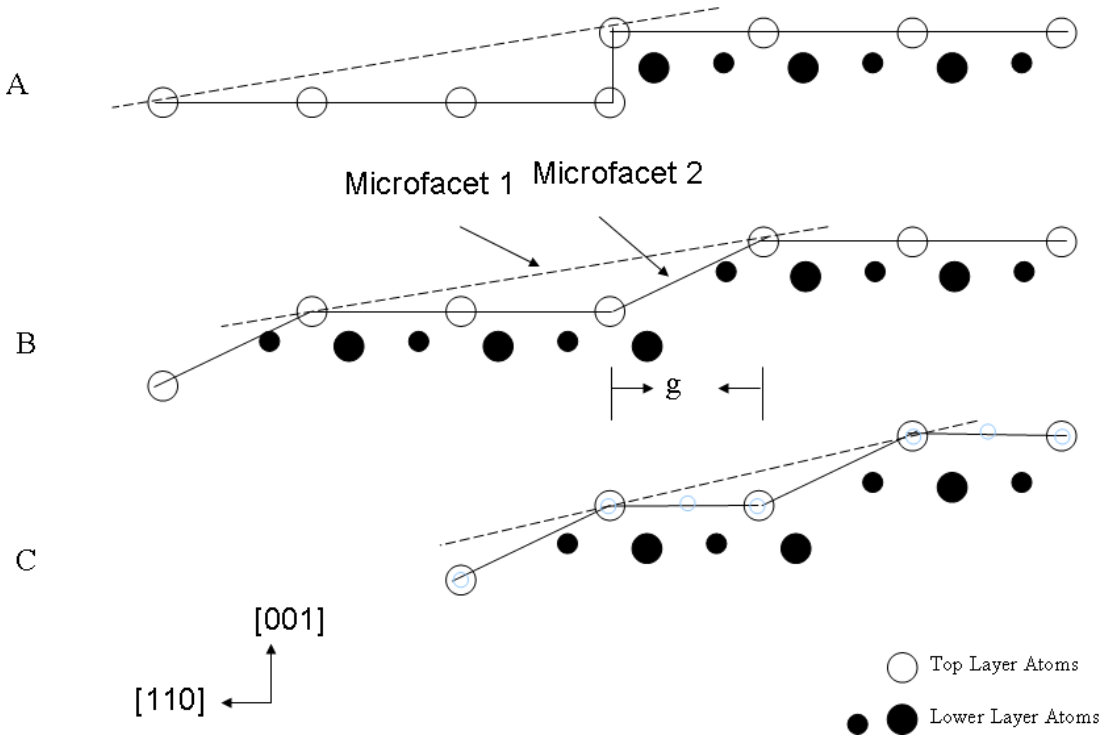

FIG. 5.9. Stepped surface structure obtained from the Ewald construction (Model A: N = 3, g = 0), the kinematical approximation (Model B: N = 2, g = a) and the STM observation [77] (Model C: N = 1, g = a).

can be deduced from the Ewald construction [Sec. 3.2 and Table 5.1]. After introducing a horizontal shift of g = a (and N = 2) between the adjacent terraces, model B is obtained from the method of kinematic approximation. Because both models A and B have the same step height of 3 Å and the same terrace periodicity of 3a or 19.2 Å, they have the same crystallographic plane of the steps. This plane is also referred as the type 1 microfacet whereas the type 2 microfacet is referred to the sub-plane exposed at the side of a terrace. Type 2 microfacet increases from (110) in model A to model B, in which more information is needed to determine the actual exposed sub-plane. Model C is a structure based upon the STM observation (N = 1, g = a) [77]. Model C is consistent with model B [74, 75, 77] on the step height and the interlayer distance. However, they differ on the terrace widths (12.8 Å for model B versus 6.5 Å for model C) and the

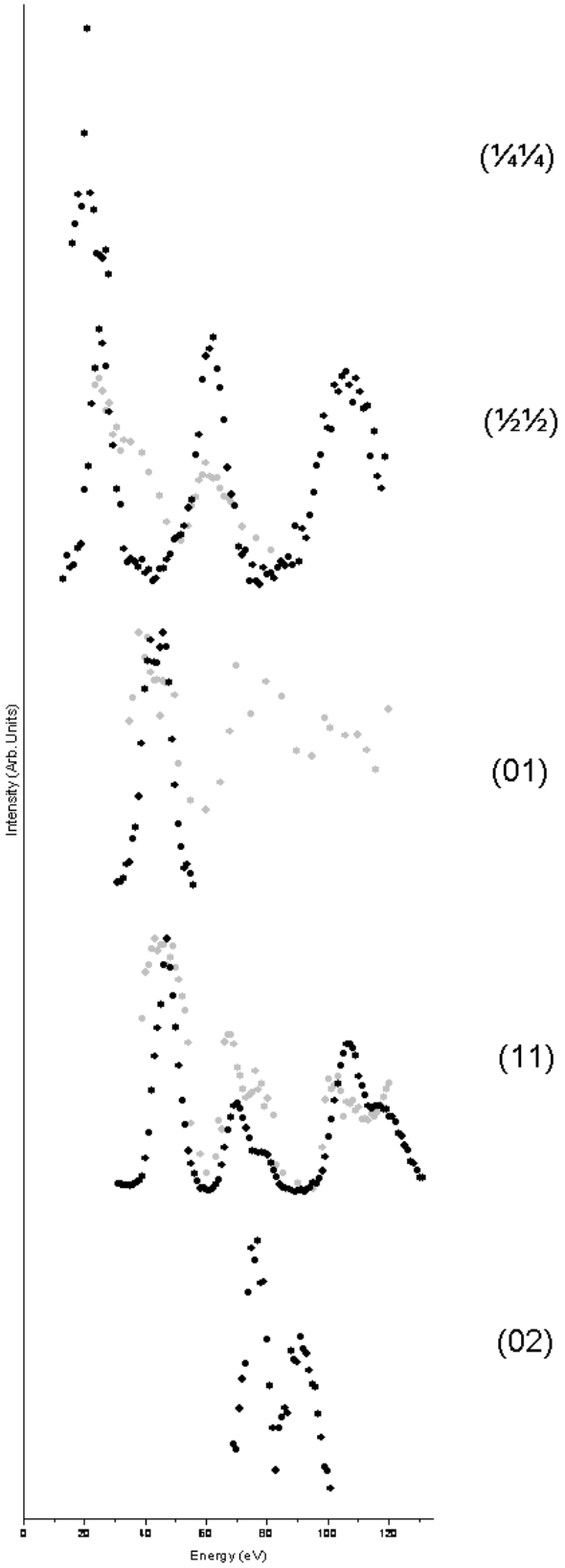

FIG. 5.10. LEED IV of TiO_2 (001) surfaces annealing at 600°C (black) and 700°C (grey).

corresponding type 1 microfacet planes ((116) for model B versus (114) for model C). The inconsistency is likely due to the fact that LEED probes the ensemble average of the terrace widths along and across the row (p. 99 and Fig. 5.11) while the STM results show those dimensions individually from direct imaging.

In addition to the kinematic analysis of the LEED data, the LEED I-V curves for selected diffraction spots are shown from 16 to 131 eV in Fig. 5.10. The black circles and the grey circles represent the I-V spectra extracted from the surfaces annealed at 600 °C and 700 °C, respectively. The peak positions are generally the same between the two curves. The difference between the relative peak height lies in the range of 40 to 50 eV of the (1/2 1/2) beam, which may indicate the different disordered structures in the overlayers.

As of now, relatively little structural information can be extracted using dynamic LEED calculations. As a stepped surface consists of closely packed atomic terraces, the plane-wave representation of the wavefield between the atomic layers becomes unsuitable. Consequently, the calculations using the conventional LEED theories diverge for the stepped surfaces [90]. Pinkave and Crampin [91] and Zhang *et al.* [92] adopted the method of spherical-wave representation to determine the structures of stepped surfaces. The theory has been tested and has permitted the calculation of converged diffraction spectra from simpler surfaces, such as metal surfaces. A further development of theoretical applications to a more complicated surface such as TiO_2(001) would be necessary for the structural determination of the surface using the LEED I-V data.

5.1.3 STM

The STM image from TiO_2(001) reveals row-like linear structures running along the [110] and the $[1\bar{1}0]$ directions (Fig. 5.11). The distribution of the lengths for most linear structures falls into 2, 3.5 and 5 nm. A few linear structures are as long as 8 nm. The length of the linear structures differs by a multiple of 1.5 nm. Zooming into the linear structure, elliptic bright spots lined with a separation of 0.65 nm are observed in Fig. 5.12. The distance between two nearest neighbor rows that run parallel to each other is measured. Among the 358 pairs of rows investigated, the nearest row distance varies from several tenths of a nanometer to a few nanometers. The majority of them fall in the range from 0.65 nm to 1.30 nm on average (Fig. 5.13). 41% of the nearest rows are adjacent to one another while the rest are separated from their neighbors as illustrated in the inset of Fig. 5.13. The periodicities along the row and between the rows form a unit

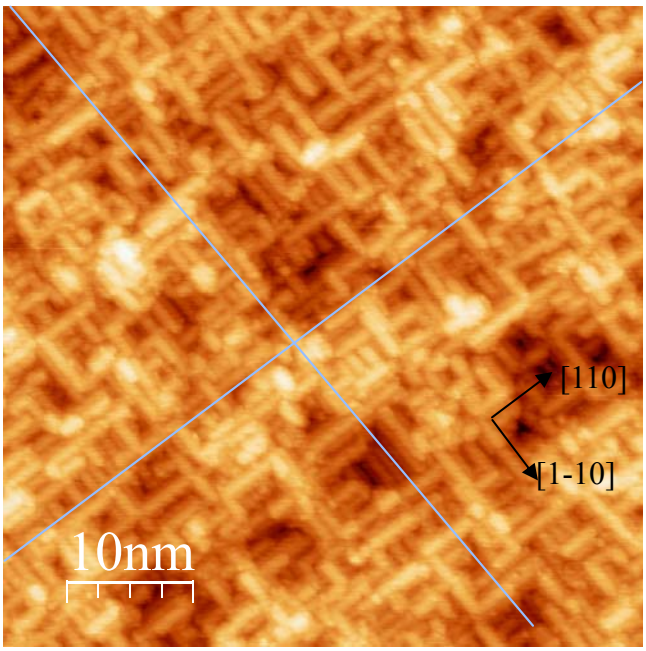

FIG. 5.11. STM image of TiO_2 (001) surface (4.8 V; 0.3 nA).

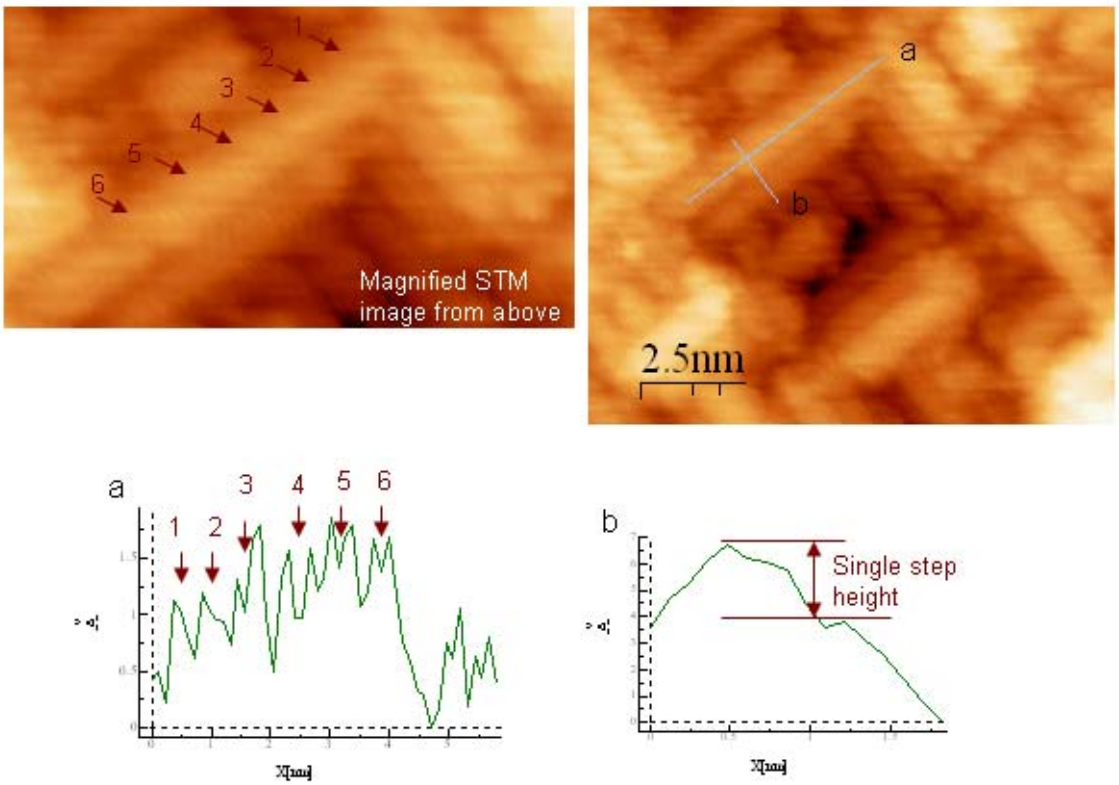

FIG. 5.12. STM images of a linear structure.

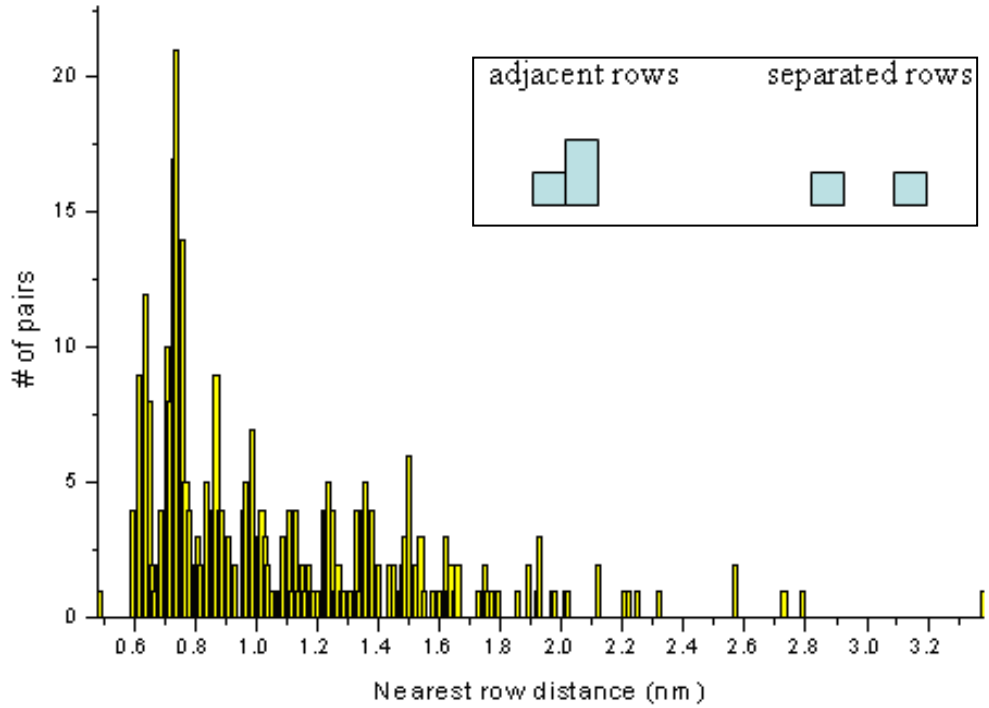

FIG. 5.13. The distribution of the nearest row distance

cell of 0.65 × 1.30 nm^2, which is consistent with the reconstructed unit cell predicted from the LEED study.

The height difference between the parallel rows is generally an integer multiple of a single-step height (0.30 nm). The height difference between the crossing rows is 0.15 nm, half of a single-step height. The histogram of the height difference can be found in Fig. 5.14 on a total of 70 crossing rows investigated. Figs. 5.15 show a STM image of

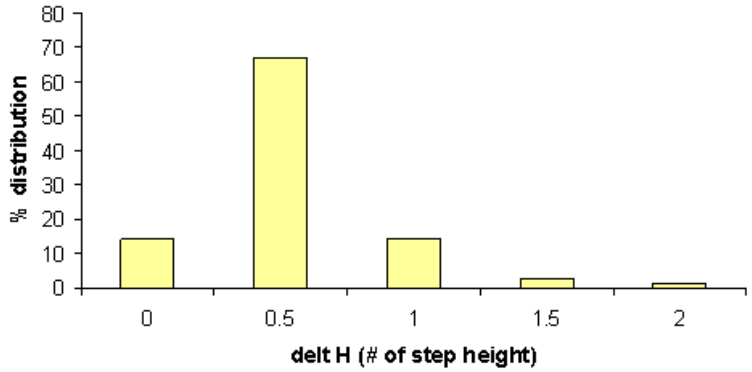

FIG. 5.14. The distribution of the height difference between the crossing rows.

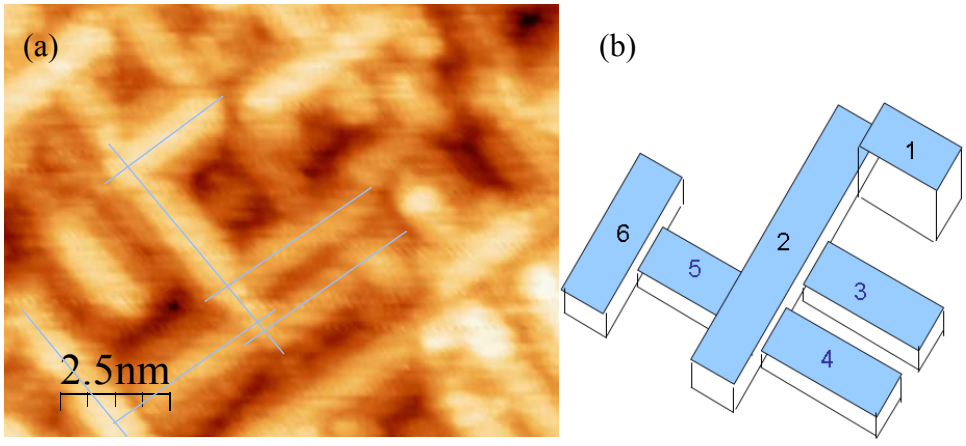

FIG. 5.15. STM image of the row-like linear structures and the schematic diagram of their relative height.

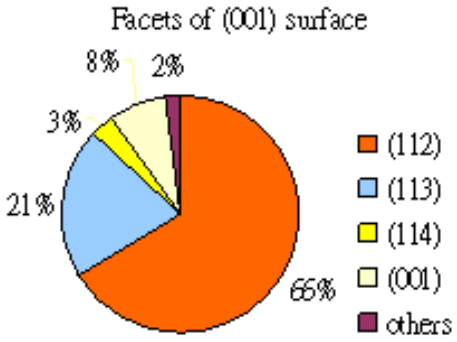

FIG. 5.16. Microfacets and their ratios of the adjacent rows on the TiO_2(001) surface.

the topography and the corresponding schematic diagram of the relative height relationship of rows: Row1 > Row 2 = Row 6 > Row 3 = Row 4 = Row 5. For the parallel rows in Fig. 5.15, their heights are either the same (i.e. Row 3 and 4) or differ by a single-step height (i.e. Row 1 and 3). For crossing rows, such as Row 2 and 3, their heights differ by a half-step height.

The slopes of the adjacent nearest rows are calculated to be inclined from the (001) surface by various angles between 0.4° and 39.0°, whose average is 22.6°. The extreme slopes (39.0° and 0.4°) correspond to the {111} and {001} microplanes. The distribution of the microplanes, shown in Fig. 5.16, are {112}, {113}, {114}, {001}and others (eg., {111}, {115}, etc.) with the ratio 65%, 21%, 3%, 8% and 3%, respectively. The inclination angles between the slopes of the separated nearest rows and the (001) surface are between 0° to 30°, with an average of 6.1°. 80% of the corresponding microplanes are equal to or flatter than {116}. In summary, the microplanes of the separated rows are flatter than the adjacent rows, which reveal that the separated rows are usually about the same height and the adjacent rows have different heights as steps.

The surface roughness can be calculated by using

$$r = \left\langle \left[h(x,y) - h \right]^2 \right\rangle^{1/2}, \tag{5.4}$$

where $h(x,y)$ is the surface height at a point (x,y) on the surface, h is the average height and $\langle\ \rangle$ denotes the spatial average over position (x,y) in a planar reference surface [93]. The roughness changes over the length scale of 60 nm along [110] and $[1\bar{1}0]$ are 0.24 nm and 0.36 nm (Fig. 5.17). This indicates that the relative roughness of the surface is about a single-step height, which is flat over the long range. This observation is consistent with earlier STM results [74, 75].

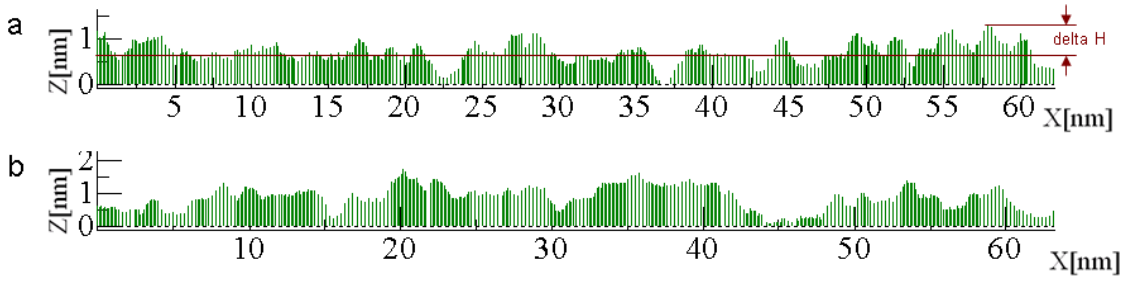

FIG. 5.17. Surface roughness along a and b shown in Fig. 5.11.

It is worth noting that the surface roughness calculated in this work indicates the flatness within a single step height variation over the long range. This is similar to the flatness reported for the high temperature (> 1027 °C) annealed surface. Also, the lattice-work structure and the {114} microfacets observed in this work appear to be the same atomic reconstructions reported by other groups [71, 74-78] despite employing the annealing temperature 300 – 400 °C below the reported values. Thus it is believed that similar surface flatness and the reconstructed structures are achieved in part due to the low Ar^+ ion current and energy employed in this study. With the Ar^+ sputtering current

and voltage that are about 10 times and 2 - 3 times smaller, respectively, our surface was likely less damaged and could be healed with a lower annealing temperature. On the other hand, the {011} faceted structure [71, 94] resulting from low temperature (627 °C) annealing was not seen in this work.

5.1.4 Proposed Model

Because of diverse surface reconstructions and their properties, it is very difficult to propose a single rule of thumb as to how a surface should reconstruct [95]. Nevertheless, there are some general principles one can keep in mind for a semiconductor surface reconstruction [96]. First, the saturation of the surface dangling bonds is necessary via rehybridization or via converting into non-bonding electronic states. Second, the surface structure observed is assumed to be the lowest energy structure achieved kinetically. Based on these underlying principles for reconstruction and experimental results, one can make several assumptions and guesses before proposing an initial model of TiO_2(001) reconstruction.

(1) The reconstructed surface is of full stoichiometric. The crystal color is associated with oxygen deficiency, and it can be a qualitative guideline for sample reduction [49, 50]. The sample color appeared as light blue after the treatments of sputtering and annealing described in Sec. 2.2, indicating that the sample was very slightly reduced. A nearly stoichiometric (1 × 1) TiO_2(110) surface resulted from similar conditions of sputtering and annealing yet more cycles further supports that TiO_2(001) is more likely stoichiometric than significantly reduced. In addition, the XPS investigations [77] on TiO_2(001) surfaces have shown that after annealing at 500 °C the

peaks of Ti^{4+} ($2p_{1/2}$) and Ti^{4+} ($2p_{3/2}$) are observed at 465.0 and 459.3 eV, respectively without a hint of Ti^{3+} and that the Ti^{3+} satellites are seen only after annealing at 1200 °C.

(2) Added Ti atoms are located at bulk-extended positions on TiO_2(001). On TiO_2(110), we have shown that the position of the Ti cation is closely related to the local stoichiometry [18]. For a sub-stoichiometric structure, the Ti atom prefers to occupy an interstitial site resulting in a face-sharing octahedral coordination. On the other hand, a fully stoichiometric defect essentially retains the bulk-like cationic positions even though the defect structure is significantly affected by molecular distortions. So, a similar concept can be extended onto the reconstruction on TiO_2(001) [75-77]. With a fully stoichiometric surface, bulk-extended positions are expected to be stable and preferable for Ti atoms. However, O atoms are allowed for distortions, so that minimizes the total number of unsaturated ligand coordination of Ti atoms.

(3) Exposed Ti sites should appear as bright spots in STM. Because the sample is positively biased, the electrons tunnel from the tip to the empty states of the surface, which are mostly Ti d orbitals. On the other hand, O atoms and Ti atoms underneath O atoms are expected to appear dark or unseen as in TiO_2(110). However, molecular distortions and the changes in electronic structure can influence local density of states substantially. So, one should keep in mind that this assumption may not be a good one.

(4) A hexamer of TiO_2 is the elementary structural building block. This idea was inspired by the stoichiometric cluster defect on TiO_2(110). They were observed to play an active role as a mobile species in the restoration of oxygen-deficient TiO_2 by growing into strands and terraces [53, 54]. A similar view has been adopted and used by Kubo *et al.* in their model of TiO_2(001) [76].

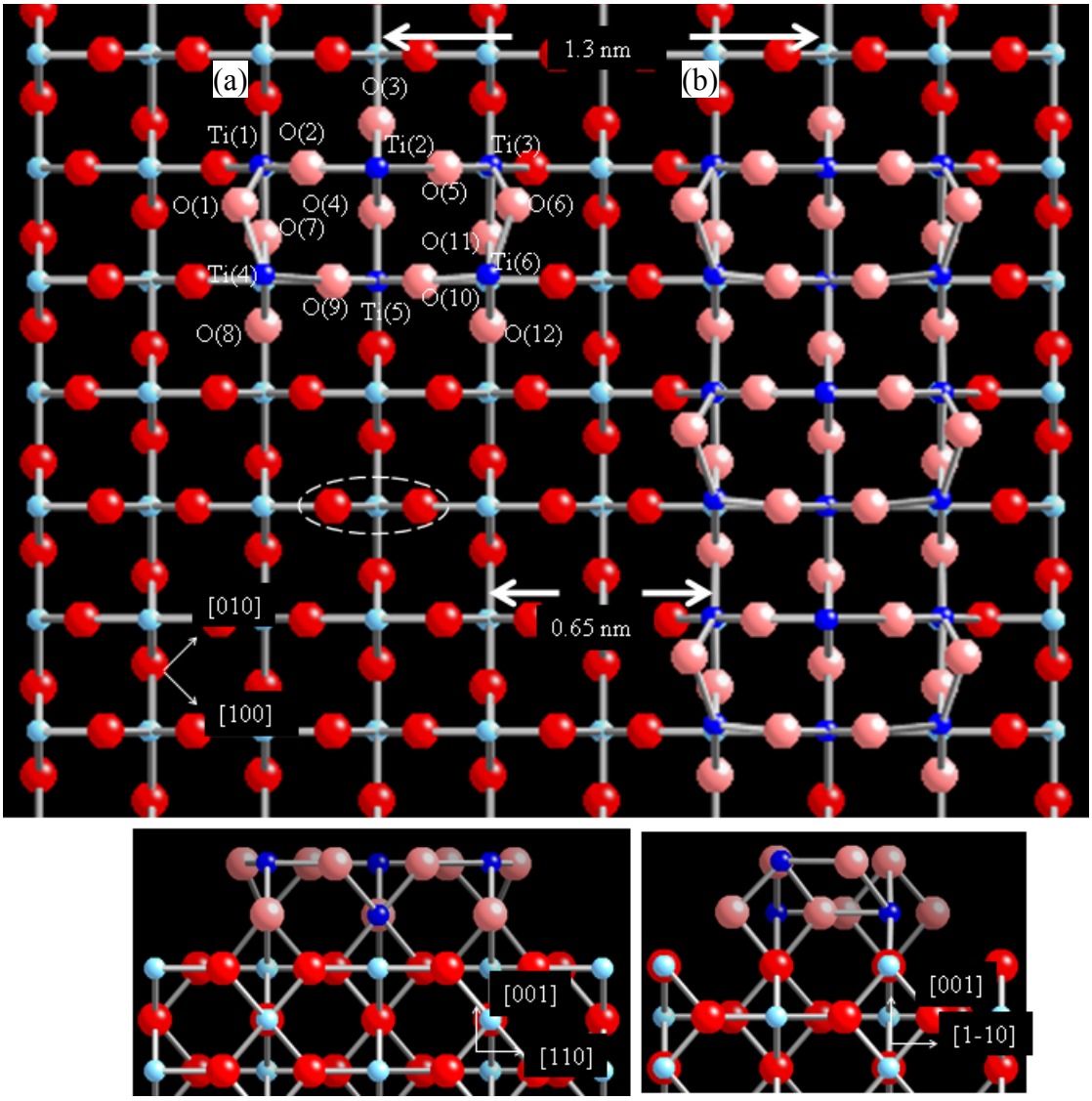

FIG. 5.18. Proposed model for TiO_2(001) reconstructed surface. (a) A cluster is formed of $(TiO_2)_6$ unit and (b) the formation of row-like linear structure with repeating units of $(TiO_2)_6$. Atoms colored in light pink and dark blue are the surface oxygen and titanium atoms, respectively, while red and light blue atoms are the bulk oxygen and titanium atoms, respectively. The chosen form of TiO_2 is highlighted in an ellipse (top).

Fig. 5.18 (a) shows the hexamer structure that accounts for a bright cluster within a linear structure on TiO_2(001). The cluster is constructed with six TiO_2 units. The chosen TiO_2 unit (highlighted in an ellipse in Fig. 5.18) consists of two coplanar oxygen atoms and a titanium atom of the bulk structure. The bond angle ($\angle$O –Ti –O) of

81.07° without relaxation is smaller than the chosen form whose angle is 180° in Fig. 5.2 [76]. As the dangling bond charge density is localized on the oxygen atoms, the cluster atoms are then expected to relax to saturate their local chemical valence [11, 18]. Hence the bond between O (1) and Ti (1) is distorted so that O (1) can approach Ti (4) to form a bond (similarly for Ti (6) and O (6)). The estimated bond length is slightly longer than 1.98 Å. In this way, the O atoms (1 and 6) and Ti atoms (4 and 6) are 2-fold and 4-fold coordinated, respectively. Also, as the added atoms are at the bulk-extended positions, they form bonds with the lower layer atoms in the same way as the bulk atoms. Overall, the cluster O atoms are 3- or 2-fold coordinated and Ti (1), Ti (3) and Ti (5) atoms are 5-fold coordinated and Ti (2), Ti (4) and Ti (6) are 4-fold coordinated. Alternatively this can be thought of in each isolated hexamer cluster, the numbers of unsaturated bond per O and per Ti atom are 0.75 and 1.5, respectively. These numbers are smaller than 0.8 and 1.6, respectively, for the pentamer structure shown in Fig. 5.2 [76].

The three 4-fold coordinated Ti atoms are expected to exhibit as bright spots in STM. They are separated by 3 Å, perpendicular to the row axis with one another. Their separation along the row axis is also 3 Å, although this value is inconsistent with the STM observation [74-77]. It is quite possible that even though the atoms are initially added at bulk-extended positions of the substrate, reasonable relaxation may shift the positions or reorient the TiO_2 units. Also, electronic charge can be redistributed to reduce the energy and create electronically more favorable local bonding environment. These changes might affect the relative positions and the relative apparent brightness of the Ti atoms imaged by STM.

The hexamer cluster is about 3 Å above the surface atom. It has the same geometry height compared to the pentamer structure in the {111}-microfacted model [76]. The shape of the pentamer is pyramid-like with the base area 4.6 × 4.6 $Å^2$, and the hexamer has a shape of rectangular block with the base area 6.6 × 3.2 $Å^2$. Within the same unit volume, the hexameric structure is more compact and amassed. It has been found both theoretically and experimentally that compact islands and chains are preferable on single element surfaces [97-99].

As the hexameric cluster grows into a nanometer-sized row, the number of unsaturated bonds for each hexamer further decreases, which reduces the energy cost [100]. Fig. 5.18(b) shows a row structure of about 2 nm long with 3 repeating units of $(TiO_2)_6$. The interval of 6.5 Å along the row is reproduced. Two such parallel rows can be generated by adding (removing) strands to (from) the (001) bulk-terminated surface with a 13 Å separation along the [110] direction and the gap distance 6.5 Å between the strands (Fig. 5.19(a)). The {114} microfacet structure observed by STM is hence formed. If the strand width is twice as large, the {116} microfacet structure obtained from the LEED kinematic analysis can be reproduced (Fig. 5.19(b)). It is note-worthy that the linear structure on TiO_2(001) is in sharp contrast to the substoichiometric strands in TiO_2(110) [50] discussed in Chap. 4.

Unlike the terrace, which can be imaged directly, the structural detail of the gap between the rows is still unknown. For example, it is recognized that atoms at a step are under stress to maintain their bulk positions despite the lower coordination number. Locally they can relax outwardly to minimize the stress present. The relaxation of atoms at one step can oppose the relaxation of atoms at a neighboring step which

effectively produces impulsive step-step interactions [100]. Future study to obtain more detailed information about the gap will be very useful in understanding reconstructed TiO_2(001) (see Sec. 6.2).

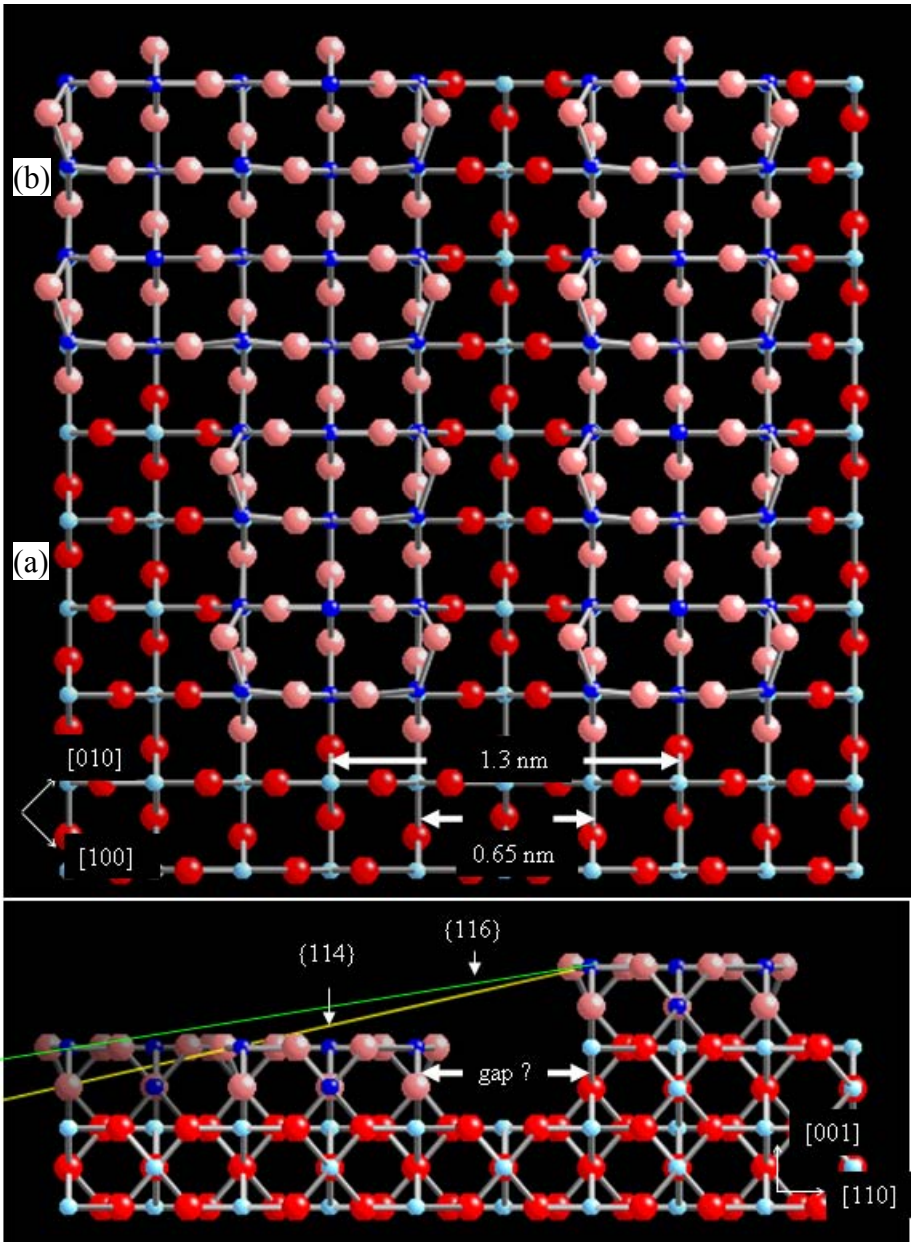

FIG. 5.19. Proposed model for TiO_2(001) reconstructed surface of (a) {114} microfacet structure and (b) {116} microfacet structure.

CHAPTER SIX

Conclusion

6.1 General Conclusions

This work reported our recent investigation into the surface structures of the pristine and partially reduced (1 × 1) TiO_2(110) and the reconstructed TiO_2(001) studied by LEED and STM. The structural-functionality relationship for nanometer-sized defects on TiO_2(110) and TiO_2(001) was reported to further understanding of the surface structures behind the photochemistry and surface catalysis related with TiO_2. Chap. 1 gave an introduction to the crystal and electronic structures of TiO_2 along with its current applications. The relevant experimental techniques, equipment, and sample preparation conditions used to study TiO_2(110) and (001) surfaces were described in Chap. 2. The kinematic approach for LEED analysis was outlined in Chap. 3. The results and the corresponding discussion of TiO_2(110) and (001) surfaces were presented in Chaps. 4 and 5, respectively.

A clean but partially reduced TiO_2(110) surface exhibited a structure and stoichiometry being far from homogeneous at the nanometer scale. Among various surface defects, the nanometer-sized clusters or dot defects were investigated by STM.

Using the DFT calculations, it was proposed that the dot defects were nanometer-sized, stoichiometric clusters. They were further modeled as $(TiO_2)_6$, which was located above the surface bridging O row and the 5-fold Ti row. Because of cluster's small size and lack of neighboring atoms, it suffered from severe under-coordination and consequently adopted a unique molecular geometry and orientation.

It was also reported that the dot defects were the preferential adsorption sites for Au deposition and the formation of nanoparticles over the substoichiometric strands and oxygen vacancies on the surface. The energy gain upon Au adsorption on the dot defects was 2.74 eV, among the largest values reported in the literature. This exceptionally strong bonding was the direct consequence of the unique geometry of the dot defect and the resulting density of states accessible for bonding. The under-coordinated O atoms both at the defect and the surface had a limited number of states near and above the Fermi level for adsorbing Au to saturate their dangling bonds via hybridization. In addition, the geometry was such that the Coulomb repulsion between the O atoms could be lowered with Au adsorbed between them. The adsorbed Au at the cluster thus became cationic, which was electron deficient. Such cationic Au has been well known in chemistry and suggested as a possible candidate for the catalytically active Au nanoparticles for the oxidation of CO.

TiO_2(001) on the other hand, has been one of the least studied surfaces of TiO_2. Both LEED and STM indicated that the surface underwent extensive reconstruction upon sputtering and annealing and exhibited a $(2\sqrt{2} \times \sqrt{2})R45^\circ$ overlayer with the formation of the row-like linear structures running along the [110] and the $[1\bar{1}0]$ directions. The row-like linear structure consisted of nanostepped rows. Each row was further made of bright dots separated by 6.5 Å along the row axis. Depending on the separation between the nearest nanostepped rows, the row-like linear structures formed microfacets that could be interpreted as various stepped surfaces on a microscopic scale. To model the bright dot within a row-like structure, a stoichiometric cluster of a $(TiO_2)_6$ at the bulk-extended position was proposed. It was further suggested that the hexamer structure could be stabilized via rehybridization of the dangling bonds between Ti and O atoms upon allowed re-orientation and relaxation of molecular geometry. As the basic building block for the row-like structure, the cluster could further grow into the observed, nanometer-sized row.

6.2 Future Considerations

We have characterized the nanometer-sized row defects on the TiO_2(001) surface quantitatively and proposed the surface reconstruction model. So, the first immediate follow-up study can be a test of the proposed model using DFT calculations. The total

energy calculation after full geometric relaxation would tell right away about the stability of the proposed row defect structure. In addition, by carefully choosing and examining the same TiO_2 cluster units within the row structure, one can even compare the energetics between the model proposed in this study and that by Kubo *et al*. [76].

Experimentally, one should collect more LEED data, especially at low temperature, and extend the energy range of I-V curves of TiO_2(001) surface. Although it is not clear if the advancement of the dynamical theory would allow the accurate calculations of the I-V peaks from such a stepped and domained surface, it would be a worthy attempt to determine crystallographic information. Since low-energy electrons probe several angstroms beneath the surface, LEED has an advantage over STM, as it provids quantitative information on atomic coordinates, bond length, and bond angles in a few top layers [27].

Another experimental characterization of the row defects can be performed using the adsorption of probe molecules. Certain structural information can be revealed from the results of inorganic and organic molecular adsorption since the surface chemistry is influenced by the surface structure [1]. For example, carboxylic acids adsorb dissociatively on the exposed cations and anions on oxide surfaces with the coordination

requirement. Therefore, their reactions bring out the surface coordinative unsaturation and oxidation state properties [101, 102].

Our results and model could then be applied to the study of interfacial thin film formation of vanadium oxide. The system of VO_2 grown on TiO_2(001) has shown the metal-insulator transition character [103-105], the behavior and the transition temperature of which are highly affected by the surface reconstruction of TiO_2(001) [104]. The vanadium oxide particles supported on TiO_2 is also a well known catalytic system. Known as a mixed-metal oxide, it performs many important selective oxidation and ammoxidation processes, which are of major commercial importance [106]. By studying VO_2 nanoparticles on TiO_2 single crystal surfaces using STM and LEED, one can address many fundamental aspects of the surface physics and chemistry on mixed-metal oxide systems such as the location and the nature of the active sites as well as the origin of the chemical activity and the mechanisms.

Lastly but not least, a low-temperature experiment on Au deposited on TiO_2 could be a valuable future study. With the surface temperature lowered with liquid nitrogen or even helium, the deposited Au atoms should slow down considerably so that one could expect different initial adsorption sites and morphology for Au nanoclusters on TiO_2(110) and TiO_2(001) [107]. Such a study could provide insight into surface diffusion barriers

and the initial formation of Au nanoclusters. Using scanning tunneling spectroscopy (STS), the study could further experimentally map the local electronic structures around Au nanoclusters to corroborate the proposed active site for low-temperature CO oxidation.

APPENDIX

APPENDIX A

Calibration for LEED Measurements and Determination of the Surface Lattice Constants

The kinematic scattering condition shown in Eq. 3.8 indicates that the parallel component of the scattered vector from a normal incidence equals the two-dimensional reciprocal lattice vector. This relationship is shown in Fig. A1. From Fig. A1 one can obtain

$$\sin\theta=\frac{2\pi}{ak}, \tag{A.1}$$

where is θ the scattering angle, a is the one dimensional lattice constant and k is the magnitude of the electron wave vector. k can be written as a function of energy

$$E=\frac{p^2}{2m_e}=\frac{(\hbar k)^2}{2m_e} \quad \text{or} \quad k=\frac{\sqrt{2m_eE}}{\hbar}$$

Hence, Eq. A.1 becomes

$$\sin\theta=\frac{h}{a\sqrt{2m_eE}} \tag{A.2}$$

On the other hand, the experimental geometry in Fig. A1(b) shows that

$$\sin\theta=\frac{D}{R} \tag{A.3}$$

where D is the distance from the specular beam to the n^{th} order scattered beam shown on the screen, and R is the distance from the sample to the screen. Combining the Eqs.

(A.2) and (A.3), one obtains

$$\frac{D}{R}=\frac{h}{a\sqrt{2m_eE}} \tag{A.4}$$

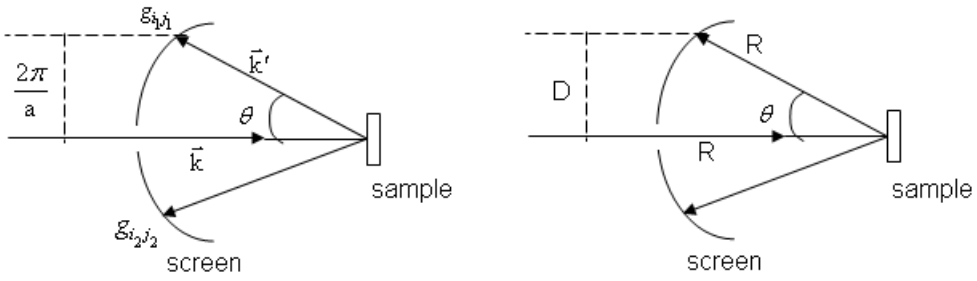

Fig. A.1 LEED geometry in the reciprocal space (a) and in the real space (b) for the lattice calibration. In the reciprocal space scheme $\vec{k}$, and $\vec{k}'$ are the wave vectors for the incident and scattered electron and a is the lattice constant. In the real space scheme, R is the sample to screen distance and D is the distance form the center of the screen to the spot.

A.1 Lattice calculation of TiO_2(110) using Ag(111) as the reference

The lattice constant of Ag(111) is 2.89 Å [105]. The (20) beams of Ag(111) appear at the edge of the screen at 180 eV. Given the diameter straight across from the 6" screen of 6.3 cm [24], the sample to screen distance R can be found from Eq. (A.4) to be 4.97 cm.

On the other hand, the (01) and (10) beams of TiO_2(110) appear at the edge of the screen at 35 and 40 eV, respectively. Using Eq. (A.4) together with the R obtained, the lattice constants of TiO_2(110) are found as 6.55 and 3.06 Å.

BIBLIOGRAPHY

[1] U. Diebold, "The Surface Science of Titanium Dioxide," Surf. Sci. Rep. 48, 53 (2003).

[2] V. E. Henrich and P. A. Cox, The Surface Science of Metal Oxides, (Cambridge, New York, 1994), pp. 2, 421-422.

[3] H. Selhofer, "Titanium oxides for optical-interference coatings," Vac. Thin Films 2, 15–19 (1999).

[4] A. Fujishima and K. Hinda, "Electrochemical Photolysis of Water at A Semiconductor Electrode," Nature 238, 37 (1972).

[5] H. Ariga, T. Taniike, H. Morikawa, M. Tada, B. K. Min, K. Watanabe, Y. Matsumoto, S. Ikeda, K. Saiki and Y. Iwasawa, "Surface-Mediated Visible-Light Photooxidation on Pure TiO_2(001)," J. Am. Chem. Soc. 131, 14670 (2009).

[6] L. Gao, S. Zheng and Q. Zhang, Materials and Application of Nano-TiO_2 for Photocatalysis, (Chemical Industry Publication, Beijing, 2002), pp. 26-27.

[7] W. H. Baur, "The Refinement of the Crystal-Structure Determination of Some Representatives of the Rutile Type: TiO_2, SnO_2, GeO_2, and MgF_2," Acta. Cryst. 9, 515 (1956).

[8] F. A. Grant, "Properties of Rutile (Titanium Dioxide)," Rev. Mod. Phys. 31, 646 (1959).

[9] J. P. LaFemina, "Total Energy Computations of Oxide Surface Reconstructions" Crit. Rev. Surf. Chem. 3, 297 (1994).

[10] P. W. Tasker, "The Stability of Ionic Crystal Surfaces," J. Phys. C 12, 4977 (1979).

[11] J. P. LaFemina, “Theory of Insulator Surface Structures,” in Handbook of Surface Science, Vol. 1 Physical Structure (edited by W. N. Unertl, Elsevier, Amsterdam, The Netherlands, 1996), pp. 142, 178.

[12] G. A. Somorjai, “Active Sites in Heterogeneous Catalysis,” Adv. Catal. 26, 1 (1977).

[13] P. J. D. Lindan, N. M. Harrison, M. J. Gillan and J. A. White, “First-principles Spin-polarized Calculations on The Reduced and Reconstructed TiO_2(110) Surface,” Phys. Rev. B 55, 15919 (1997).

[14] A. T. Paxton and L. Thiên-Nga, “Electronic Structure of Reduced Titanium Dioxide,” Phys. Rev. B 57, 1579 (1998).

[15] P. J. Hardman, G. N. Raikar, C. A. Muryn, G. van der Laan, P. L. Wincott, G. Thornton, D. W. Bullett and P. A. D. M. A. Dale, “Valence-Band Structure of TiO_2 along the Γ-Δ-X and Γ-Σ-M Directions,” Phys. Rev. B 49, 7170 (1994).

[16] H. Onishi and Y. Iwasawa, “Reconstruction of TiO_2(110) Surface: STM Study with Atomic-Scale Resolution,” Surf. Sci. 313, L783 (1994).

[17] K. F. McCarty and N. C. Bartelt, “Role of Bulk Thermal Defects in the Reconstruction Dynamics of the TiO_2(110) Surface,” Phys. Rev. Lett. 90, 046014 (2003).

[18] K. T. Park, V. Meunier, M. H. Pan, W. A. Shelton, N.-H. Yu and E. W. Plummer, “Nanoclusters of TiO_2 Wetted with Gold,” Surf. Sci. 603, 3131 (2009).

[19] G. A. Somorjai, Chemistry in Two Dimensions: Surfaces (Cornell Univ. Press, 1981), pp. 26, 39, 45.

[20] F. -C. Chen and C. -S. Chang, Vacuum Technology & Application, (National Science Council Precision Instrument Development Center, Taiwan, 2001), p.102.

[21] P. J. Biltoft and M. A. Benapfl, Vacuum Technology, Theory and Laboratory Exercises, Las Positas College, 2002, p. 126.

[22] J. T. Yates, Jr., Experimental Innovations in Surface Science, (Springer, Berlin, Germany, 1998), pp. 132, 517, 520, 566.

[23] M. Haruta, "Size- and Support-Dependency in the Catalysis of Gold," Catal. Today 36, 153 (1997).

[24] Manual ErLEED, VSI Vacuum Science Instruments GmbH, 1997, p. 11 and the technical data.

[25] Ellis, T. S. (2005) Heteroepitaxial Metallo-Phthalocyanine (MPc, M = Co, Ni, Cu) Thin Films on Gold: Atomic and Interfacial Electronic Structures. (Doctoral dissertation,) pp. 44-55.

[26] K. Heinz and K. Muller, Structural Studies of Surfaces, (Springer-Verlag, Fed. Rep. Ger., 1982), p. 22.

[27] M. A. Van Hove, W. H. Weinberg and C. –M. Chan, Low-Energy Electron Diffraction, (Springer-Verlag, Heidelberg, 1986), pp. 26, 92-93, 113-114.

[28] J. P. Ibe, P. P. Bey, S. L. Brandow, R. A. Brizzolara, N. A. Burnham, D. P. DiLella, K. P. Lee, C. R. K. Marrian, and R. J. Colton, "On the Electrochemical Etching of Tips for Scanning Tunneling Microscopy," J. Vac. Sci. Technol. A 8, 3570 (1990).

[29] J. Méndez, M. Luna, A.M. Baró, "Preparation of STM W Tips and Characterization by FEM, TEM and SEM," Surf. Sci. 266, 294 (1992).

[30] C. J. Chen, Introduction to Scanning Tunneling Microscopy 2nd edition, (Oxford, New York, 2008), pp 1-5, 220, 289-290, 313-316, 324-325.

[31] H. Lüth, Solid Surfaces, Interfaces and Thin Films 4th edition, (Springer-Verlag, Berlin Heidelberg, 2001), pp. 154-155, 158-160.

[32] M. Henzler, "Atomic Steps on Single Crystals: Experimental Methods and Properties," Appl. Phys. 9, 11 (1976).

[33] G. Binnig, H. Rohrer, Ch. Gerber and E. Weibel, "Tunneling through a Controllable Vacuum Gap," Appl. Phys. Lett. 40, 178 (1982).

[34] G. Binnig, H. Rohrer, Ch. Gerber and E. Weibel, "Surface Studies by Scanning Tunneling Microscopy," Phys. Rev. Lett. 49, 57 (1982).

[35] R. P. Feynman. There's Plenty of Room at the Bottom: An Invitation to Enter a New Field of Physics. Lecture at an 1959 APS meeting. The Archives, California Institute of Technology, see www.its.caltech.edu/~feynman/plenty.html (1959).

[36] A. Szabo and T. Engel, "Structural Studies of TiO_2(110) Using Scanning Tunneling Microscopy," Surf. Sci. 329, 241 (1995).

[37] S. Mannix and S. Schmeitz, "Electronic Structure of Ideal TiO_2(110), TiO_2(001), and TiO_2(100) Surfaces," Phys. Rev. B 30, 2202 (1984).

[38] C. G. Mason, S. P. Tear, T. N. Doust and G. Thornton, "A Low-energy Electron Diffraction Analysis of The Structure of The Titanium Dioxide (001) Surface," J. Phys.: Condens. Matter 3, S97 (1991).

[39] R. P. Gupta, "Lattice Relaxation at a Metal Surface," Phys. Rev. B 23, 6265 (1981).

[40] J. M. Pan, B. L. Maschhoff, U. Diebold and T. E. Madoy, "Interaction of Water, Oxygen, and Hydrogen with TiO_2(110) Surfaces Having Different Defect Densities" J. Vac. Sci, Technol. A. 10, 2470 (1992).

[41] U. Diebold, J. Lehman, T. Mahmoud, M. Kuhn, G. Leonardelli, W. Hebenstreit, M. Schmid and P. Varga, "Intrinsic Defects on a TiO_2(110)(1×1) Surface and Their Reaction with Oxygen: a Scanning Tunneling Microscopy Study," Surf. Sci. 411,137 (1998).

[42] J. B. Pendry, Low Energy Electron Diffraction: The Theory and Its Application to Determination of Surface Structure, (Academic Press Inc., London, 1974).

[43] R. Lindsay, A. Wander, A. Ernst, B. Montanari, G. Thornton and N. M. Harrison, "Revisiting the Surface Structure of TiO_2(110): A Quantitative Low-Energy Electron Diffraction Study," Phys. Rev. Lett. 94, 246102 (2005).

[44] G. Charlton, P. B. Howes, C. L. Nicklin, P. Steadman, J. S. G. Taylor, C. A. Muryn, S. P. Harte, J. Mercer, R. McGrath, D. Norman, T. S. Turner and G. Thornton, "Relaxation of TiO_2(110)-(1 × 1) Using Surface X-Ray Diffraction," Phys. Rev. Lett. 78, 495 (1997).

[45] J. Rundgren, "Optimized Surface-Slab Excited-State Muffin-Tin Potential and Surface Core Level Shifts," Phys. Rev. B 68, 125405 (2003).

[46] V. B. Nascimento, R. G. Moore, J. Rundgren, Jiandi Zhang, Lei Cai, R. Jin, D. G. Mandrus and E. W. Plummer, "Procedure for LEED I-V Structural Analysis of Metal Oxide Surfaces: $Ca_{1.5}Sr_{0.5}RuO_4$(001)," Phys. Rev. B 75, 035408 (2007).

[47] I. Horcas, R. Fernandez, J.M. Gomez-Rodriguez, J. Colchero, J. Gomez-Herrero and A. M. Baro, "WSXM: A Software for Scanning Probe Microscopy and a Tool for Nanotechnology," Rev. Sci. Instrum. 78, 013705 (2007).

[48] U. Diebold, J. F. Anderson, K.-O. Ng and D. Vanderbilt, "Evidence for the Tunneling Site on Transition-Metal Oxides: TiO2(110)," Phys. Rev. Lett. 77, 1322 (1996).

[49] M. Li, W. Hebenstreit and U. Diebold, "Morphology Change of Oxygen-Restructured TiO_2(110) Surfaces by UHV Annealing: Formation of a Low-temperature (1 × 2) structure," Phys. Rev. B 61, 4926 (2000).

[50] U. Diebold, M. Li, O. Dulub, E. L. D. Hebenstreit and W. Henenstreit, "The Relationship Between Bulk and Surface Properties of Rutile TiO_2(110)," Surf. Rev. Lett. 5-6, 613 (2000).

[51] M. Li, W. Hebenstreit, U. Diebold, A. M. Tyryshkin, M. K. Bowman, G. G. Dunham and M. A. Henderson, "The Influence of the Bulk Reduction State on the Surface Structure and Morphology of Rutile TiO_2(110) Single Crystals," J. Chem. Phys. B, 104, 4944 (2000).

[52] K. T. Park, M. H. Pan, V. Meunier and E. W. Plummer, "Surface Reconstructions of TiO_2(110) Driven by Suboxides," Phys. Rev. Lett. 96, 226105 (2006).

[53] R. A. Bennett, P. Stone, N. J. Price and M. Bowker, "Two (1×2) Reconstructions of TiO_2(110): Surface Rearrangement and Reactivity Studied Using Elevated Temperature Scanning Tunneling Microscopy," Phys. Rev. Lett. 82, 3831 (1999).

[54] K. F. McCarty, "Growth Regimes of the Oxygen-Deficient TiO_2(110) Surface Exposed to Oxygen," Surf. Sci. 543, 185 (2003).

[55] J. Tersoff and D.R. Hamann, Phys. Rev. B 31 (1985) 805, as implemented in the BSKAN package (W.A. Hofer, J. Redinger, Surf. Sci. 447 (2000) 51.).

[56] D. Matthey, J. G. Wang, S. Wendt, J. Matthiesen, R. Schaub, E. Lægsgaard, B. Hammer and F. Besenbacher, "Enhanced Bonding of Gold Nanoparticles on Oxidized TiO_2(110)," Science 23, 1692 (2007).

[57] G. K. H. Madsen and B. Hammer, "Effect of Subsurface Ti-Interstitials on the Bonding of Small Gold Clusters on Rutile TiO_2(110)," J. Chem. Phys. 130, 044704 (2009).

[58] M. Valden, X. Lai and D. W. Goodman, "Onset of Catalytic Activity of Gold Clusters on Titania with the Appearance of Nonmetallic Properties," Science 281, 1647 (1998).

[59] S. A. Varganov, R. M. Olson, M. S. Gordon, G. Mills and H. Metiu, "A Study of the Reactions of Molecular Hydrogen with Small Gold Clusters," J. Chem. Phys. 120, 5169 (2004).

[60] U. Diebold, "Dispersed Au Atoms, Supported on TiO_2(110)," Surf. Sci. 578, 1 (2005).

[61] E. Wahlström, N. Lopez, R. Schaub, P. Thostrup, A. Rønnau, C. Africh, E. Lægsgaard, J. K. Nørskov and F. Besenbacher, "Bonding of Gold Nanoclusters to Oxygen Vacancies on Rutile TiO_2(110)," Phys. Rev. Lett. 90, 026101 (2003).

[62] Q. Fu, H. Saltsburg and M. Flytzani-Stephanopoulos, “Active Nonmetallic Au and Pt Species on Ceria-Based Water-Gas Shift Catalysts,” Science 301 (2003) 935.

[63] J. Guzman and B.C. Gates, “Catalysis by Supported Gold: Correlation between Catalytic Activity for CO Oxidation and Oxidation States of Gold,” J. Am. Chem. Soc. 126, 2672 (2004).

[64] G.. J. Hutchings, M. S. Hall, A. F. Carley, P. Landon, B. E. Solsona, C. J. Kiely, A. Herzing, M. Makkee, J. A. Moulijn, A. Overweg, J. C. Fierro-Gonzalez, J. Guzman and B. C. Gates, “Role of Gold Cations in the Oxidation of Carbon Monoxide Catalyzed by Iron Oxide-Supported Gold,” J. Catal. 242, 71 (2006).

[65] R. Meyer, C. Lemire, Sh.K. Shaikhutdinov and H.-J. Freund, Gold Bull. 37, 72 (2004) and references therein.

[66] M. Haruta and M. Daté, “Advances in the Catalysis of Au Nanoparticles,” Appl. Catal. A 222, 427 (2001).

[67] L. M. Molina and B. Hammer, “Active Role of Oxide Support during CO Oxidation at Au/MgO,” Phys. Rev. Lett. 90, 206102 (2003).

[68] X. Wu, L. Senapati, S.K. Nayak, A. Selloni, M. Hajaligol, “A Density Functional Study of Carbon Monoxide Adsorption on Small Cationic, Neutral, and Anionic Gold Clusters,” J. Chem. Phys. 117, 4010 (2002).

[69] Y.W. Chung, W.J. Lo and G.A. Somorjai, “LEED and Electron Spectroscopy Studies of the Clean (110) and (100) Titanium Dioxide (Rutile) Crystal Surfaces,” Surf. Sci. 64, 588 (1977).

[70] R. H. Tait and R. V. Kasowski, “Ultraviolet Photoemission and Low-energy-electron Diffraction Studies of TiO_2 (rutile) (001) and (110) surfaces,” Phys. Rev. B 20, 5178 (1979).

[71] L. E. Firment, “Thermal Faceting of The Rutile TiO_2(001) Surface,” Surf. Sci. 116, 205 (1982).

[72] C. W. Tucker, “Low-Energy Electron Diffraction from Faceted Surfaces,” J. Appl. Phys. 38, 5570 (1968).

[73] H. Nörenberg, F. Dinelli and G.A.D. Briggs, “The Surface Structure of TiO_2(001) after High Temperature Annealing Studied by AFM, STM, and Optical Microscopy,” Surf. Sci. 446, L83 (2000).

[74] K. Fukui, R. Tero and Y. Iwasawa, “Atom-Resolved Structure of TiO2(001) Surface by Scanning Tunneling Microscopy,” Jpn. J. Appl. Phys. 40, 4331 (2001).

[75] R. Tero, K. Fukui and Y. Iwasawa, “Atom-Resolved Surface Structures and Molecular Adsorption on TiO2(001) Investigated by Scanning Tunneling Microscopy,” J. Phys. Chem. B 107, 3207 (2003).

[76] T. Kubo, K. Sayama, and H. Nozoye, “Microfaceting Explains Complicated Structures on Rutile TiO2 Surfaces ,” J. Am. Chem. Soc. 128, 4074 (2006).

[77] H. Ariga, T. Taniike, H. Morikawa, R. Tero, H. Kondoh and Y. Iwasawa, “Lattice-Work Structure of a TiO_2(001) Surface Studied by STM, Core-Level Spectroscopies and DFT Calculations,” Chem. Phys. Lett. 454, 350 (2008).

[78] A. Busiakiewicz, Z. Klusek, M. Rogala, P. Dabrowski, P. J. Kowalczyk and P. K. Datta, “The New High-temperature Surface Structure on Reduced TiO2(001),” J. Phys.: Condens. Matter 22, 395501 (2010).

[79] M. Henzler, “LEED Studies of Surface Imperfection,” Appl. Surf. Sci 11/12, 450 (1982).

[80] K. Heinz , “LEED and DLEED as Modern Tools for Quantitative Surface Structure Determination,” Rep. Prog. Phys. 58, 637 (1995).

[81] O. Janzen, Ch. Hahn, T. U. Kampen and W. Mönch, “Explanation of Multiplet Spots in Low-Energy Electron Diraction Patterns of Clean GaN{0001}−1 × 1 Surfaces,” Eur. Phys. J. B 7, 1 (1999).

[82] H. Minoda and K. Yagi, “Gold-induced Faceting on A Si(001) Vicinal Surface: Spot-Profile-Analyzing LEED and Reflection-Electron-Microscopy Study,” Phys. Rev. B 59, 2363 (1999).

[83] W. Weigand, F. Reuss, L. Hansen, A. Waag, L. W. Molenkamp, C. Kumpf, M. Sokolowski and E. Umbach, “Structure of the Te/Ge(001) Surface Studied by SPA-LEED,” Surf. Sci. 562, 33 (2004).

[84] V. G. Kul’kov, “Faceting Kinetics of Incommensurate Tilt Boundaries,” Inorganic Materials, 41, 784 (2005). Translated from Neorganicheskie Materialy, Vol. 41, No. 7, 2005, pp. 892–896.

[85] S. Horng, K. Young and A. Kahn, “Structural Studies of (331) GaAs Surface,” J. Vac. Sci. Technol. A 7, 2039 (1989).

[86] R. L. Kurtz, “Stimulated Desorption Dtudies of Defect Structures on TiO_2,” Surf. Sci. 177, 526 (1986).

[87] The diameters straight across the 6” and 8” screens are 6.3 and 10.8 cm, respectively [24] and the corresponding sample to screen distances are 5 and 8 cm, respectively.

[88] W.P. Ellis and R.L. Schwoebel, “LEED from Surface Steps on UO_2 Single Crystals,” Surf. Sci. 11, 82 (1968).

[89] M. Henzler, “LEED-Investigation on Step Arrays on Cleaved Germanium (111) Surfaces,” Suf. Sci. 19, 159 (1970).

[90] M. A. Van Hove, “Surface Crystallography with Low-energy Electron Diffraction,” Proc. R. Soc. Lond. A 442, 61 (1993).

[91] P. Pinkava and S. Crampin, “On the Calculation of LEED Spectra from Stepped Surfaces,” Surf. Sci. 233, 27 (1990).

[92] X. -G. Zhang, P. J. Rous, J. M. MacLaren, A. Gonis, M. A. Van Hove and G. A. Somorjai, "A Real-Space Multiple Scattering Theory of Low Energy Electron Diffraction: a New Approach for the Structure Determination of Stepped Surfaces," Surf. Sci. 239, 103 (1990).

[93] Anupam Roy, K. Bhattacharjee, H.P. Lenka, D.P. Mahapatra and B.N. Dev, "Surface Roughness of Ion-bombarded Si(100) Surfaces: Roughening and Smoothing with the Same Roughness Exponent," Nuc. Inst. Meth. Phys. Res. B 266, 1276 (2008).

[94] M. D. Antonik, J. C. Edwards and R. J. Lad, "Facet Formation on Single Crystal TiO_2 Surfaces Studied by Atomic Force Microscopy," Mat. Res. Soc. Symp. Proc. 237, 459 (1992).

[95] C. T. Chan, K. M. Ho and K. P. Bohnen, " Surface Reconstruction: Metal Surfaces and Metal on Semiconductor Surfaces," in Handbook of Surface Science, Vol. 1 Physical Structure (edited by W. N. Unertl, Elsevier, Amsterdam, The Netherlands, 1996), pp. 131, 116-117.

[96] C. B. Duke, "Surface Structures of Elemental and Compound Semiconductors," in Handbook of Surface Science, Vol. 1 Physical Structure (edited by W. N. Unertl, Elsevier, Amsterdam, The Netherlands, 1996), pp. 246-247.

[97] A, F. Wright, M. S. Daw and C. Y. Fong, " Structures and Energetics of Pt, Pd, and Ni Adatom Clusters on the Pt(001) Surface: Embedded-atom-method Calculations," Phys. Rev. B 42, 9409 (1990).

[98] P. R. Schwoebel, S. M. Foiles, C. L. Bisson and G. L. Kellogg , "Structure of Platinum Adatom Clusters on Pt(100): Experimental Observations and Embedded-Atom-Method Calculations, "Phys. Rev. B 40, 10639 (1989).

[99] T. L. Einstein, "Interaction Between Adsorbate Particles " in Handbook of Surface Science, Vol. 1 Physical Structure (edited by W. N. Unertl, Elsevier, Amsterdam, The Netherlands, 1996), p. 627.

[100] M. C. Tringides, " Atomic Scale Defects on Surfaces," in Handbook of Surface Science, Vol. 1 Physical Structure (edited by W. N. Unertl, Elsevier, Amsterdam, The Netherlands, 1996), pp. 664, 671.

[101] M. A. Barteau, "Site Requirements of Reactions on Oxide Surfaces," J. Vac. Sci. Technol. A 11, 2162 (1993).

[102] M. A. Barteau, "Organic Reactions at Well-Defined Oxide Surfaces," Chem. Rev. 96, 1413 (1996).

[103] Y. Muraoka, Y. Ueda and Z. Hiroi, "Large Modification of the Metal–Insulator Transition Temperature in Strained VO_2 Films Grown on TiO_2 Substrates," J. Phys. Chem. Solids 63, 965 (2002).

[104] K. Nagashima, T. Yanagida, H. Tanaka and T. Kawai, "Interface Effect on Metal-insulator Transition of Strained Vanadium Dioxide Ultrathin Flms," J. Appl. Phys. 101, 026103 (2007).

[105] V. Pardo and W. E. Pickett, "Half-Metallic Semi-Dirac-Point Generated by Quantum Confinement in TiO_2 /VO_2 Nanostructures," Phys. Rev. Lett. 102, 166803 (2009).

[106] B. M. Weckhuysen and D. E. Keller, "Chemistry, Spectroscopy and the Role of Supported Vanadium Oxides in Heterogeneous Catalysis," Catal. Today 78, 25 (2003).

[107] G. Neuhold, L. Bartels, J.J. Paggel and K. Horn, "Thickness-Dependent Morphologies of Thin Ag Films on GaAs(110) as Revealed by LEED and STM," Surf. Sci. 376, 1 (1997).

[108] E. D. Palik, Handbook of Optical Constants of Solids, 3rd ed., edited by E. D. Palik (Academic Press, London, UK, 1998), p. 189.